UNIVERSITÀ DI TRENTO

Department of Industrial Engineering

XXXIII cycle

Doctoral School in Materials, Mechatronics
and System Engineering

Nanostructured flexible radiation sensors

Matteo Favaro

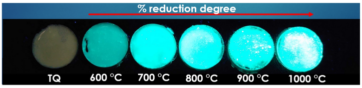

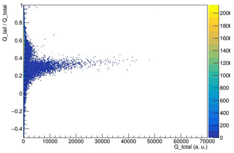

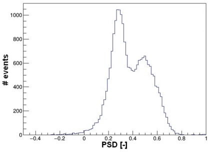

24 June 2021

Nanostructured flexible radiation sensors

Matteo Favaro

Email: matteo.favaro@unitn.it

Approved by:

Prof. Alberto Quaranta, Advisor
Dept. of Industrial Engineering
University of Trento, Italy

Ph.D. Commission:

Prof. Beatrice Fraboni
Dept. of Physics and Astronomy "Augusto Righi"
University of Bologna, Italy

Prof. Enrico Trave
Dept. of Molecular Sciences and Nanosystems
Ca' Foscari University of Venice, Italy

Prof. Devid Maniglio
Dept. of Industrial Engineering
University of Trento, Italy

University of Trento

Department of Industrial Engineering

24 June 2021

University of Trento - Department of Industrial Engineering

Doctoral Thesis

Matteo Favaro - 24 June 2021
Published in Trento (Italy) - by University of Trento

ISBN: - - - - - - - - -

Abstract

Flexible scintillating radiation detectors have gained increasing attention in the scientific community in the last decade. They represent a fast and easy way for monitoring the impinging radiation in real time and acquire the dose released in medical treatments, like cancer radio- or proton-therapy sessions. Flexible linear-chain polysiloxane detectors offer the possibility to overcome geometrical limitations, they possess superior optical transparency and flexibility, and can be obtained with contained production costs and times, making them highly competitive with respect to traditional single-crystals and plastics. Unlike phenyl-containing siloxanes, linear polysiloxanes does not show direct interaction with the impinging radiation, therefore they can be used just as matrices for hosting luminescent materials, such as nanocrystals or nanopowders.

Quantum dots (QDs) are nanocrystals showing quantum confinement effects, with an incredible light yield, a tunable emission wavelength and a fast decay lifetime. For these reasons, they are worth being incorporated in siloxane-based scintillators as primary dyes, without the need of complex ternary systems. Part of this thesis analyzes the effects of ionizing radiation on the luminescence and temporal response of QD-loaded polysiloxanes for radiation detection and monitoring, with special focus on real-time measurements under proton beam.

Another possibility is to embed luminescent nanopowders, such as zinc oxide (ZnO) and reduced zinc oxide (ZnO:Zn). The Zn-rich form shows a remarked green luminescence, with increasing light yield as a function of the reduction degree, i.e. zinc content. In view of the above, this thesis reports the advances on polysiloxanes loaded with ZnO and ZnO:Zn phosphors. The core of the thesis is devoted to the progresses in ZnO production and treatment for the realization of multi-layered flexible scintillators. A special focus is putted on a novel production route based on atmospheric pressure plasma (APPJ), that allows for the co-deposition of ZnO-loaded plasma polymers and for the doping via liquid precursor solution.

Contents

List of Figures

List of Tables

List of Abbreviations

APD	Avalanche photodiode
AZO	Aluminum-doped zinc oxide
DBD	Dielectric barrier discharge
DBE	Defective band emission
DDBD	Double-dielectric barrier discharge
DSC	Differential scanning calorimetry
EDS	Energy dispersive spectroscopy
ESR	Electron spin resonance
FEG	Field emission gun
FT-IR	Fourier-transformed infrared spectroscopy
FRET	Förster Resonance Energy Transfer
NBE	Near band-edge emission
NMR	Nuclear magnetic resonance
PD	Plasma deposition
PMT	Photomultiplier tube
PPH	plasma-polymerized hexane
PVOH	Poly-vinyl alcohol
QD	Quantum dots
RET	Radiative Energy Transfer
SEM	Scanning electron microscope
SP	Spray pyrolysis
TGA	Thermogravimetric analysis
XRD	X-ray diffraction
XRL	X-ray radioluminescence

Introduction

A growing interest toward the realization of flexible polysiloxanes scintillating radiation detectors have attracted researchers in the last years [1–6]. The possibility to overcome geometrical limitations and to realize conformal detectors is squeezing material scientists minds in order to study, produce and improve advanced materials with radiation detection capabilities. These material are fundamental in the medical field, especially for radio-therapy and proton-therapy, where they can give a real time indication of the absorbed dose. Moreover, the wide possibilities offered by flexible detectors over traditional ones are driving a continuously increasing interest in the research field [7, 8].
Traditional inorganic crystal detectors, in fact, are limited mainly by geometrical and mechanical constraints, but also by production techniques and times, with associated high costs. One of the main advantages of inorganic crystals resides in their superior radiation hardness, being able to withstand massive doses without damaging or decreasing their performance. On average, the light output per unit energy is much higher compared to plastic scintillator, therefore they are still used as reference materials.
For many years plastics have been the only feasible alternative to inorganic crystals [9], being easy to scale up and to be produced in different shapes, with contained costs, from liquid precursors. However, when compared to inorganic crystals, their radiation hardness is poorer and they suffer the exposure to oxygen and moisture. To obtain a sufficiently high stability, additives to prevent radical formation and yellowing may be added to the precursor mixture, affecting the overall conversion performance.
In this framework, the rise of a new family of radiation hard and cost effective siloxane-based scintillators matches scientists and industrial interests [5, 6]. High chemical stability and reduced production costs and times meets the requirements of flexibility and scalability. Linear-chain

polysiloxane flexible scintillators, in fact, can overcome geometrical limitations thanks to their elastomeric behavior that allows high elongation, reduced bending radii and good mechanical stability. However, they are still at an early research stage, being not able to compete with traditional inorganic crystals in terms of light output per energy unit and transparency, but in some cases they perform close to plastics.

Two classes of siloxane-based scintillators can be pointed out: linear chain and phenyl-containing chain. While the former cannot produce intrinsic scintillation light, the latter behaves similarly to plastics, converting the impinging radiation at the phenyl rings. For these reasons, linear chain siloxanes needs to be loaded with an active component that can convert the radiation through scintillation. Inorganic nanopowders or organic molecules are usually added to the hosting matrix [3, 9–13] giving rise to a composite material.

However, the introduction of a second component increases the complexity of the system in terms of both production route and detection principles, with the rise of energy transfer mechanisms between the components. First of all, the second component needs to be either well dispersed in the hosting matrix or to be confined in a specific layer. In both cases, the addition of a second component with different refractive index introduces a series of problem correlated with transparency and transmittance. In fact, in the case of a well dispersed detection material, transparency is fundamental for an effective photon collection.

Another important aspect is the chemical nature of the active material, that changes the excitation and emission timing characteristics of the system, making it suitable for certain applications. Organic and inorganic loaders, in fact, behaves in a very different manner, with fast lifetimes for organic and slow one for inorganic.

In this thesis we focused on the production of nanostructured and composite materials for the realization of scintillators. At first, inorganic quantum dots (QD) embedded in a siloxane matrix were tested as potential novel scintillators under mixed radiation. The energy transfer between matrix and QDs resulted to be generally poor or negligible, except in the cases of radiation-induced matrix damaging.

To continue pursuing the nanoscale advantages, a preliminary study on the deposition of nanostructured oxides was carried out through an atmospheric pressure plasma jet (APPJ). Aluminum doped zinc oxide (ZnO:Al) and polymer encapsulated zinc oxide (ZnO/PPH) nano films deposited on silicon showed promising results. Unfortunately to date the thickness of such samples is too limited for making scintillators with adequate radiation detection capabilities.

Satisfactory scintillation performance were obtained with ZnO:Zn nanopowders and hybrid ZnO:Zn/PDMS composites. A systematic study of the effects of thermal reduction at high temperature in Ar/H_2 on ZnO powders was carried out. Upon complete characterization of the powders, multilayer flexible siloxane scintillators were casted and analyzed under mixed radiation sources.

In this framework, Chapter 1 introduces to the basic detection principles for mixed radiation, pointing out the main differences between organic and inorganic scintillators. Moreover, it focuses on a very important feature for proper mixed radiation detection: the pulse-shape discrimination (PSD) capability. This unique feature of the material allows to discriminate the interacting radiation based on the scintillation decay times.

Chapter 1 also introduces to the basis of zinc oxide, with an overview on the main properties focused on radiation detection. As it will be clearer later, zinc oxide have been widely investigate and is still gaining attention in the academic field for some unique features in the radiation detection and optoelectronic fields. Although widely investigate, we present some new aspects that need further deepening. In particular, a freshly new production route through atmospheric pressure plasma torch (APPJ). For this purpose, Chapter 2 introduces to the field of atmospheric pressure plasmas, with a general overview of the geometries, configurations, limitations and benefits. The advantages offered by this technique over traditional plasma ones resides in the generation of a plasma in atmospheric conditions, so the presence of a vacuum chamber and pump is not necessary anymore. The geometric limitations given by a vacuum chamber are easily overcame and the integration in existing industrial production lines is considered feasible for extensive surface treatments. Nevertheless, the main drawback is represented by the great effort needed to specifically tune a production process, as some chemical and physical parameters can affect the plasma plume. The use of APPJ technology in the research field is submitted to a general interest for the production of specific experimental-state devices for radiation detection. In particular, we focused on the possibility to co-deposit zinc oxide nanoparticles with plasma polymerized n-hexane for the realization of thin film scintillators for mixed radiations.

In general, the most widely used production technique for the realization of flexible detectors is still based on wet chemistry. This method allows for an homogeneous dispersion of the filler in the matrix, with controlled loading and casting. The dispersion of organic and inorganic fillers in a polymeric matrix through mixing and casting leads to superior optical and mechanical properties.

For this purpose, Chapter 3 presents all the production and characterization techniques used within this thesis. The polymeric matrix used for the realization of most samples is a poly-siloxane based matrix, that was selected for its superior optical transparency, flexibility and easiness of production and handling. It can be casted in a multitude of shapes and thicknesses, with variable phenyl content and therefore with different optical contributions.

Flexible scintillators, made of a poly-siloxane matrix with inorganic loading (quantum dots, QD) were characterized with steady-state and time-resolved measurements under proton beam irradiation. The results are reported in Chapter 4, where a particular attention is devoted to the investigation of energy-transfer mechanisms between the matrix and the loading component. The results showed a poor or negligible energy transfer between the matrix and the QDs, except in the cases of damaging.

Based on these initial results, a deeper investigation of zinc oxide-based scintillators is presented in Chapter 5, where the attention is focused on the mixed radiation detection capability. Zinc oxide and Zn-rich zinc oxide (ZnO:Zn) phosphors allows for mixed radiation detection and can be easily handled and incorporated. The realization of multi-layered films based on poly-dimethyl-siloxane (PDMS) with ZnO:Zn loading lead to a good detectability of α-particles, X-rays and protons. The PDMS matrix

granted an optimal flexibility level while retaining a superior optical transparency for a proper photon detection. Moreover, the composite scintillators showed PSD capability with respect to alpha and gamma radiation.
Another way to produce polymeric-based detectors is presented in Chapter 6, where the ZnO powder was embedded in polymerized *n*-hexane through the use of the plasma torch. APPJ allowed for a plasma polymerization of the liquid precursor into thin films with embedded zinc oxide nanopowders. The effectiveness of this production route was dual: on one side the plasma polymerization of liquid precursor, while on the other side the recovery of ZnO optical properties through passivation of the surface defects. Trap levels, in fact, are derived either by the production route or by the annealing treatment, and leads to a decrease of the photoluminescence.
Finally, Chapter 7 reports on the production and doping of zinc oxide thin films via APPJ technique. Atmospheric plasma, in fact, gives the unique possibility to start by aerosol solutions and to obtain doping by simple addition in the liquid state. For this purpose, aluminum-doped zinc oxide was obtained by mixing zinc and aluminum acetate in the aerosol state, followed by plasma reaction. The result was a crystalline structure with substitutional aluminum that exhibit good electrical properties. Although the effectiveness of plasma was proved, the final structure was highly defective, with a detrimental effect on the electron mobility. This feasibility study was carried out with the aim of producing hybrid scintillators. However, the limitations on the final thickness results in poor optical properties, that are insufficient for the realization of a proper scintillator.

Chapter 1

Flexible scintillators and radiation detection

1.1 An introduction to ionizing radiation

The way the impinging radiation interacts and loses energy inside a radiation detector determines the operation principles and modes. In this chapter, an overview on the interaction mechanisms of selected types of radiation with matter is presented. Different radiation of interest will be presented and discussed:

- Heavy-charged particles (α-particles, H^+)
- Electrons (e^-)
- Gamma rays (γ)
- Neutrons (n)

A particular interest is devoted to ionizing radiation, a group that includes all the above mentioned radiations, which carry sufficient energy to detach electrons from molecules or atoms. As general classification, direct or indirect ionization mechanisms can be distinguished. The first category of direct ionization includes heavily-charged particles and electrons, whereas the second category of indirect ionization includes high-energy photons (gamma and X-rays) and neutrons.

Depending on the interaction mechanism, a wide range of penetration depth of impinging radiation should be considered: charged-particles produces strong ionization along the track, therefore can penetrate just few hundreds of microns, while neutral particles interact less and ionize mainly through recoil and therefore can penetrate much more.

A way to exploit these interaction is through scintillating materials, a category of matter grouping a special behavior toward impacting radiation, which is captured and converted into visible photons.

1.1.1 Interaction of heavy charged particles

The primary interaction of heavily charged particles with matter is throughout coulomb-type forces, between the positively charged particles and the negatively charged electronic cloud of the material [14]. The interaction takes place with many electrons as soon as the heavy particle enters the material, and depending on the proximity, it can lead to excitation (the electron is raised to a higher level) or ionization (the electron is removed from the atom shell). This interaction occurs with an energy transfer between the particle and the electron at the expenses of a reduction of kinetic energy. The interaction with the electrons results in a continuous speed decrease up to a complete stop. The paths taken by heavily charged particles are mostly straight, with the exception of the very last part. This translates into the concept of *range*, which represents the average distance that penetrating particles can cover into a certain material.

A more specific definition is the *linear stopping power (S)*, that represents the differential energy loss for a particle per unit length:

$$S = -\frac{dE}{dx} \tag{1.1}$$

This amount (Eq. 1.1) is typically referred as to *specific energy loss* if considered on a particle track.

The *Bethe formula* is the classical expression that describes the specific energy loss as:

$$-\frac{dE}{dx} = \frac{4 \cdot \pi \cdot e^4 \cdot z^2}{m_0 \cdot v^2} \cdot N \cdot B \tag{1.2}$$

where

$$B \equiv Z\left[ln\frac{2 \cdot m_0 \cdot v^2}{I} - ln\left(1 - \frac{v^2}{c^2}\right) - \frac{v^2}{c^2}\right] \tag{1.3}$$

Specifically, in Eq 1.3, the terms v and z represents the velocity and charge of the primary particle respectively. N and Z are the number density and atomic number of the absorber atoms, m_0 is the electron rest mass, e is the electron charge and I is the average excitation and ionization potential of the absorber material.
The first term of Eq. 1.3 becomes predominant when considering non-relativistic charged particles (v « c) and, in general, the expression of B (Eq. 1.3) changes with the particle energy with a trend following $\frac{1}{v^2}$.
Experimentally, this trend corresponds to an increase of time spent nearby an electron when the particle velocity is low, meaning an increase of energy transfer. When plotted, this behavior gives the well known *Bragg peak* near the end of an ionization track (Figure 1.1).

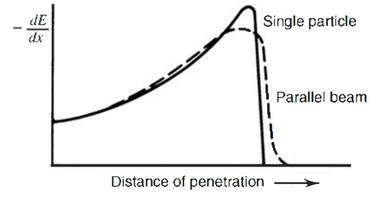

FIGURE 1.1: Linear stopping power along a specific track [14].

In Figure 1.1, the linear stopping power is plotted against the penetration distance for a specific particle track. The two curves presented differs because of the energy straggling effect of a beam with respect to a single particle. This phenomenon is associated with the stochastic nature of energy loss processes for a mono-energetic charged particle beam. The energy straggling is therefore the width of the energy distribution and varies during the particle track.

The definition of *range*, previously introduced, can be refined by considering the definition of *mean range (R_m)* and *extrapolated range (R_e)*. The mean range represents the material thickness that is able to reduce of 50% the particle count with respect to air or vacuum. The extrapolated range represents the extrapolation to zero of the linear portion of the transmission curve of Figure 1.2.

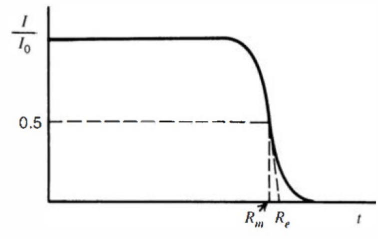

FIGURE 1.2: Definition of mean and extrapolated range in a transmission experiment [14].

The fluctuation of penetration length for charged particles of initial equal energy is defined as *range straggling*. As for the energy straggling, this characteristic of heavily charged particles derives from the statistical nature, and the total range straggling can be up to a few percent of the mean range.

1.1.2 Interaction of fast electrons

If compared to the previous section of heavily charged particles, the rate of energy loss of fast electrons is lower and the trajectory of these in the material is largely non-linear. This almost randomic path is the result of continuous interactions between fast electrons and orbital electrons, as their mass is equal. Additionally, abrupt changes in the penetration direction can derive from electron-nuclear interactions. Fast electrons can lose energy by coulomb interactions but also mainly by radiative processes. These processes are referred as to *Bremsstrahlung* and they can issue energy from any electron track position.

Therefore, in this case the total linear stopping power is the sum of two separate contributions: the collisional losses and the radiative losses (Eq. 1.4).

$$\frac{dE}{dx} = \left(\frac{dE}{dx}\right)_c + \left(\frac{dE}{dx}\right)_r \tag{1.4}$$

The ratio of these two contribution can be approximated to:

$$\frac{\left(\frac{dE}{dx}\right)_c}{\left(\frac{dE}{dx}\right)_r} \cong \frac{EZ}{700} \tag{1.5}$$

where E is the energy expressed in units of MeV.

The typical energies involved in beta particles or secondary electrons interaction are in the range of a few MeV.

Differently from monoenergetic electrons, beta particles emitted by radioactive sources have a continuous energy distribution. For low-energy beta particles, the absorption occurs in a small material thickness, so the attenuation curve is initially sharp. For this purpose, semilog plots are usually adopted to display the thickness against counts, as reported in Figure 1.3.

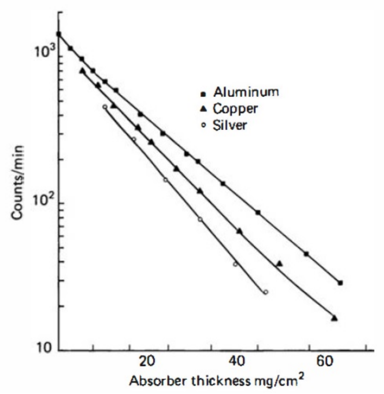

FIGURE 1.3: Detected betas as function of the material thickness [14].

Since the trajectory of fast electrons in the material can be subjected to abrupt variations, the phenomenon of *backscattering* can occur. The fraction of electrons undergoing backscattering is function of the energy and the material. In general, the higher amount of backscattered electrons is detected for high atomic number materials and low incident energies electrons.

1.1.3 Interaction of gamma rays

The interaction of gamma rays with matter consist of a variety of mechanisms, however only three are of interest in radiation detection measurements: *photoelectric effect*, *Compton scattering* and *pair production*.
Depending on the amount of energy transferred from the photon to the electrons, the incident gamma ray can be scattered or entirely disappear.
The importance of these phenomena depends strongly on the atomic number (Z) of the absorbing material, as shown in Figure 1.4.

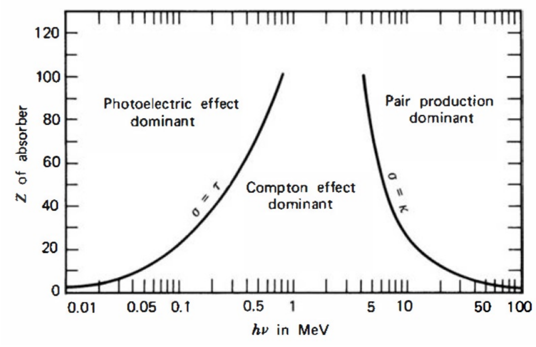

FIGURE 1.4: Importance of the three main interaction processes of gamma rays as function of the atomic number of the absorbing material [14].

In the case of *photoelectric effect*, the energy transfer between the incident photon and the absorbing material leads to a complete energy transfer with photon disappearing. This complete transfer results in the ejection of an electron from the most inner shells of the absorbing material (formerly photoelectron), usually a K shell electron. The energy of the photoelectron is exactly the initial photon energy ($h\nu$) minus the binding energy (E_b) of the original shell of the photoelectron (Eq. 1.6).

$$E_{e^-} = h\nu - E_b \tag{1.6}$$

Since this process ejects an inner shell electron, the atom from which is ejected presents a vacancy in its bound shell, meaning that is formerly ionized. This charge disparity is rapidly filled by electron re-arrangement or free electron capture. However, this process generates characteristic X-ray photons that can be reabsorbed or can escape.

The photoelectric absorption process is characteristic of low energy incident gamma rays and is enhanced for high atomic number absorbing materials.

A single analytical expression of the probability of photoelectric absorption cannot be written, however a rough estimation of this probability is given by:

$$\tau = A \cdot \frac{Z^n}{E_\gamma^{3.5}} \tag{1.7}$$

where A is a constant and the n exponent varies between 4 and 5 depending on the gamma-ray energy.

On the other hand, the *Compton scattering* effect takes place when an incident gamma ray (mainly coming from radioactive sources) transfers only a portion of its energy to an electron, that is initially assumed to be at rest. This partial energy transfer deflects the incident photon, that becomes a scattered photon, and induces the motion of the initially stationary electron that becomes a recoil electron (Figure 1.5).

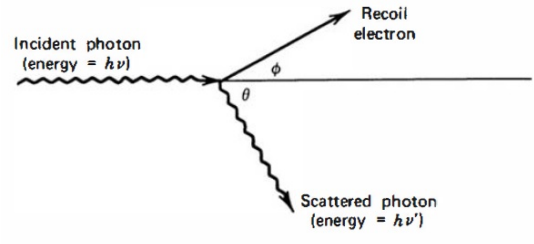

FIGURE 1.5: Compton interaction and products [14].

The effect shown in Figure 1.5 can be expressed by writing simultaneously the energy and momentum conservation, and deriving:

$$h\nu' = \frac{h\nu}{1 + \frac{h\nu}{m_0 \cdot c^2}(1 - cos\,\theta)} \tag{1.8}$$

where $h\nu$ is the incident photon energy and $m_0 \cdot c^2$ is the electron rest-mass energy (0.511 MeV).

Therefore, the neat energy of the recoiled electron is:

$$E_{e^-} = h\nu - h\nu' \tag{1.9}$$

The amount of energy transferred is related to the scattering angle (θ): for $\theta = 0$ no energy is transferred, while the maximum energy is passed for $\theta = \pi$, even though some of the original energy is retained by the incident photon.

The angular distribution of the scattered photons is function of the incident energy and can be predicted using the *Klein-Nishina* formula [14].

The dependence of the of the amount of transferred energy with the scattering angle explains the continuum nature of of the Compton energy spectrum, that ends with a sharp cut-off known as the *Compton edge* for $\theta = \pi$.

Finally, *pair production* is the phenomenon with statistically higher probability when the gamma energy exceeds twice the electron rest-mass energy ($E > 2 \cdot m_0 \cdot c^2 = 1.02\, MeV$). As a practical matter, the pair production occurs predominantly with high-energy gamma rays. The interaction consists in the total energy loss of the incident gamma, that disappears while an electron-positron pair is created. The energy exceeding twice the rest-mass is converted into kinetic energy for both the electron and the positron.

The total energy of the pair is:

$$E_{pp} = h\nu - 2 \cdot m_0 \cdot c^2 \tag{1.10}$$

For all the above mentioned cases, it is possible to define a *linear absorption coefficient* that represents the sum of all the contributions (exponential attenuations) of single interactions.

For gamma ray interactions, a *mean free path (λ)* can be defined as the average distance in the material before the interaction occurs.

1.1.4 Interaction of neutrons

Oppositely to heavily charged particles and fast electrons, neutron does not carry any charge, therefore no Coulomb interaction is possible with the absorbing material. The result is that neutrons can travel several tens of centimeters without interacting with the material, meaning that is "transparent" to conventional detectors. The interaction of neutrons occurs with the nuclei of the absorbing material and it results in secondary radiations or neutron partial energy loss.

Secondary radiations derived from a neutron interaction are almost always charged particles, as the interaction results in neutron-induced nuclear reactions or an increase of nucleus energy.

It is common to treat neutrons based on their energy and two categories are generally employed: fast neutrons and slow neutrons. The cut-off energy between these two classes is the cadmium abrupt drop of the absorption cross section (about 0.5 eV).

Slow neutrons interacts with matter through elastic scattering and a set of neutron-induced nuclear reactions that scales with $\frac{1}{v}$ (Figure 1.6).

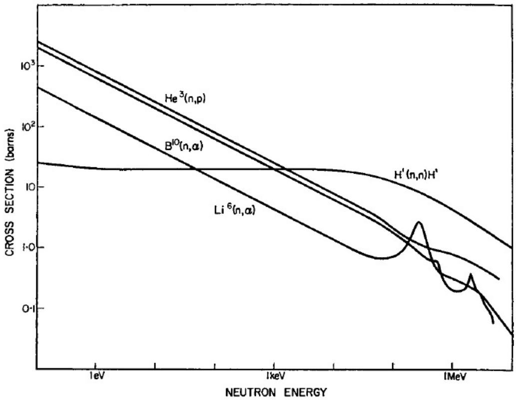

FIGURE 1.6: Neutron absorption [1].

The reduced amount of kinetic energy is not sufficient for an effective energy transfer so the detection cannot be based on this principle. However, the neutron-matter interaction throughout elastic scattering can lead to a thermalization (in thermal equilibrium) of the neutron in the absorbing medium before other interactions takes place.

Therefore, neutron-induced nuclear reactions are the most relevant interaction for slow neutrons, owing to the creation of secondary radiations with sufficient energy to be detected directly. This involves generally the emission of heavily charged particle in (n,α) or (n,p) reactions. Among these reactions, the most common involves ^{3}He, ^{6}Li and ^{10}B atoms because of their large interaction cross section.
The ^{3}He neutron detectors take advantage of the reaction:

$$ {}^{3}_{2}He + n \rightarrow {}^{3}_{1} H + p + 0.764\, MeV \tag{1.11}$$

Differently, ^{6}Li detectors are based on the reaction:

$$ {}^{6}_{3}Li + n \rightarrow {}^{3}_{1} H + \alpha + 4.78\, MeV \tag{1.12}$$

Similarly, also the ^{10}B detectors are based on an (n,α) reaction:

$$ {}^{10}_{5}B + n \rightarrow \begin{cases} {}^{7}_{3}Li + \alpha + 2.79\, MeV \\ {}^{7}_{3}Li^{*} + \alpha + 2.31\, MeV \end{cases} \tag{1.13}$$

$$ {}^{7}_{3}Li^{*} \rightarrow {}^{7}_{3} Li + \gamma + 0.48\, MeV \tag{1.14}$$

The importance of neutron-induced nuclear reactions drops down dramatically with the increase of neutron energy, where the kinetic energy increases and scattering phenomena becomes predominant. The interaction with the absorbing material generates secondary radiations in the form of recoil nuclei, and at each scattering center the neutron is moderated.
The recoil energy is given by:

$$ E_r = \frac{2 \cdot m_{nucl} \cdot E_n}{(A+1)^2}(1 - cos\, \alpha) \tag{1.15}$$

where m_{nucl} is the mass of the nucleus, E_n is the neutron kinetic energy and α is the neutron scattering angle. The maximum amount of energy is transferred for $\alpha = \pi$. For the case of $m_{nucl} = 1$ (i.e. hydrogen atoms), $E_r = E_n$ meaning that the entire neutron energy is transferred to the hydrogen nucleus. This explains the use of hydrogen-rich materials to attenuate fast neutrons for shielding and detection purposes.

For the detection of fast neutron, organic scintillators, rich in hydrogen, are typically employed. In particular, the scintillator detect the protons scattered from the organic molecules. If the neutron energy is sufficiently high, the inelastic scattering phenomenon can occur, with the excitation of the nucleus to a higher energy state, whose relaxation produces a gamma ray.

1.2 Scintillation basis

As anticipated before, if the radiation impinges on a scintillating material, the interaction and energy transfer can induce one or more phenomena like excitation, ionization and de-excitation. Electronic excited states can produce light or result in a non-radiative de-excitation process, also known as quenching [15].

The process of light production upon excitation by an ionizing radiation is called radioluminescence or scintillation. This category includes excitation by X-rays, gammas, neutrons, alpha and beta-particles, together with other more exotic sources.

Many different types of radiation detectors are sensitive to impinging radiation: ionization chambers, Geiger-Müller counters, liquid counters, solid counters, Čerenkov counters, dosimeters, track visualization instruments. Among the solid counters, scintillation detectors offers the best balance between versatility, cost and easiness. Additionally, the variety of radiation types and wide energy range makes them competitive.

In general, the ideal scintillating material should possess:

- high scintillation efficiency, meaning a good conversion into detectable photons
- linear conversion, meaning that the amount of light should be proportional to the energy deposited
- high transparency for a good light collection
- short decay time to produce fast signals

- a refractive index as close as that of glass, to permit an efficient coupling with conventional detectors

1.2.1 Organic scintillators

Organic scintillators includes pure crystals, liquids and plastics. The most studied and reference material is still anthracene, an organic crystal with high light yield but extremely fragile and difficult to be obtained in large sizes.

By dissolution of organics in solvents one can obtain liquid scintillators, characterized by high radiation hardness and a limited cost. However, the solvents involved in the dissolution process are generally toxic, difficult to handle and oxygen sensitive.

Finally, plastics (Figure 1.7) represents a family of cheap organic scintillators that are relatively easy to be produced through polymerization of aromatic monomers. They are easy to handle, they can be produced in a variety of shapes and simple to scale-up, since the polymerization starts from liquid batches. The addition of organic dyes is simple and can efficiently activate the scintillation process, through wavelength shifting and reduction of the self-absorption. The most studied and available plastic scintillators are poly-vinyl-toluene (PVT) and polystyrene (PS) based scintillators. They are widely used in security radiation systems as they represent the only practical choice for large-volume solid detectors.

In the last decade, poly-siloxanes have also been investigated for scintillation purposes. They do not belong to the family of plastics, since they are elastomers, but they display good flexibility, high temperature stability and good radiation hardness.

The main weakness of organic scintillator, in fact, resides in the low radiation hardness if compared to inorganic crystals. A variety of studies have been reported about the radiation damaging of organic scintillators. The amount of radiation necessary for damaging an organic scintillator is measured as dose or equivalent dose (Gy) which means the energy deposited by one joule per kilogram of mass. For polymers and plastics, the threshold dose is about $10^3 \div 10^4$ Gy, but there are also radiation-resistant plastics that can withstand 10^5 Gy [14].

The observed changes upon exposure varies for the decrease of light output due to damaging of the luminescent component up to the decrease of optical transparency, due to the creation of absorption centers. A key factor is the presence of oxygen, which can lead to a non-recoverable damaging because of its interaction with the radiation that forms radical species. In plastics, the most common damaging after exposure to radiations in air is represented by the yellowing, i.e. transparency reduction, due to radicals and trapped electrons.

FIGURE 1.7: Plastic scintillators under UV light excitation [16].

In organic materials, the interaction with matter generates transitions in the energy levels of a single molecule, therefore the fluorescence can be observed independently from the physical state. For example, anthracene can emit light upon interaction either as a solid crystal or as vapor.

The specific electronic structure of molecules, that is responsible for light emission upon excitation, gives rise to the classification into two categories: conjugated molecules and aromatic organic molecules.

These are characterized by weakly bounded π-electrons that can easily jump to the excited states. This situation is well schematized in the Jablonski diagram reported in Figure 1.8.

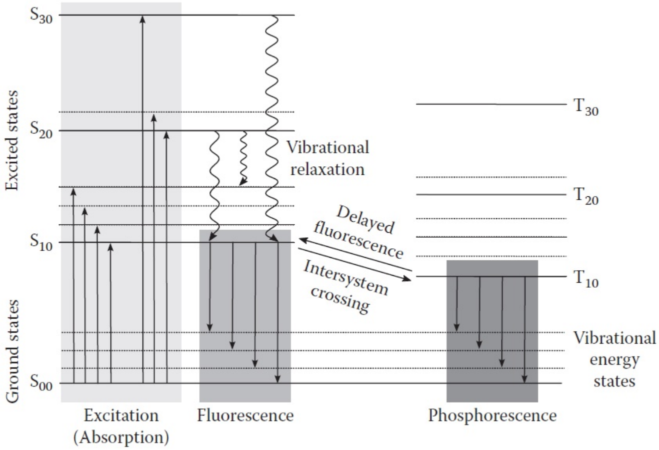

FIGURE 1.8: Jablonski diagram of the π-electrons in a molecule [15].

The majority of scintillation contribution is derived by the population of the S_{10} level which is the first excited state at ground vibrational level, since the excess of vibrational energy is rapidly lost to reach the thermal equilibrium.

Upon excitation, the molecules can release their energy in a variety of different processes, depending on the system complexity. In one-type molecule systems, the main de-excitation processes are fluorescence, since the singlet-singlet transition is preferential, or internal conversion.The first emits visible light while the latter is a non-radiative process. If the intersystem crossing (ISC) process occurs, the energy is transferred for a singlet to a triplet state and the result is a delayed fluorescence, better known as phosphorescence.

Another important parameter is the distance between the first absorption band and the emission associated with the same electronic transition. This is generally known as Stokes shift and should be carefully evaluated with organic scintillators, since the overlap of the absorption and emission bands occurs frequently and the process of self-absorption should be minimized.

Three categories of organic scintillators can be pointed out: unitary systems, binary systems and ternary systems.
Pure crystals represents the first category, while scintillating materials embedded in a matrix or dispersed in a solvent belongs to the second category.
The third and more complex category is composed of a scintillating material and a wavelength shifter dispersed in a matrix or solvent. The role of the wavelength shifter is crucial, since it absorbs the light emitted by the primary scintillator and re-emits it to a higher wavelength. However, the complexity of a three-component system does not always result in radiative transfer process, as well explained by Figure 1.9.

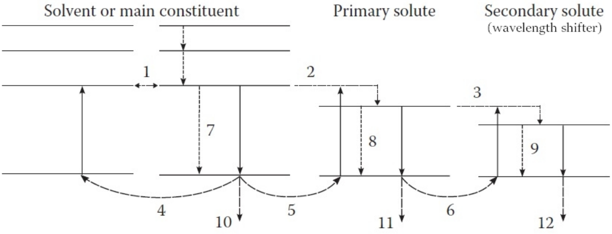

FIGURE 1.9: De-excitation in ternary scintillating systems [15].
1: Non-radiative molecular transfer
2: Non-radiative molecule to solute (primary) transfer
3: Non-radiative solute to wavelength shifter transfer
4, 5, 6: Radiative transfer
7, 8, 9: internal quenching
10, 11, 12: Emission of light from one or other components of the system.

In general, other de-excitation processes can occur and become competitive with fluorescence if the lifetime is comparable to the time of these processes.
An important parameter for selecting a good scintillator is its light output. This strictly depends on the nature of the scintillator whereas to the type and energy of the ionizing particle. Especially for organic scintillators, the light emission is also dependent on the damage of the scintillator

itself. Exposure to light, oxygen and also radiation can cause performance degradation in terms of light output but also structural degradation in the case of polymers [15].

Concepts related to the light output, of fundamental importance in this thesis, are the rise-time and fall-off or decay time. Formerly, for plastic scintillators, both of these parameters should be taken into account, but generally the rise-time is much faster than the decay time, so a simplification can be made.

The most adopted model for the light decay analysis is the exponential decay model:

$$n(t) = \frac{N}{\tau} \cdot e^{-t/\tau} \tag{1.16}$$

As previously mentioned, two types of fluorescence can occur, each characterized by a decay time that is either short (few nanoseconds) or long (hundreds of nanosecond).

The response of most organic scintillators is a combination of these two fluorescent components, therefore a complete analysis should take into account a fast and a slow component. The amount of light associated with the fast or slow component depends on the nature of the exciting particle. This means that the shape of the response can give information about the kind of particle that deposited the energy, allowing for the well-known pulse shape discrimination (PSD) feature, that will be deepened later in Section 1.2.4. The most common use of this element is for counting neutrons in presence of gamma radiation, as explained in Figure 1.10.

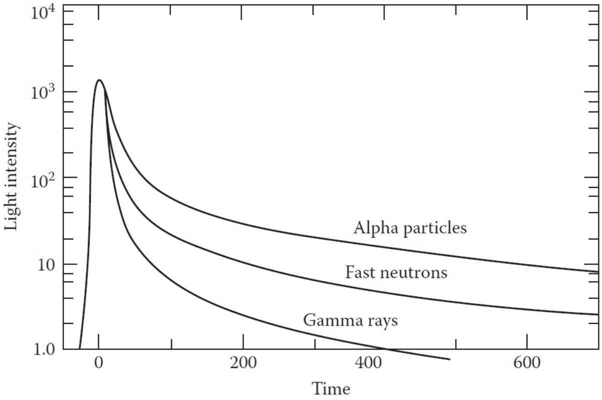

FIGURE 1.10: Time response to different kind of exciting particles for a stilbene crystal [15].

Up to now, it was considered that all the energy absorbed by the scintillator is lately converted into light. This is true only for ideal scintillator, while for real systems the scintillation efficiency parameter should be considered. This variable accounts for the fraction of energy deposited and converted into scintillation light. However, this also depends on the spectra emission region considered, since one of the most common standard is Anthracene, that has an absolute scintillation efficiency of 5% in the blue spectral region. A common way to express the scintillation efficiency is to express it as photons produced per unit of absorbed energy (ph/MeV).
The efficiency is also strongly affected by the particle energy and type, since the response for electrons is higher than that for heavy particles.

1.2.2 Inorganic scintillators

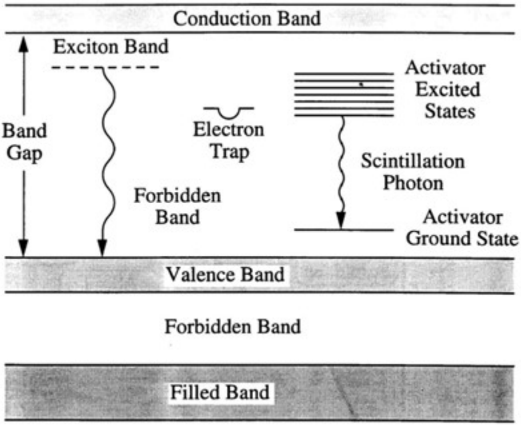

FIGURE 1.11: Band structure in inorganic scintillators.

Scintillation in inorganic materials depends on the energy states available in the band structure of the crystal lattice (Figure 1.11). The availability of electrons is limited to discrete bands of energy: the lower, *valence band*, represents the lattice sites where electrons are bound, the higher, *conduction band*, represents the level at which electrons are free to migrate throughout the crystal. The region comprised between these two bands is called *forbidden band* because no electrons can never be found, if the crystal is pure. Since this gap is generally wide, so that excited electrons returning to the valence band cannot emit visible photons, small amount of dopants (i.e. impurities) are added. The role of this material (commonly called *activators*) is to create levels in the forbidden band, that are normally not available. These are extremely important because in the de-excitation process gives new path with low energy, that translates in the formation of visible photons. These levels are generally referred as to *luminescence centers*.
When a charged particle hits the detector material, a large number of electron-hole pairs are created as a consequence of the transition of electrons to the conduction band. The holes can drift to the activator sites and ionize it

while the electrons can travel freely in the crystal. Once they reach an ionized activator site, they can recombine to create a neutral configuration by emitting a photon. The photon energy (i.e. wavelength) depends on the position of the luminescence centers within the bandgap, that can be tuned by changing the active material. The half-life of excited states is in the range of 50-500 ns typically [14].

Alternatively, there is the possibility of combined migration within the crystal of the electron with the associated hole in a loosely configuration, also known as *exciton*.

A rough estimation of the scintillation efficiency can be obtained by considering that about three times the bandgap energy is required to create an electron-hole pair in a certain material.

A great advantage of luminescence through activation sites resides in the transparency of the crystal with respect to the scintillation light. This is a direct consequence of the activator sites present in the crystal energy structure. The reduction of the transition energy results in an emission shift to longer wavelength that will not be influenced by the crystal self-absorption.

The most common and studied inorganic scintillators are the alkali halide family, like *NaI(Tl), CsI(Tl), CsI(Na)* and *LiI(Eu)*. The decay times of this family of scintillators is generally slow, in the order of several hundreds of nanoseconds. Other slow inorganic crystals, with decay times > 200 ns, are bismuth germanate (BGO, $Bi_4Ge_3O_{12}$), cadmium tungstate ($CdWO_4$), silver-doped zinc sulphide (ZnS:Ag), europium-activated calcium fluoride (CaF_2:Eu), Yttrium Aluminium Perovskite cerium-doped (YAP:Ce) and others.

All these crystals are characterized by a high light yield and good radiation hardness. However, their cost is generally high and the scalability not possible, since the most common production process is melt-grown from liquid phase. They are fragile, therefore their handling is not easy and they are not suitable for many applications.

1.2.3 Scintillation detectors

The light emitted after a radiation interaction should be captured by an appropriate detector, that generally does the conversion to an electrical signal.

For many years, photomultiplier tubes (PMT) have accomplished this task of conversion with effectiveness, even though in the last decades semiconductor photodiodes have emerged for some specific characteristics.

The simplified scheme of a classical PMT is reported in Figure 1.12 where the two main components can be found: the photosensitive material (photocathode) and the multiplication structure.

The photocathode has the role of converting the incident photons into electrons, but since generally the amount of photoelectrons involved is small, their charge would not be enough to generate a sufficient electrical signal. To overcome this limitation, an electron multiplication structure is coupled with the photoactive material in order to generate a sufficient amount of electrons and therefore to give a good signal output. A typical PMT amplification structure consists of 12-15 dynodes that can finally generate $10^7 \div 10^{10}$ electrons. The output signal is collected at the anode. The amplification response of the majority of the commercially available PMTs is strongly linear, meaning that an increase in the input light produces a linear increase of the electrical output.

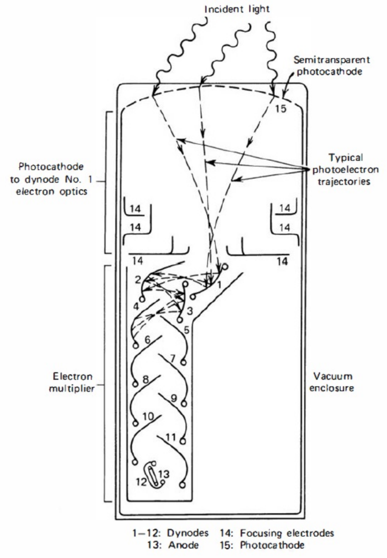

FIGURE 1.12: Classical photo multiplier tube structure with 12 dynodes [14].

Typically, PMT detectors are characterized by a delay of 20-50 ns and pulse width of few nanoseconds.

Among the important parameters of PMTs, the *(quantum efficiency* accounts for the goodness of the photo-conversion process, meaning that is defined as the ratio between the number of photoelectrons emitted over the number of incident photons. This values ranges between 20-30% for commercially available PMTs, making them less efficient than photodiodes.

Mainly for this reason, but also related to a more efficient power consumption, silicon-based photodiodes have gained importance in the last decades. They are generally more compact, slightly faster and insensitive to the magnetic field, making them a good substitute in many experiments. Two main classes of photodiodes are available: conventional photodiodes and avalanche photodiodes. The first is characterized by no internal gain, while the second by an enormous internal gain derived by the strong electric field present.

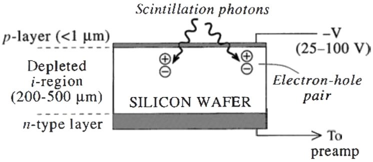

FIGURE 1.13: Conventional photodiode scheme [14].

Conventional photodiodes (schematized in Figure 1.13) presents a very high quantum efficiency (up to 60-80%) and can cover a wider wavelength range than a PMT (but always limited to the silicon absorption range) but requires an external amplifier. This lack of amplification becomes important when operating in pulsed mode, where just a bunch of photoelectrons are produced, and the electronic noise can be a significant contribution of the output. This limitation is effectively overcome with the use of an avalanche photodiode, in which the avalanche process is used to increase the signal output with respect to noise. In this process an electron absorbed in the depleted region is subjected to a big acceleration, imparted by the strong electric field. This gives a sufficient kinetic energy to trigger a cascade process of kinetic energy transfer from electron to electron, leading to the multiplication of the initial signal by ionization of electrons that are initially at rest. The gain that can be achieved depends on the temperature and is an exponential function of the applied voltage, since on an APD it should be enough high to work in *Geiger mode*, above the breakdown voltage (V_{bd}).

Regarding the timing performances of APDs, in general the electron drift with respect to the impinging position gives the biggest contribution to the timing uncertainty, leading to a typical response time of few nanoseconds [14].

Another limitation of APDs is derived from the time required to quench the avalanche and return to the initial bias voltage.

1.2.4 Pulse Shape Discrimination (PSD) capability

The pulse shape discrimination (PSD) capability of a system is the ability to discriminate different impinging particles. The excitation mechanism induced by an impinging high-energy particle in an organic solid scintillator generates ionized molecules in the matrix and the dye, that can subsequently recombine in a process known as ion recombination. The excited states resulting from ion recombination are mainly triplet states (T_n) with an abundance of 3:1 respect to singlet states (S_n). Moreover, the interaction of a high-energy particle with the material generates a high density of excited states along the particle track. For this reason, bimolecular reaction involving higher excited states can occur, resulting in a process called ionization quenching. This resulting process is very fast and directly competes with the internal conversion process for the relaxation of singlet and triplet states to their first-excited level. The importance of this process depends on the specific energy loss (dE/dx), explaining the reasons behind a higher scintillation light yield of electrons compared to alpha particles with the same energy. This light is the result of a bimolecular annihilation of triplet states (generally denoted as triplet-triplet annihilation, TTA) that produces an additional singlet excited state (Eq. **??**).

$$T_1 + T_1 \rightarrow S_0 + S_1 \tag{1.17}$$

This mechanism is occurring relatively easy in liquid media but is not favorable in solid scintillators, where the dye molecule distance cannot change. For these reasons, the scintillation light is characterized by two components: a prompt fluorescence and a delayed fluorescence (Figure 1.14a). The former resulting from singlet state de-excitation while the latter being the de-excitation from singlet state after the TTA event. Since this second mechanism takes more time to occur, the resulting fluorescence will be characterized by a slower component, giving the basis for the PSD technique with time-resolved measurements.

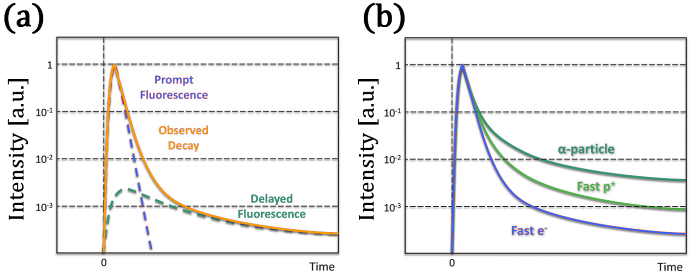

FIGURE 1.14: (a) Difference between prompt and delayed fluorescence and (b) interaction of particles with different specific energy loss.

As visible in Figure 1.14, the interaction of a radiation with scintillating materials produce a signal that is generally a pulse with a certain amplitude and with an associated time of occurrence. Besides the amplitude, also the shape can assume an importance when treating radiation interactions. In particular, the interaction of different particles with the material can give rise to different energy transfer processes, therefore the light produced, i.e. the current recorded, can have a different rise time. To exploit this information, pulse shape discrimination (PSD) methods have been proposed. These techniques can allow to discriminate the contribution of different impinging radiations, therefore allowing to discriminate the background from the real signal. This is the case of organic scintillators used as fast neutron detectors, were the constant presence of background gammas can be a problem for the detection.

Two general approaches were proposed over the years: one is based on the electronic discrimination of the rise time in the pulse, while the other is based on the signal integration over different time periods. Both of the techniques are widely used in the scientific community and depending on the material and radiation type, one can be more effective over the other.

To apply the rise time discrimination, the use of CR-RC-CR networks or double delay line shapers, gives rise to a bipolar shape whose zero crossover point includes the shape information.

Conversely, the second method is based on the charge integration over two different time regions of the pulse. By computing the ratio of these two integrals, one can deduce information about the pulse profile, since common pulses will have an approximately constant ratio. The ratios will have a bi-gaussian distribution, as shown in Figure 1.15.

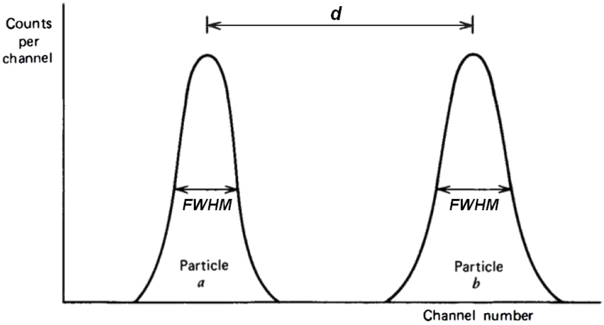

FIGURE 1.15: Distribution of the charge integration ratios [14].

Nevertheless, the performances of this method are severally compromised when the input count rate is high, because of pile-up effects. These effects can be limited if a rejection criteria is implemented to discard pulses occurring too close.

A Figure of Merit (FoM) can be defined to measure the separation of the two distribution peaks, as follows:

$$FoM = \frac{d}{FWHM_a + FWHM_b} \tag{1.18}$$

where FWHM represents the full-width at half-maximum of the distribution and d the distance between the maxima.

1.3 Quantum dots

Semiconductor nanocrystals with size of 1-10 nm displaying quantum confinement effects are generally referred as quantum dots [17–19]. These small crystals possessing outstanding optical properties, such as tunable emission wavelength (Figure 1.16), narrow emission spectrum and fast decay lifetime, makes them ideal candidates for the realization of flexible scintillators.

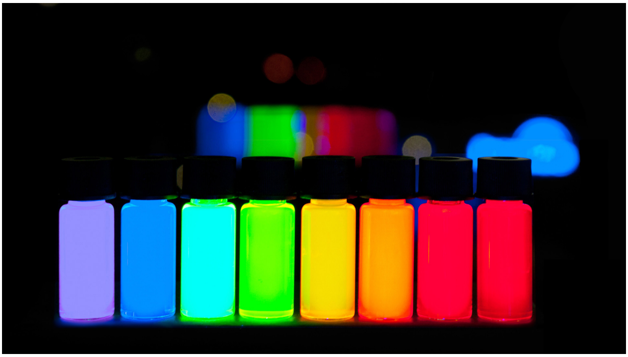

FIGURE 1.16: Optical emission of quantum dots with different size, excited under UV light.

They are generally added to polymeric matrix to increase the average atomic number (Z) and the light yield of the system. Moreover, they can be an effective replacement for the non-emitting nanoparticles that are generally embedded in plastic scintillators. In fact, a main drawback of these non-emitting nanoparticles resides in the proportional decrease of light yield with the loading amount, because of a non-efficient energy transfer and conversion to visible photons. For these reasons, semiconductor QDs have started attracting interest in the last decades. Initial attempts by *Létant and Wang et al.* [20] focused on the embedding of QDs in porous glass as complete replacement for the primary dye. Similar studies were then proposed by *Kang et al.* [21] and *Lawrence et al.* [22] with scintillation experiments under x-ray and alpha particles. However, all these attempts were not able to reveal clearly the impinging radiation with the generation of a photopeak. The main reason behind these poor results resides in the low effective Z of the final composite due to the limited loading amount of QDs, that was contained below 5% wt. to prevent aggregation. Moreover, the small Stokes shift of these nanocrystals can easily result is self-absorption when scaling up the thickness. A possible solution was proposed by *Campbell et al.* [23] with the addition of a conjugated polymer acting as acceptor for the QDs. A substantial scintillation improvement was recorded up to 15% wt. of loading, followed by an abrupt decrease due to aggregation. A major step forward was obtained with the nanocomposites proposed by *Liu et al.* [24], consisting in ternary systems with a dye as third component. In this way, efficient energy transfer was obtained with the increase of QDs content up to 60%. However, such a high level loading cannot be thought as a secondary component but represents the main constituent of the composite, increasing of several orders of magnitude the price and reducing the mechanical stability of the overall system.

1.4 Zinc oxide

Zinc oxide have been widely studied in the 20^{th} century starting to gather attention from 1935 [25]. In the last years, due to the rise of new and promising technologies, the possibilities to grow single crystals and high-quality powders for the realization of opto-electronic and electric devices has become tempting.

Zinc oxide is wide direct-bandgap semiconductor with an energy gap (E_g) of 3.4 eV and a large exciton binding energy of 60 meV at room temperature. Its main advantages are represented by a wide chemistry, a low threshold for optical emission, a good radiation hardness and a well-established bio-compatibility.

The main optical properties are related to the possibility to fabricate UV laser diodes, optical sensors and technological devices taking advantage of nanoscale properties.

In standard conditions (room temperature and atmospheric pressure) the most stable form of zinc oxide is the wurtzite structure (Figure 1.17).

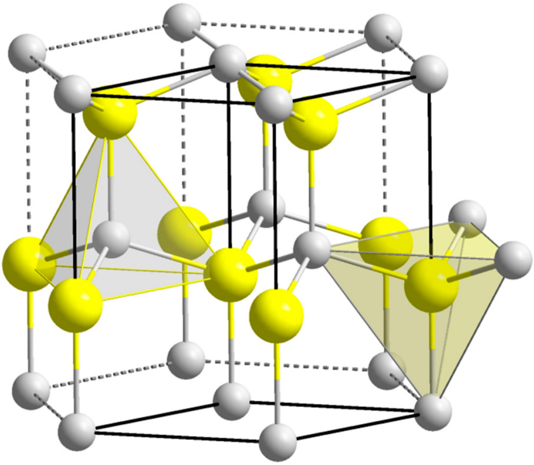

FIGURE 1.17: The wurtzite structure of zinc oxide (Zn in yellow, O in grey) [26].

Wurtzite is a hexagonal lattice (*a,c* lattice parameters) of the space group $P6_3mc$ with tetrahedral coordination of zinc and oxygen ions. This gives rise to polar symmetry along the *c*-axis which is responsible of many properties such as piezo-electricity and spontaneous polarization [25]. Nevertheless, it is also fundamental for crystal growth and defect generation alongside with the determination of a sp^3 covalent bonding structure. However, zinc oxide possesses also a strong ionic character, meaning that its behavior is borderline between a covalent and an ionic compound.

The typical lattice parameters are a = 3.2495 Å and c = 5.2069 Å, with a material density of 5.605 $\frac{g}{cm^3}$ [25].

Other less common crystalline structures of zinc oxide are rocksalt and zincblende.

The electronic structure of this direct bandgap semiconductor is reported in Figure 1.18. The energy bandgap can also be tuned by alloying with MgO or CdO that can increase or decrease the energy bandgap respectively. This is particularly relevant for the fabrication of optoelectronic

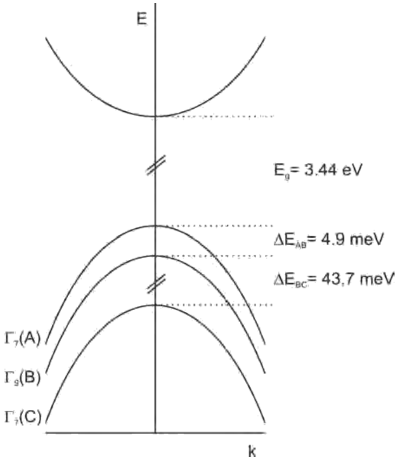

FIGURE 1.18: Zinc oxide experimental valence band split [25].

devices.

The optical properties of zinc oxide are, however, a key point for this material. The optical emission of zinc oxide is concentrated in two main regions of the spectrum: the exciton emission at 385 nm and a large defect-related band ranging from 450 nm up to 650 nm [25]. This broad band, also known as the green band, has been mainly attributed to defects such as oxygen vacancies and zinc interstitials. Zinc oxide is, in fact, commonly obtained in its *n*-type form, meaning that it contains shallow donors such as hydrogen. The application fields for zinc oxide depends mainly on the growing technology: nano-structures are interesting for flat screen displays, gas sensors, chemical sensors and UV light diodes; while epitaxial layers and single crystals are attractive for detectors and transparent thin films. In the form of nanoparticles, zinc oxide is a well-known additive in paints, coatings and sunscreens.

The good radiation hardness to protons have been investigated for possible space applications [25].

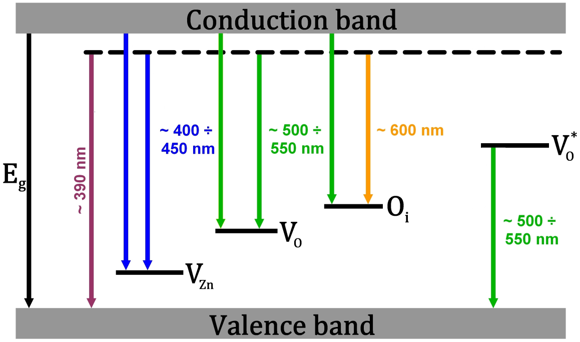

FIGURE 1.19: Zinc oxide band structure with the most common defects (vacancies and interstitials) and associated radiative transitions.

Figure 1.19 shows the zinc oxide band structure with the most common defect levels and associated optical transitions. The near-band-edge recombination occurring at 390 nm, commonly denoted as excitonic transition, is associated to an interstitial to valence band transition. Zinc vacancies (V_{Zn}) are responsible for the blue luminescence, while oxygen vacancies (V_O) for the yellow and green luminescence. Interstitial oxygen (O_i) are generally associated with green to orange emissions, while singly ionized oxygen vacancies ($V_O^\bullet$) [27–29].

1.4.1 Doping and defects in zinc oxide

The attracting interest around zinc oxide and its possible applications in many fields is mainly depending or largely affected by the presence of defects and impurities. Defects can be classified as Zn interstitial or vacancies and O vacancies, while impurities are divided in donor-type and acceptor-type impurities.

The as-grown ZnO was found to be n-type because of the fact that most samples were grown in Zn-rich conditions and, consequently, it was assumed that the main donor was Zn interstitials (Zn_I) or O vacancies (V_O).

However, many studies have confirmed, also by theoretical calculations, that both Zn_I and V_O are deep donors and they have a too high formation energy in *n*-type zinc oxide [30]. Some experiments, have lately proved that Zn_I is actually a shallow donor but still with high formation energy. Within this framework, it has been proved that hydrogen (H) is always a donor in ZnO, because of its low ionization energy and contributes significantly in its conductivity. Indeed, also complexes of Zn_I interstitials are important in conduction.

Other common donor impurities, besides H, are the group III elements such as Al, Ga and In, that can easily substitute Zn in the crystal lattice [31, 32]. Other group VII elements as F or Cl are known to have donor behavior in ZnO [33].

On the other hand, acceptor dopants are considered of greater interest for the realization of *p*-type ZnO for the production of *p*-*n* junctions devices. For this purpose, all the elements of group I (substituting for Zn) and group V (substituting for O) should be considered as candidates. Nitrogen is more likely the ideal candidate because of the small size difference, that can lead to a minimal strain in the lattice. Moreover the electronic structure is close to that of oxygen, but the doping level that can be achieved is low.

Copper was also studied as deep level acceptor able to compensate the *n*-type behavior. However, the role of copper is still under debate because the doping effect has been reported for both the Cu^{2+} and Cu^{+} ionic forms [34].

Silver ions interaction with zinc oxide is either in substitutional of interstitial position. The doping effect reflects on the bandgap energy, but authors are not in good agreement on the real effect of silver ions [35].

However, the most important and dominant acceptor is the zinc vacancy.

In addition to all the point defects mentioned up to now, zinc oxide is always rich in larger defects as dislocations and stacking faults, but these defects are not well known yet.

1.4.2 Zinc oxide for radiation detection

The study of radiation interaction with zinc oxide and doped zinc oxide have attracted interest in the last two decades, although the initial studies are dated in the 60's. Gallium-doped zinc oxide have always been attractive because of its ultra-fast scintillation decay time (< 1 ns) and high light yield (15000 ph/MeV) [36]. Nevertheless, other dopant have been studied, such as indium and zinc [37–40].
The main limitations of these works were relate to the impossibility to produce large single crystals with good transparency, that are essential for the detection of gamma and x-rays. However, powders and thin films, mainly made by hot pressing or hydrothermal growth, are sufficient to evaluate the interaction with neutrons and alpha particles [36].
An important characteristic of this material is its sensitivity to the radiation type and energy, meaning that is possible to realize a particle discrimination. This is extremely important in the radiation detection field since it increase the detector flexibility of use.
The best results for ZnO:Ga were achieved by *Bourret et al.* [41] by reacting ZnO and Ga_2O_3 in a high temperature (400-1100 °C) reducing atmosphere (H_2 rich). The PL spectrum and decay-time under X-ray excitation are reported in Figure 1.20. The hydrogen annealing seem to be effective in

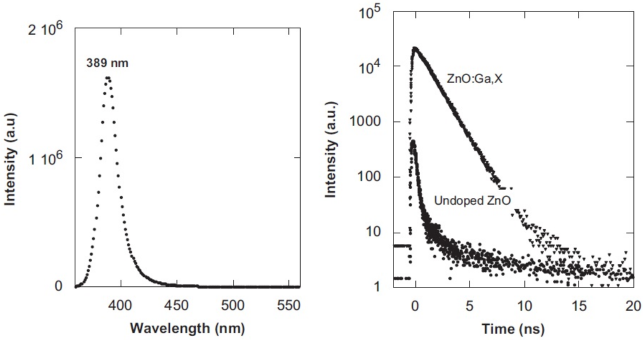

FIGURE 1.20: PL and decay-time of ZnO:Ga samples under X-ray excitation [41].

filling zinc vacancies with hydrogen ions and in removing excessive oxygen, as the lifetime decay is mono-exponential.

In the same work, metallic gallium was also employed for the doping, giving worse results in term of scintillation, but better result in term of conductivity, meaning that the Ga^{3+} donor is present. However, after nitrogen annealing, the UV emission was reduced, supporting the theory that the ultra-fast scintillation is not due to nitrogen acceptors.

In another work by *Chen et al.* [42] the scientists worked on a ZnO:Ga single crystal scintillator made by hydrothermal synthesis. The response was measured under a variety of charged particles with different energy ranges. The main results are summarized in Table 1.1.

Particle type	Energy (MeV)	Range (μm)	τ (ns)
β	0–1.173	1310 for 1.173 MeV	1.09 ± 0.02
H^+	15	692	1.21 ± 0.02
Li^+	42	100	1.50 ± 0.03
α	5.48	13	1.56 ± 0.03
O^{8+}	100	34	1.70 ± 0.04

TABLE 1.1: Decay time response under different charged particles interaction, fitted with single exponential model [42].

These results highlights a energy-dependent behavior, that makes this scintillator promising for ultra-fast pulse-shape discrimination (PSD).

A composite plastic scintillator embedding ZnO:Ga was proposed by *Buresova et al.* [12], in which they embedded luminescent particles in a polystyrene matrix. The resulting composite showed low transparency with 1 mm thick samples and 10 % wt. loading, but superior scintillation behavior with an effective and efficient non-radiative energy transfer between the matrix and the powder. The efficiency was evaluated to be up to 90 %, being the emission of the PS matrix negligible whereas the emission of ZnO:Ga predominant and ultra-fast in the picosecond range. Such properties can be employed in alpha-particle detection and low energy photon (UV) bean monitoring with exceptional timing information. By decreasing the thickness to about 1/5 of the original value, good transparency values can be achieved, making these scintillators usable in practical applications. Regarding other group III dopant, indium-doped zinc oxide (ZnO:In) was studied mainly by Pejchal and co-workers [43] for the realization of both thin films and bulk single crystals. In their study, hydrothermal grown samples were tested under a femtosecond pulsed laser (λ_{em} = 260 nm) showing a bi-exponential behavior with sub-nanosecond emissions. Additionally, *Yanagida et al.* [44] and *Kano et al.* [45] reported on the effects of dopant concentration on the alpha-particle excitation and excitation dynamics, respectively.

A completely different world is represented by Zn-rich ZnO (ZnO:Zn), that shows longer decay time ($\approx$ 10 ns) and the possibility to embed ^{6}Li particles [39, 40]. ZnO:Zn phosphors were studied for optical-related applications, such as for the production of field emission displays [46], flat panel display [47] and opto-electronic component [47, 48]. However, interesting scintillation properties were highlighted in a few works by *Wang et al.* [49], *Derenzo et al.* [50], *Demidenko et al.* [51] and *Li et al.* [52]. In general, the modification of oxygen and zinc defective levels induces a remarked green luminescence that can be tuned with the reduction temperature. Moreover, the luminescence yield has been reported to be growth-dependent and atmosphere-sensitive [40]. Interestingly, radioluminescence (RL) under X-rays proved the superior scintillation behavior of ZnO:Zn over undoped zinc oxide [49]. Additionally, the detection efficiency was reported to be an order of magnitude higher for the defective band scintillation emission [40].

Chapter 2

Atmospheric Pressure Plasma Jets

2.1 An overview on APPJ technologies

Atmospheric pressure plasma jets have attracted increasing interest in the last years, mainly for their flexibility and low cost. The possibility to work in atmospheric conditions translates in a big advantage in terms of complex 3D geometries that can be treated and maintenance, because traditional plasma systems requires pumps and vacuum chambers that limits the treating dimension and increases costs [53]. Additionally, the integration on an atmospheric pressure device in current working lines is much easier and can cover bigger areas, with increase productivity. A particular attention should be devoted to the selection of deposition parameters to obtain a repeatable process with homogeneous deposition.

An atmospheric pressure plasma torch has the possibility to treat different substrates in different working conditions. One of the biggest advantages is the possibility to work in close to room temperature conditions, meaning that the temperature reached on the substrate is low enough for treating skin and heat-sensitive polymers. This opens to the world of biomedical applications, both for cleaning surfaces and treatment of skin, but also to deposit bio-derived materials, such as silk and silk-fibroin.

The three main processes that an atmospheric plasma torch can develop are: surface processing, surface deposition and etching [53]. These three processes are completely different as they deal with different ranges of power, temperature and chemical environment.

Surface processing belongs to the big category of surface treatments, as this typically means a surface cleaning or activation. This is extremely interesting because the surface activation process leads to an increase of the chemical-physical interaction of the surface with matter. This can also be a surface grafting, with the addition of surface molecules that can promote the selectivity of surface chemical reactions.

Another interesting possibility is surface deposition, that we explored in depth. This technology combines a highly-reactive environment with chemical species added via external feeding systems, inducing reactions in the plume and depositing the products on different kind of substrates. The plasma atmosphere overcomes the energy barrier for many reactions not only because of the plasma temperature but also thanks to the high density of excited states and electrons that are peculiar of a plasma environment.

Finally, another possibility offered by this technique is the surface etching. The etching process is quite complex, since it is realized by a flux of ions. However, the equilibrium between the ion power and the substrate heating is crucial, in order to maintain the substrate properties. In general, the etching rate is strongly affected by plasma power and gas flow.

In the family of atmospheric pressure plasma jets, many different solution and geometries have been proposed over the last years. The technological advances of the last two decades were pushed by the increasing interest in application in areas such as medicine [54, 55], nanomaterial synthesis [56–59] and surface engineering [56, 60, 61] . A big contribution came from the medicine and biological field to develop and understand the mechanisms of operation at atmospheric pressure. APPJ non-equilibrium capability translates in close-to-room temperature operation conditions that are favorable for the treatment of living cells and tissues.

The main feature of this class of plasmas resides in the ejection of the plasma outside the generation region. This is possible if a series of parameters, such as the source design, the electric field geometry and the gas flow, favors the extraction and propagation of the plasma outside the generation region up to several millimeters. The degree of interaction between the plasma and the substrate can be selected also by tuning the relative distance.

Although many different configurations were proposed, common features can be highlighted and are schematized in Figure 2.1.

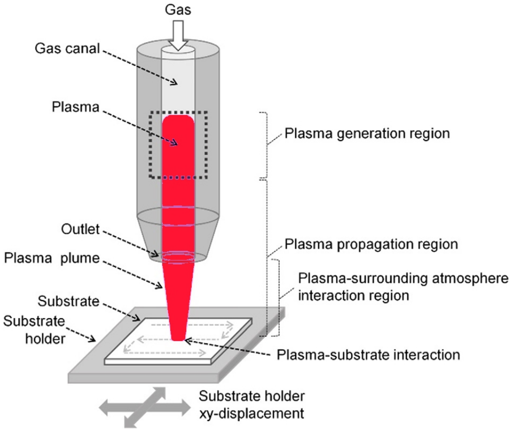

FIGURE 2.1: General scheme of an atmospheric pressure plasma jet including the electrodes and the gas flow channels [53].

In general, an atmospheric pressure plasma apparatus is composed of the electrodes for the plasma generation and the channels for the plasma generation and propagation (Figure 2.2). The gas flowing in the channel determines the plasma propagation direction up to the outlet, where the plasma is ejected in the so called plasma plume. The outlet is usually round-shaped or annular, as it has the same dimension of the channel, but can also be convergent, which reduces the cross-section thus increasing the gas flow and promoting the plasma extraction.

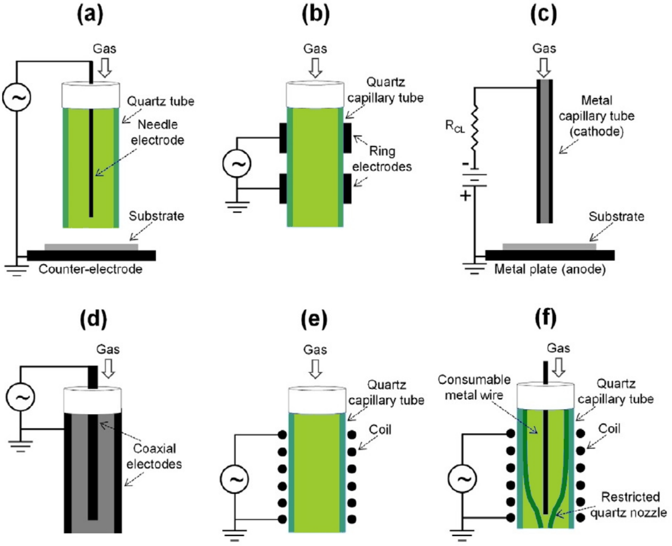

FIGURE 2.2: Common electrodes and channel geometries for atmospheric pressure plasmas [53].

A brief classification can also be done depending on the outlet dimensions, meaning that a narrow circular outlet is generally refered as to "point plasma source" while a high-aspect ratio rectangular window as to "linear plasma jet".

Circular outlet geometries have channels with dimensions from hundreds of microns up to few millimeters, while ring-shaped and rectangular-shaped can expand up to few centimeters. The gas channel cross-sectional dimensions are, in fact, strictly related to the necessity of generating an atmospheric plasma. This implies that high gas breakdown voltages should be reached, thus limiting the distances to narrow gaps. This also helps in keeping the high voltage as low as possible, avoiding the plasma discharge region [62–65].

Another critical aspect of the design, is the proper choice of materials being in contact with the gas and plasma. Metals are generally used for "bare metal electrodes" while insulating materials such as alumina, glass or silica are used in the case of "dielectric-covered electrodes".

Additionally, the channel geometry can be complicated with the introduction of additional channels for feeding vapors or aerosol solutions of chemical precursors.

For all the atmospheric plasmas, the discharge gas are selected among the family of noble or inert gas, meaning that helium, argon, nitrogen or other gas mixtures are preferred.

In a basic geometry configuration, any precursor can be added directly to the discharge gas in the plasma source. This helps increasing the precursor activation and fragmentation but fails inducing the deposition at the electrodes.

To overcome this problem, a coaxial channel solution can be adopted to feed the precursor through a second channel, before or after the device outlet. Usually the aerosol or vapor gas carrier is the same as the discharge one, leading to a dual role of this gas: the plasma generation and the precursor transport and injection. This technological advancement avoid the deposition of precursors in the plasma device, leading to a lower maintenance required and easier cleaning.

For specific configurations, the precursor can also be in the form of solid metal wire, that consumes upon interaction with the plasma, and leads to the deposition of thin films or nanostructures.

The non-equilibrium condition characteristic of atmospheric plasma is quite difficult to be maintained during the plasma generation, since the collision frequency between electrons and gas atoms is high, and the latter should stay close to room temperature while the electron temperature is always much higher [66, 67]. To sustain this process, different strategies should be exploited regarding the electrode geometry, the presence of dielectric barriers to avoid arc formation, the high gas flow to avoid overheating and a high-frequency alternating-current (AC) plasma excitation. The plasma temperature of atmospheric pressure plasma devices ranges from room temperature at the substrate level, up to several hundreds of degree Celsius in the plasma generation region. This is an important difference, because even though the plasma temperature can be quite high in the generation region, the application of technological strategies can lead to a cold atmospheric pressure plasma at the substrate level, meaning it to be still useful to treat heat-sensitive materials.

A possible classification is based on the identification of specific type of strategies applied to obtain the non-equilibrium condition, in particular: based on discharge cell design or based on the high-frequency plasma generation. Asymmetric electrode geometry, sub-millimeter plasma confinement and dielectric barriers belongs to the discharge cell design family [56, 63, 65, 68, 69], while radiofrequency and microwave plasmas to the second family [63, 64, 70].

2.1.1 Discharge cell design

In the family of strategies for different cell design, corona discharges (CD) are made of highly asymmetric electrodes, such as point-to-plane, wire-to-plane or wire-to-cylinder. The small metal electrode, upon the application of a high voltage, creates a strong electric field due to its curvature radius. The gas ignition is therefore obtained close to the electrode, but with a careful voltage raise, can be extended up to the counter-electrode. The discharge, however, should not reach it, otherwise the plasma regime changes from corona to arc, with an increase of the ionization degree.

Corona discharge devices can be powered by both direct current or alternating current supply, with values ranging up to several tens of kV. The most stable non-equilibrium plasma form for corona discharge is obtained with pulsed-power supply, with pulse width in the order of few hundreds of nanosecond, sufficiently short to avoid the arc formation [65, 69, 71]. These plasmas can be fed with air or nitrogen, and different commercial products are available on the market.

Dielectric barrier discharge (DBD) can achieve the non-equilibrium conditions thanks to a dielectric barrier in between the electrode and the counter-electrode [72–74]. The key role of the dielectric material is to avoid the arc formation, limiting the discharge duration. DBDs are generally powered with AC supply, with frequencies up to several kHz in both continuous and pulsed mode. These devices can be fed with air, nitrogen and noble gases (Ar or He) and the flow rates are as high as several liters-per-minute (slm). Although initially characterized only by a discharge regime, nowadays many different regimes can be obtained by controlling the key parameters, like the excitation frequency and the applied voltage.

Microplasma are a third category of cell design in which the electrode distance is sub-millimetric and the discharge is confined in this tiny space [56]. Microplasmas can achieve very stable non-equilibrium conditions at atmospheric pressure. Its main application is in the synthesis of free-standing nanomaterials.

2.1.2 High-frequency plasma generation

Uniform, stable and spark-free atmospheric pressure plasmas can be obtained by applying high-frequency alternated-current electric fields in the MHz to GHz range. In the 90's, a first prototype with 13.56 MHz operating frequency was developed in the US and deeply investigated [64, 75].

Two stable operating mode are possible: the α-mode and the γ-mode. Stable uniform discharge through bulk ionization is obtained in α-mode, with negligible contribution of the secondary electrodes emitted by the cathode. Conversely, the γ-mode exploits secondary electron emission, with a small electrode area coverage [64]. In the stable α-mode, temperature lower than 200 °C have been reported.

For the class of high-frequency plasma generation, three main electrode geometries can be highlighted, as reported in Figure 2.3 [76–78].

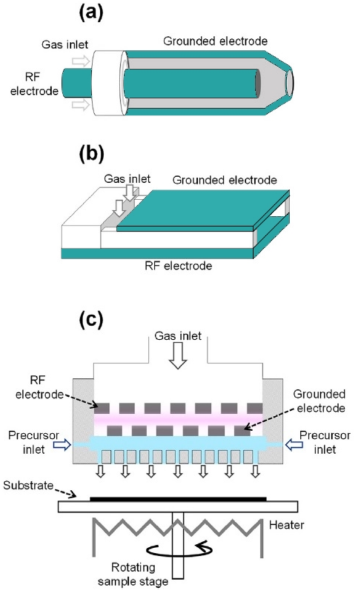

FIGURE 2.3: Typical RF atmospheric pressure electrode geometries: (a) concentric electrodes, (b) parallel plate electrodes and (c) perforated parallel plate electrodes [53].

The first configuration is characterized by concentric electrodes made of stainless steel. The RF signal is applied to the inner electrode and a cooling system is required to maintain temperatures around 100-150 °C. The parallel plate and perforated parallel plate electrode geometries are very similar, and in both cases the gas flows in the channel between the electrode and the counter-electrode. Generally, the lower electrode is grounded and the RF signal is applied to the top electrode. Since in the last case the outlet is composed of many holes, it is commonly referred as to the "showerhead plasma".

Another strategy rather than the RF signal application is the generation and stabilization of atmospheric plasma through microwaves. To date only few studies have been proposed, mainly for surface processing with Ar as feeding gas.

2.1.3 A comparison between traditional low-pressure plasma and atmospheric plasma

In the last decades, many industrial processes have exploited the usefulness of plasma treatments over a wide range of application areas including optics, packaging, microelectronics and bio materials. The development of atmospheric pressure plasma devices over conventional ones have attracted scientists in recent years. The absence of vacuum systems as well as the reduced reactor cost, easier handling and the overcome of geometric constraints are the basic motivations of the rapid growth over traditional plasmas. However, many critical aspects have to be taken into account since the creation of a stable plasma in atmospheric conditions is challenging. In fact, a wide range of instabilities can cause plasma arcing or overheating and inhomogeneities in the plasma plume can result for filamentation of the plasma itself [64, 65]. To overcome these problems, a careful selection of the feeding gas mixture can help to maintain the non-equilibrium condition, avoiding overheating and arcing.

Noble gases like argon (Ar) and Helium (He) are generally used as primary gases, since they are noble gases and can operate at significantly lower voltages [56, 63, 65, 68]. This translates in lower power density and lower thermal instability.

Air or nitrogen are generally avoided, because of their higher breakdown voltage and lower thermal capacity. Nevertheless, the use of noble gases over air or nitrogen raises the running costs, since the feeding flow can be as high as several liters-per-minute, especially to reduce the residence time in the plasma state so to reduce the gas heating [63].

2.2 Plasma enhanced reactions and polymerization

Among the large variety of techniques available for the tailoring of surface properties, the family of plasma-based techniques is of particular interest

because it combines several advantages, such as low temperature processing, wide range of materials that can be treated and versatility to modulate the required properties just by simply adjusting the synthesis conditions.
Nowadays, the development of organic thin film surfaces is of great interest, as most of the applications are focused on surface capabilities and interactions. Plasma-based technologies allows for the synthesis of plasma polymer films (PFF) [79] that slightly resembles a conventionally polymerized film. In fact, a plasma polymerization creates a random network rather than conventional repeating-block chains, resulting in a higher cross-linking degree.
The concept is well schematized in Figure 2.4.

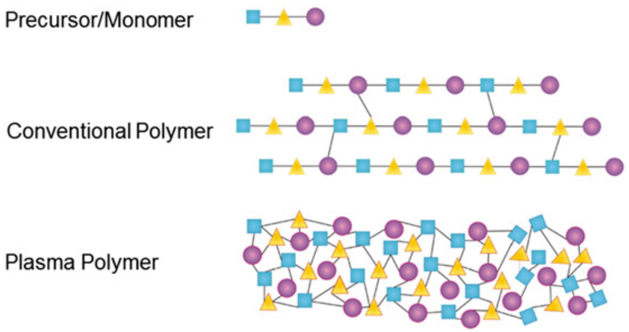

FIGURE 2.4: Comparison of a traditionally processed polymer and a plasma polymerized one [79].

It has been demonstrated that PPF have good thermal, chemical and mechanical stability and a variety of materials, even with complex geometry, can be homogeneously covered.
Plasma polymerization have gathered great attention in the corrosion and packaging fields, that for historical reasons aimed to produce physical barriers with high cross-linking degree. The cross-linking degree is, in fact, related to the precursor fragmentation, that in the highly energetic environment created by a plasma can be easily achieved. However, a highly energetic condition is generally leading to a poor chemical composition

control, that is the key-parameter to define the performances of PPF.
In the large class of plasma-based technologies, atmospheric pressure plasmas are predominantly used because of their non-equilibrium feature, that allows the electrons to induce chemical reactions without an important thermal contribution. However, due to the recent development of atmospheric plasmas over conventional low-pressure plasmas, the plasma polymerization process have been widely studied for conventional plasmas [79] and only recently have been extended to atmospheric ones [80].
The precursors used for low-pressure plasmas are generally identical to that of atmospheric ones, but at atmospheric pressure the monomer injected in the plasma through the use of a plasma gas. This gas carrier allows the monomer to reach the plasma region, where the polymerization in mainly induced by the formation of a radical specie obtained by collision with a high-energy particle or by UV excitation. This represents the main difference with respect to a low-pressure plasma where the activation is obtained by monomer-electron collision.
Another key feature of atmospheric pressure plasma is represented by the possibility to synthesize oxides starting from liquid or vapor precursors. In fact, a proper selection of the gas carrier, for example an Ar/O_2 mixture, can lead to the formation of a strongly oxidizing atmosphere thanks to the enhanced radical formation in plasma. If this atmosphere is combined with a buffer solution of organo-metallic precursor, the result is the combustion of the organic part and the oxidation of the metal. As a practical example, a buffer solution of zinc acetate fluxed in Ar/O_2 carrier, results in the formation of zinc oxide with complete disappearing of the organic acetate group.

2.2.1 Plasma polymerization

One of the most commonly accepted plasma polymerization model is the *Yasuda* "Rapid Step Growth Polymerization" (RSGP) model [81], initially developed for low-pressure plasmas but in good agreement with experimental results also for atmospheric pressure plasmas. This model is based on the assumption of total monomer fragmentation induced by the plasma and subsequent recombination and deposition (Figure).

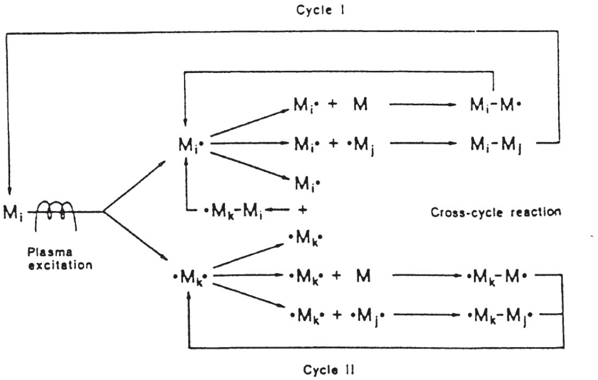

FIGURE 2.5: Plasma polymerization growth mechanism [82].
M: initial monomer
i,j,k: polymerization steps

Since the bulk structure of plasma polymers is completely irregular, the proposed mechanism is considered the most likely to occur. However, many internal and external plasma parameters, such as reactor geometry, applied voltage or monomer partial pressure, can influence the properties of the films.

Moreover, a significant difference between conventional and plasma polymers should be highlighted. The fragmentation of precursor monomer occurring in the plasma state leads to the formation of fragments that are generally smaller than the original monomer. The structure of plasma polymers cannot be accurately predicted from the structure of the monomer as the feeding precursor can be considered mostly as a source of single atoms, for an atomic level polymerization.

The plasma polymerization is not able to provide linear polymers but instead creates complex three-dimensional networks with high-degree of cross-linking. Carbon atoms are almost always branched or cross-linked in a network that resembles a diamond-like structure.

The interaction between organic molecules and plasma can occur through direct ionization of the molecules or by collision with gas excited species. Since the gas feels the presence of precursor molecules, it can dissipate its own energy either via photon emission or via collisional transfer. The photon emission is generally reduced upon the addition of an organic molecule because a portion of energy is used for the organic molecule excitation. This is realized by breaking covalent bonds (like C-C and C-H) because it requires less energy than the ionization of the molecule.

Another important concept is related to the plasma-surface interaction. Since the energy of electrons and ions is relatively low, even in presence of a polymeric surface, the direct interaction can be considered as to be limited to the surface without penetration. Conversely, the UV photons generated by plasma ion dissipation are extremely more energetic and can penetrate into the bulk of the material.

If on one hand the plasma physical penetration is negligible, the chemically active species produced by plasma ionization and energy transfer cannot be considered limited to the surface. In fact, the penetration strongly depends on the chemical reactivity and specificity of the surface. Two parameters are responsible for this effect: the transport rate and the chemical reaction rate.

2.2.2 Chemistry of the feeding monomer

The chemical structure of the organic compounds used as monomers is generally of fundamental importance in conventional polymerization. For example, the presence of double and triple bonds is mandatory for a vinyl polymerization. However, when considering the process of plasma polymerization, this chemical importance is lost, and the monomers can be classified in four different classes:

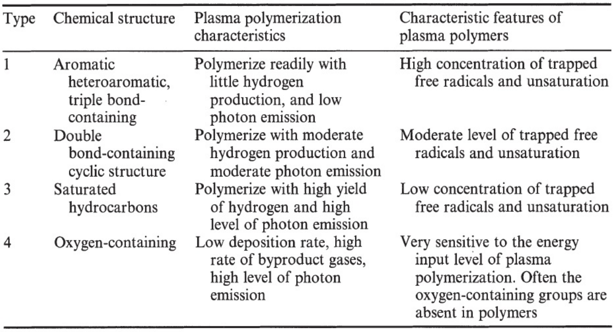

Type	Chemical structure	Plasma polymerization characteristics	Characteristic features of plasma polymers
1	Aromatic heteroaromatic, triple bond-containing	Polymerize readily with little hydrogen production, and low photon emission	High concentration of trapped free radicals and unsaturation
2	Double bond-containing cyclic structure	Polymerize with moderate hydrogen production and moderate photon emission	Moderate level of trapped free radicals and unsaturation
3	Saturated hydrocarbons	Polymerize with high yield of hydrogen and high level of photon emission	Low concentration of trapped free radicals and unsaturation
4	Oxygen-containing	Low deposition rate, high rate of byproduct gases, high level of photon emission	Very sensitive to the energy input level of plasma polymerization. Often the oxygen-containing groups are absent in polymers

TABLE 2.1: Classification of the organic compound for plasma polymerization [82].

Table 2.1 groups the main experimentally observed characteristics with the chemical structure of precursor monomers.

It is possible to notice that the reactivity level changes significantly with the initial chemical structure. In particular, oxygen-containing precursors are very sensitive to the energy level and they can react and being released without contributing to the final polymerized structure.

A list of the most common and widely studied monomers for plasma polymerization is reported in Table 2.2.

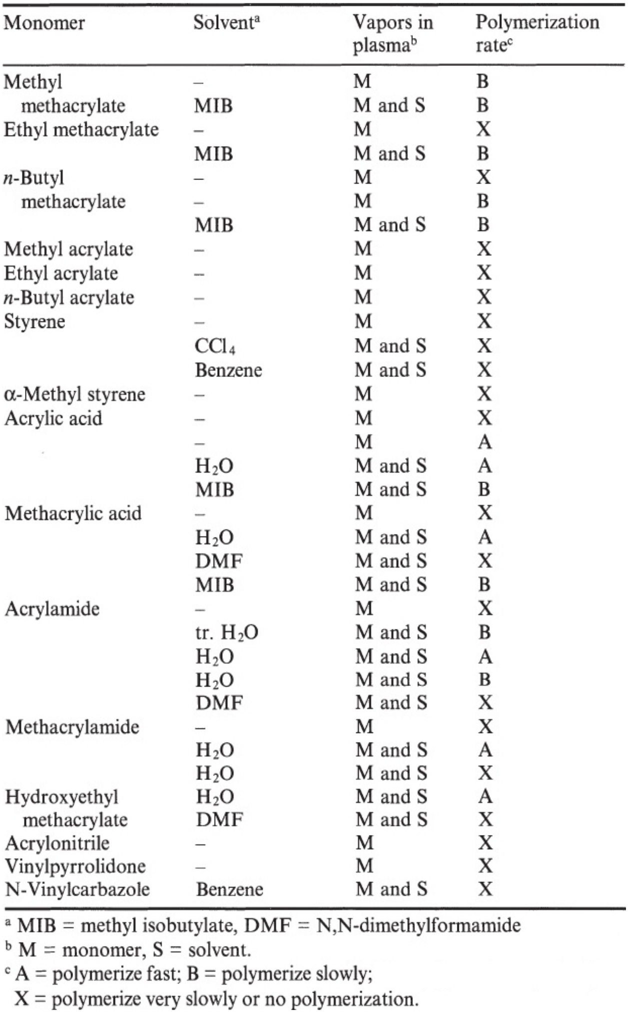

Monomer	Solvent[a]	Vapors in plasma[b]	Polymerization rate[c]
Methyl methacrylate	–	M	B
	MIB	M and S	B
Ethyl methacrylate	–	M	X
	MIB	M and S	B
n-Butyl methacrylate	–	M	X
	–	M	B
	MIB	M and S	B
Methyl acrylate	–	M	X
Ethyl acrylate	–	M	X
n-Butyl acrylate	–	M	X
Styrene	–	M	X
	CCl_4	M and S	X
	Benzene	M and S	X
α-Methyl styrene	–	M	X
Acrylic acid	–	M	X
	–	M	A
	H_2O	M and S	A
	MIB	M and S	B
Methacrylic acid	–	M	X
	H_2O	M and S	A
	DMF	M and S	X
	MIB	M and S	B
Acrylamide	–	M	X
	tr. H_2O	M and S	B
	H_2O	M and S	A
	H_2O	M and S	B
	DMF	M and S	X
Methacrylamide	–	M	X
	H_2O	M and S	A
	H_2O	M and S	X
Hydroxyethyl methacrylate	H_2O	M and S	A
	DMF	M and S	X
Acrylonitrile	–	M	X
Vinylpyrrolidone	–	M	X
N-Vinylcarbazole	Benzene	M and S	X

[a] MIB = methyl isobutylate, DMF = N,N-dimethylformamide

[b] M = monomer, S = solvent.

[c] A = polymerize fast; B = polymerize slowly; X = polymerize very slowly or no polymerization.

TABLE 2.2: Common plasma monomers with polymerization conditions [82].

More recent research highlighted that a variety of substances can be feed as monomers for plasma polymerization, some of them more *green chemistry* oriented [83].

2.2.3 Nanomaterials synthesis through APPJ technology

The peculiar geometry of APPJ and the intrinsic low-temperature characteristic makes APPJ plasmas ideal for the synthesis of standalone nanomaterials and thin films starting from liquid aerosol solutions or vapors. Moreover, the possibility to use specific carrier gases and custom buffer solution allows to obtain controlled reactions in the plasma phase and a good final material stoichiometry control [53, 68, 84, 85]. Although widely used for etching and surface activation treatments, APPJ was intensively studied for the deposition of semiconductor materials, SiO_x coatings and carbon nanostructures [84].

Oxides represents a main category in APPJ deposition and were extensively studied. A variety of different oxides have been deposited so far: SiO_x, SiO_2, CeO_x, TiO_2, SnO_x, InO_x, ZnO and ZnO:Al [63]. Silica-based oxides were grown starting from silane gas or more conventional tetramethyldisiloxane (TMDSO), hexamethyldisiloxane (HMDSO), and tetraethylorthosilicate (TEOS) precursors. Alternatively, trimethylsilyl chloride was also tested to produce stoichiometric SiO_2 thin films [86]. Semiconductor TiO_2 and CeO_x thin films were obtained from titanium oxide acetylacetonate and cerium acetate, respectively [87, 88]. Moreover, conductive transparent oxides, such as ZnO:Al, SnO_x and InO_x, with low electrical resistivity and good transparency were obtained [89–91].

A key-feature of APPJ plasmas resided in the possibility to obtain doped materials at low temperature thanks to a fine tuning of precursor liquid solution [85]. On one hand, thin films are obtained by direct interaction of the plasma plume with the substrate, giving a uniform coating both in thickness and coverage. On the other hand, plasma-liquid interactions have been investigated for the production of standalone nanoparticles [84, 92–94].

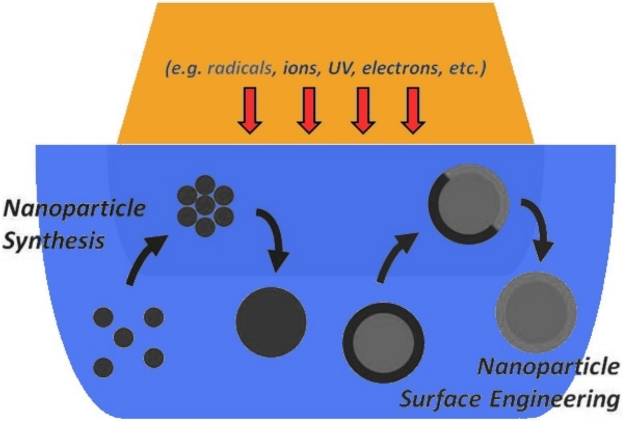

FIGURE 2.6: Plasma-liquid interaction for the deposition of nanoparticles [92].

Standalone nanoparticles can be produced with different size and shapes by direct plasma-liquid choosing the proper precursor solution and concentration. For example, gold nanoparticles in liquid solution were produced from chloroauric acid solution in water without stabilizing agents [92]. Tunable compact layers made by aggregation of standalone gold nanoparticles were also deposited for plasmonic applications [95].
Another advantage offered by APPJ resides in the possibility to engineer the surface of standalone nanoparticles through specific surface engineering. For example, *Mariotti et al.* reported on the surface engineering of silicon nanoparticles in ethanol through plasma-liquid interaction for enhanced photovoltaic applications [92]. Alternatively, plasma polymerization of diverse monomers can lead to specific nanoparticle surface fictionalization, for example through passivation of surface defect with consequent PL enhancement [96].

Chapter 3

Materials and Methods

In this chapter, all the experimental details about the plasma torch and the characterization techniques are reported. Firstly, the plasma machine is presented and the standard working parameters are reported. Secondly, all the customization and the movement control program is presented. Thirdly, an overview of the polysiloxane resins shows the preparation and reaction for the matrix used to produce the samples. Finally, the techniques used to characterize all the produced samples are introduced and the standard parameters are reported.

3.1 The custom plasma setup

The custom setup used to realize the samples reported lately is based on a commercial atmospheric pressure plasma torch (Stylus Plasma Noble, Nadir S.r.l., US patent n° US9693441B2, EU patent n° EP3069577A1 [97, 98], modified for our purposes.). The torch operates in atmospheric pressure conditions using a noble gas (Argon) thanks to a specific electrode geometry (dielectric barrier discharge, DBD) in which the electrodes are not directly in contact but they are coated with an alumina layer. A schematic cross-section of the plasma head is shown in Figure 3.1

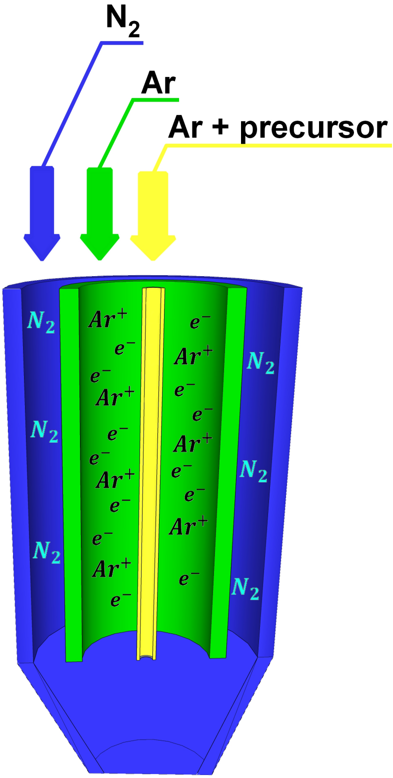

FIGURE 3.1: Plasma torch head cross-section highlighting the concentric channel structure with cooling, plasma and reacting species.

A concentric-channel geometry allows to generate the plasma in a specific region (high voltage region) and to drive the plasma out of a nozzle for some millimeters, using a radiofrequency circuit (RF region). The plasma head was mounted on a customized 3D printer framework (Velleman K8200). The printer framework was modified by replacing the printing head with the plasma torch, and the heating bed with a more powerful one (mica-based, 100 W, up to 300 °C).

The torch was operated with user-tuned parameters that are listed in the section below.

3.1.1 APPJ standard parameters

In this section, the plasma torch operating parameters for deposition are reported (Table 3.1). All these parameters were kept constant for all the depositions reported in this thesis, if not differently specified.
Table 3.1 summarizes the main plasma parameters, such as the high voltage, the RF power and the gas flows.

RF Power [W]	**Distance** [mm]	**High voltage** [kV]
20	6	7÷8

Argon process gas [slm]	**Nitrogen cooling gas** [slm]	**Precursor gas** [slm]
5	14÷15	0.4

X-Y stage movement [mm/min]
300

TABLE 3.1: Plasma standard parameters for deposition/treatment.

The 3D stage is provided of a microcontroller (ATmega2560) that receives instruction via usb connection and drives the x-y-z motors. The 3D stage, derived by a modified 3D printer, comes along with a commercial open-access software that was not able to satisfy the requirements for controlled thin films and nanoparticles deposition, so a MatLab-based GUI (Graphical User Interface) was developed and implemented. The program communicates with the microcontroller through G-Code language.
The program allows for custom controlled movements of the plasma torch head and for two different patterned movements (linear or square-grid).
The custom system GUI layout is reported in Figure 3.2.

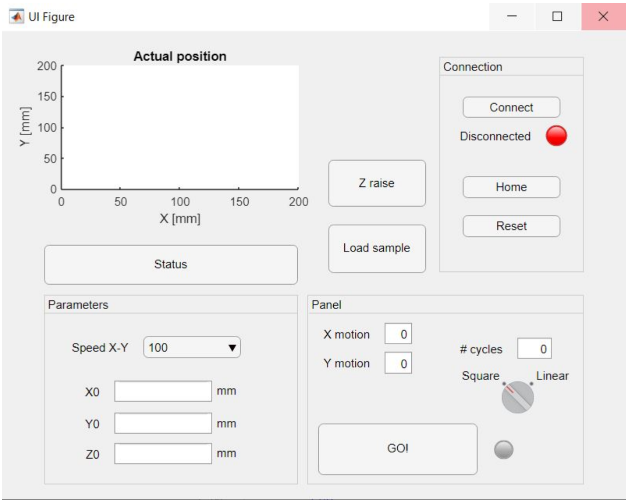

Speed X-Y 100

X motion 0

Y motion 0

cycles 0

FIGURE 3.2: Plasma movement system GUI.

The motion system is based on NEMA motors that are not provided of optical encoders for motion control, so an initial calibration is required.
The patterned square-grid movement was used to deposit all the samples, resulting in a good deposition homogeneity. Large areas can be covered with homogenous thickness in multiple steps, resulting in reproducible samples.
The x-y plane is provided of a custom heating plate that is operated through an external controller, allowing for a temperature range from room temperature up to 300 °C thanks to a mica-based heater.

3.2 Polysiloxane synthesis

For the preparation of polysiloxane-based samples, three different types of resin were employed: PDMS, PSS1418 and PSS100, where for PSS samples the number represents the percentage amount of vinyl content in each resin.

The two resins follows different cross-linking paths, because one can polymerized through poly-addition while the other by poly-condensation. This is an important information because the reaction behavior influences the geometry of the final sample, as the shrinkage is not equal.
Both polymerization reactions can occur at room temperature in 24/48 hours but are favoured at slightly higher temperature, such as 60 °C for 4 hours.
In both cases, the presence of a platinum or tin catalyser is fundamental to trigger the reaction.

3.2.1 PDMS

Poly-dimethyl-siloxane (PDMS) was employed for its superior transparency and flexibility.
The chemical structure is reported in Figure 3.3.

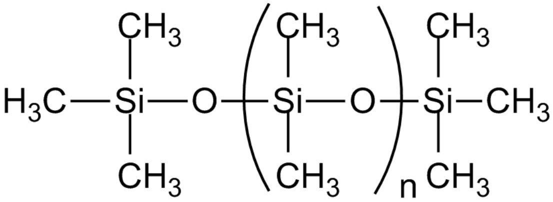

$$\mathrm{H_3C}-\underset{\mathrm{CH_3}}{\overset{\mathrm{CH_3}}{\mathrm{Si}}}-\mathrm{O}\left(\underset{\mathrm{CH_3}}{\overset{\mathrm{CH_3}}{\mathrm{Si}}}-\mathrm{O}\right)_n\underset{\mathrm{CH_3}}{\overset{\mathrm{CH_3}}{\mathrm{Si}}}-\mathrm{CH_3}$$

FIGURE 3.3: Molecular structure of poly-dimethyl-siloxane.

The easiness of production and handling makes the PDMS resin suitable for a variety of applications. However, the absence of phenyl groups makes the resin insensitive to the radiation, making it suitable only for being a host matrix for an active material. On the other hand, the superior transparency grants that the scintillation light is collected efficiently, with minor losses.

3.2.2 PSS 14-18

Poly(dimethyl-co-diphenyl) siloxane (PSS1418) with phenyl content of 14 ÷ 18 % mol. was employed for its lower rigidity compared to PSS-22 and PSS-100. Nevertheless, the phenyl content hinders the polymer chain mobility and reduces the elongation at break. On the other hand, the presence of phenyl groups is essential for the scintillation behavior, since the benzene-like structure allows for visible electron transitions.
The realization of PSS14-18 samples is obtained by mixing three components: the *Diphenylsiloxane-Dimethylsiloxane* copolymer, the *MethylHydrosiloxane - PhenylMethylsiloxane* and the *dioctyltindilaurate* as catalyser.
The molecular structure of the base resin, the *Diphenylsiloxane-Dimethylsiloxane copolymer, vinyl terminated*, is shown in Figure 3.4

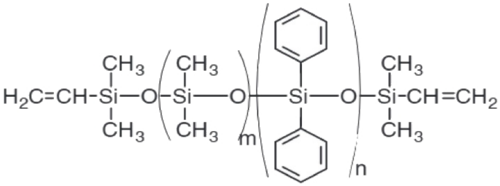

FIGURE 3.4: Molecular structure of *Diphenylsiloxane-Dimethylsiloxane copolymer, vinyl terminated* (n ≈ 14÷18).

The component reacts with *MethylHydrosiloxane - PhenylMethylsiloxane, hydride terminated* shown in Figure 3.5, to obtain a linear structure.

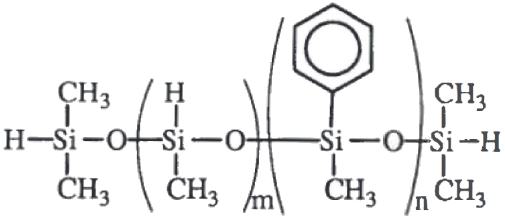

FIGURE 3.5: Molecular structure of *MethylHydrosiloxane - Phenyl-Methylsiloxane, hydride terminated* (n ≈ 45÷50).

The reaction is favoured by the use of a catalyser, *dioctyltindilaurate* (Figure 3.6).

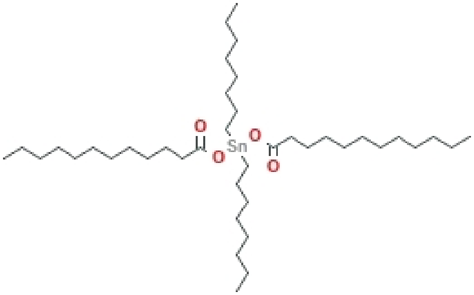

FIGURE 3.6: Molecular structure of *dioctyltindilaurate*.

3.2.3 PSS-22 and PSS-100

Another siloxane-based polymer used for the realization of flexible scintillator is the poly(dimethyl-co-diphenyl) siloxane with phenyl content of 22% mol. or of 99÷100% mol. It is employed to increase the scintillation performances compared to the PSS14-18 samples. However, the increase of phenyl content helps increasing the scintillation performances but reflects on the mechanical properties of the final polymer, with an increase of rigidity and a decrease of flexibility.

The realization of PSS-22 and PSS-100 samples is obtained by mixing three components: the *Vinyl Terminated poly-Phenyl-Methylsiloxane*, the *Methyl-Hydrosiloxane - Phenyl-Methylsiloxane* and the *Platinum - divinyl-tetramethyl-disiloxane complex in xylene* as catalyser.

The molecular structure of the base resin, the *Vinyl Terminated poly-Phenyl-Methyl-siloxane*, is shown in Figure 3.7

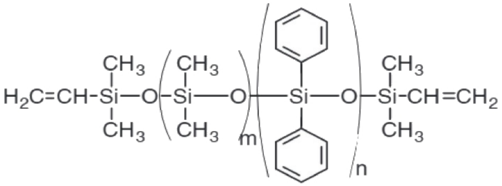

FIGURE 3.7: Molecular structure of *Vinyl Terminated polyPhenyl-Methyl-siloxane* (n $\approx$ 99 $\div$ 100).

The component reacts with *Methyl-Hydrosiloxane - Phenyl-Methylsiloxane, hydride terminated* shown in Figure 3.8, to obtain a linear structure.

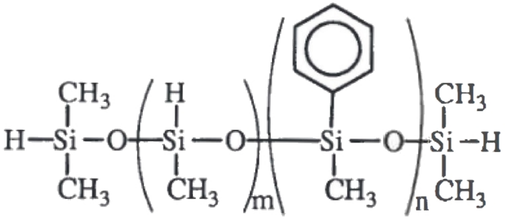

FIGURE 3.8: Molecular structure of *Methyl-Hydrosiloxane - Phenyl-Methylsiloxane, hydride terminated* (n $\approx$ 45 $\div$ 50).

The reaction is favoured by the use of a catalyser, *Platinum - divinyl-tetramethyl-disiloxane complex in xylene* (Figure 3.9).

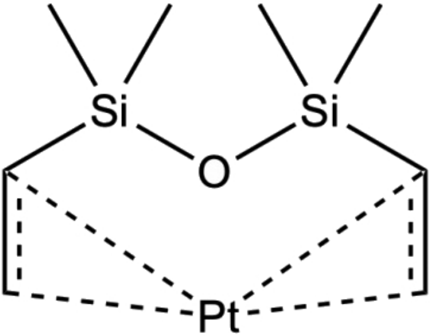

FIGURE 3.9: Molecular structure of *Platinum - divinyltetramethyldisiloxane complex in xylene*.

3.3 Optical measurements

3.3.1 UV-Vis and steady-state measurements

Luminescence measurements is taken either using an UV-Vis spectrofluorometer or with a laser as excitation source.

FIGURE 3.10: Jasco FP-6300 spectrofluorometer.

The UV-Vis spectrofluorometer (Jasco FP6300, Figure 3.10) is a single xenon lamp excitation source that covers the 200÷750 nm range. It has two monochromators, one for selecting the excitation wavelength and one for the emission wavelength, and two PMT detectors that can be biased up to 1000 V. The typical settings for an excitation-emission measurement includes an excitation and emission slit width of 5 nm, a measurement speed of 500÷1000 nm/min and a sensitivity (i.e. PMT voltage) of 400 V.
A general scheme of a spectrofluorometer is shown in Figure 3.11.

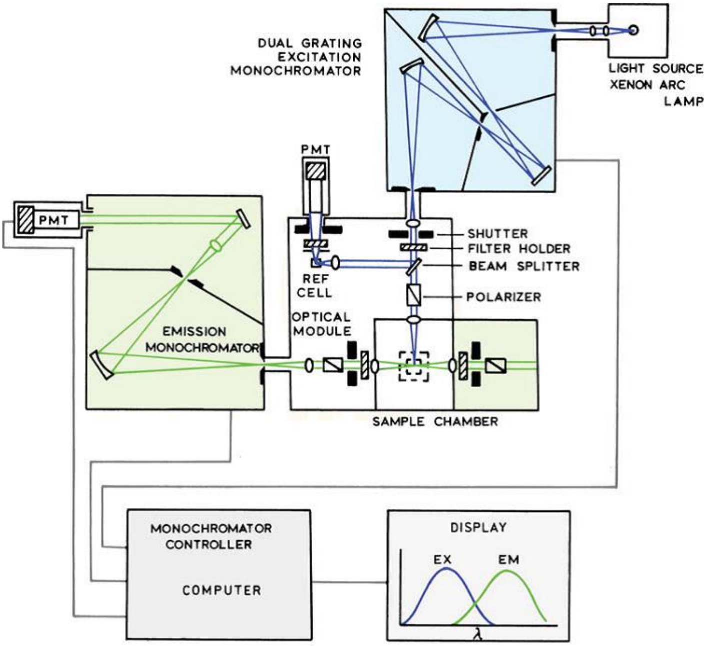

FIGURE 3.11: General scheme of a spectrofluorometer.

For laser measurements, two different wavelengths are employed: a 266 nm and a 355 nm. Both are diode-pumped solid-state (DPSS) lasers based on 3^{rd} (355 nm) and 4^{th} (266 nm) harmonic (Figure 3.12). The lasers are frequency modulated (5÷10 kHz) with pulse width of 3÷7 ns for the 355 nm and 250÷350 ps for the 266 nm. The excitation source (355 nm) is conveyed into a single-mode optical fiber (125 μm) or shot directly on the sample (266 nm).

The fluorescence is collected using a dry microscope objective (Olympus RMS4X achromatic, 0.10 NA) and, if necessary, an optical cut-off filter to eliminate the laser-line (364 nm cut-off for the 355 nm source). The signal is conveyed into an optical fiber (600 μm core) to a portable spectrometer (OceanOptics QE65000, 200÷1000 nm range, 1 nm sensitivity). The spectrometer is connected to a laptop where the dark spectrum correction is asses by software subtraction (SpectraSuite).

3.3.2 Time-resolved measurements

Time resolved measurements are carried out using a time-correlated single photon counter (TCSPC, PicoHarp 300) with 4 ps timing resolution coupled with the optical system described in the previous section.

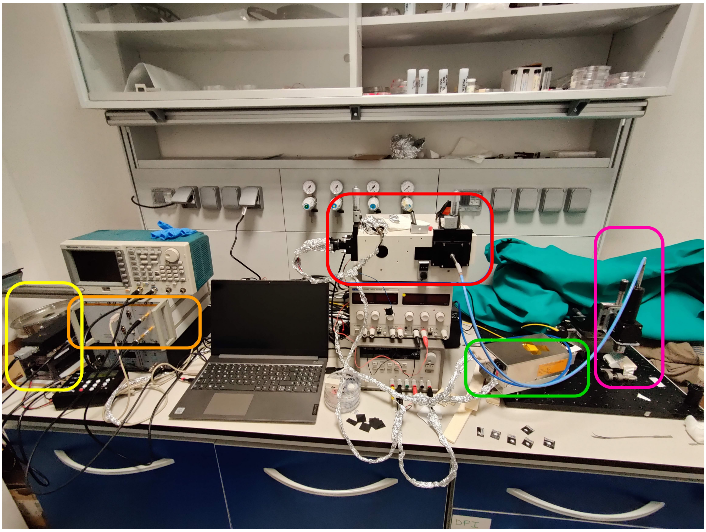

FIGURE 3.12: Laser bench with laser heads (green 266 nm, yellow 355 nm), collection system (pink), monochromator (red) and TCSPC (orange).

The TCSPC allows to create the histogram of photon arrival by acquiring the time difference between the emission of a bunch of photons by the laser and the fluorescence of the sample collected through the PMT/APD. The general TCSPC working principle is shown is Figure 3.13.

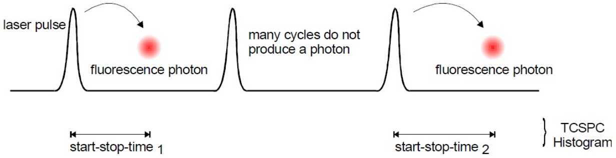

FIGURE 3.13: Time-correlated single photon counting principle [99].

The trigger signal is synchronized using an external pulse generator (Tektronix AFG3000C) or by using the laser driver, depending on the polarity of the synch signal. For every photon emitted upon laser excitation, an electrical signal (i.e. pulse) is generated by the PMT and collected by the TCSPC to build the time histogram. An example of a correlation histogram is shown in Figure 3.14

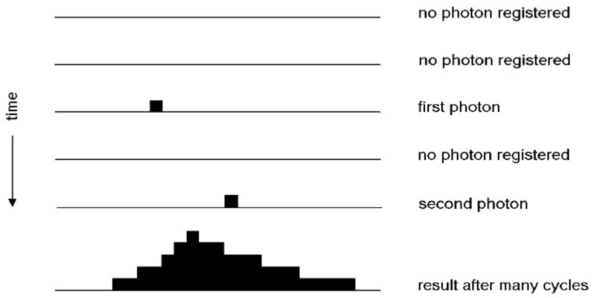

FIGURE 3.14: Photon arrival and time correlation [99].

Since the fluorescence decay is typically following an exponential behavior, the fit of the histogram gives the lifetime value.
The general working principle of the TCSPC system coupled with the laser source and the laptop is shown in Figure

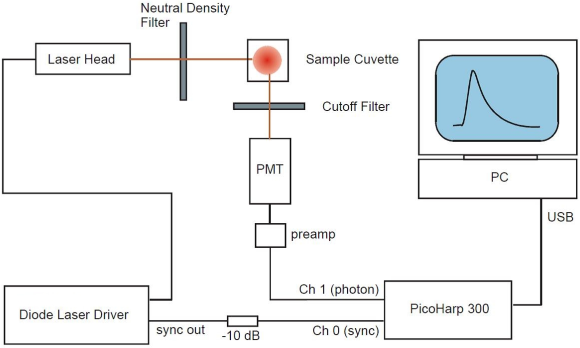

FIGURE 3.15: Schematic of the TCSPC coupled with the PMT and laser source for timing measurements [99].

3.4 FT-IR measurements

The Fourier-transformed Infrared Spectroscopy (FT-IR) is performed using a Nicolet Avatar 330 (Figure 3.16) equipped with DTGS detector. The measurements are performed in transmittance mode using 8 cm^{-1} resolution, 64 scans and bare silicon as reference. All the other machine parameters are kept constant and set to default values.

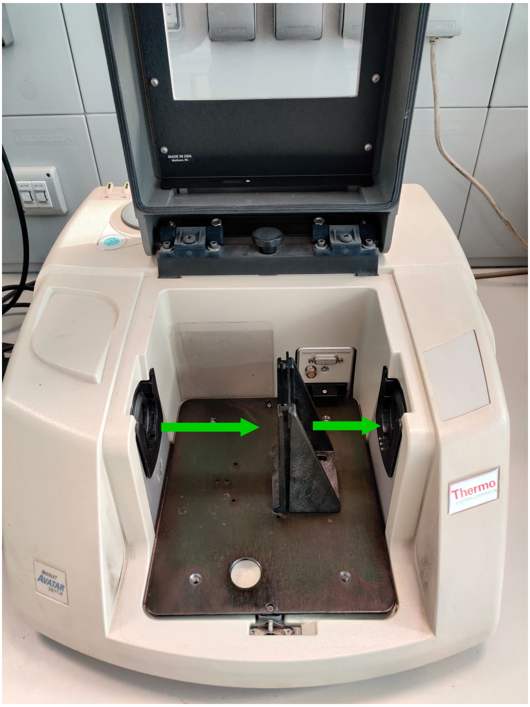

FIGURE 3.16: Nicolet Avatar 330 FT-IR.

3.5 SEM/EDS measurements

The scanning electron microscopy characterization is performed using a Zeiss Supra 50 SEM equipped with backscattered (AsB) detector and field emission gun (FEG) source. Standard parameters for morphology analysis are: 5 kV acceleration, 30 μm aperture and 20 s integration time for a single acquisition.
The energy dispersive spectroscopy (EDS) is performed using a Jeol JSM-IT300LV SEM equipped with a FEG source and a BRUKER QUANTAX XFlash 630M detector with liquid-nitrogen cooling. The samples are inspected at 10 kV with 60 s integration time.

3.6 Electrical measurements

The electrical measurements area collected using a four-point probe station (Everbeing C6) equipped with a Keithley 4200A-SCS parameter analyzer. The instrument results are provided as sheet resistance ($\Omega/\Box$) and subsequently converted to resistivity ($\Omega \cdot cm$) using the known sample thickness acquired with a mechanical profilometer.

3.7 X-ray diffraction (XRD)

X-ray diffraction measurements are carried out using a Italstructures IPD3000 (Figure 3.17) instrument in vertical Bragg-Brentano configuration. The instrument is equipped with a wide-angle detector that allows for a full-spectrum record. For pure XRD measurements the analysis is performed in low incident angle mode ($\approx 1°$) with a cobalt source ($K_\alpha = 1.7902$ Å) powered at 40 kV / 20 mA.

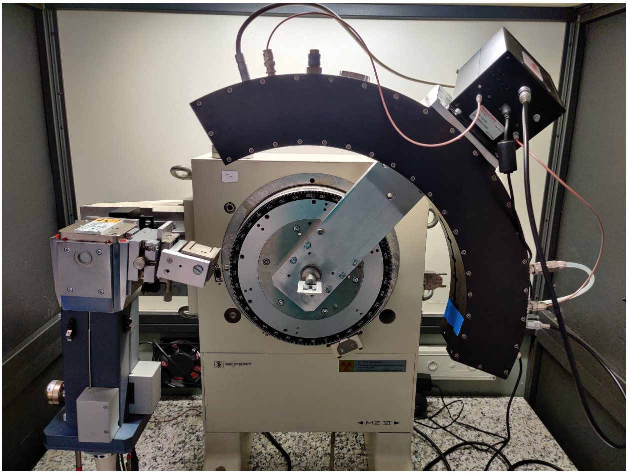

FIGURE 3.17: IPD3000 instrument with wide angle detector.

For X-ray luminescence (XRL) measurements the source is powered with the same configuration but the detector was replaced with an optical fiber (multimode 600 μm core) connected with the OceanOptics QE65000 spectrometer. The acquisition is performed using a custom software developed in MatLab ®, able to perform dark spectrum subtraction, continuous and single acquisition with or without dark spectrum correction.
The graphical user interface (GUI) of the program is visible in Figure 3.18.

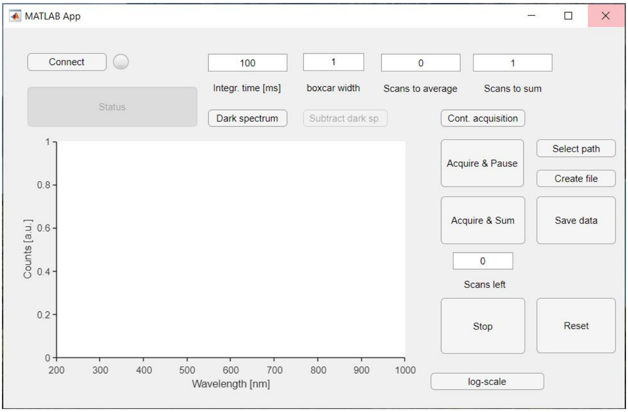

100
Integr. time [ms]

1
boxcar width

0
Scans to average

1
Scans to sum

0
Scans left

FIGURE 3.18: OceanOptics spectrometer acquisition GUI.

3.8 Thermogravimetric analysis (TGA)

The thermogravimetric analysis is performed using a Q5000 IR thermobalance (TA Instruments, Figure 3.19) with platinum crucibles (100 μL). The specimens are tested in the range 30-700 °C with 10 °C/min temperature ramp and under 10 sccm of N_2/air flow.

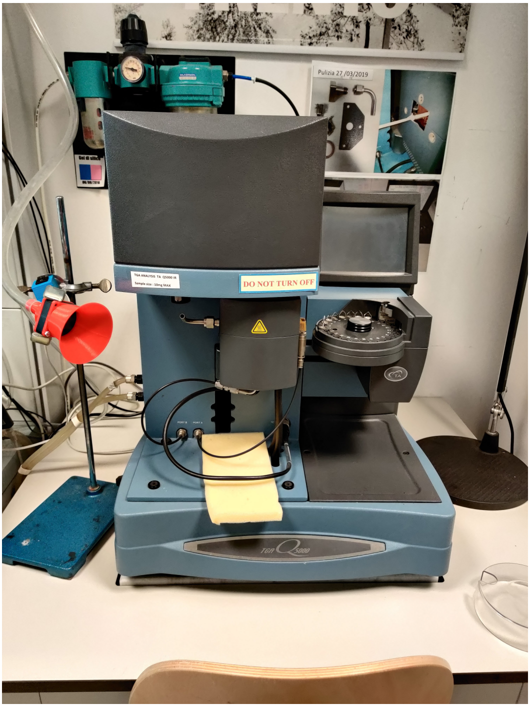

FIGURE 3.19: Q5000 IR thermobalance.

3.9 Differential scanning calorimetry (DSC)

The differential scanning calorimetry (DSC) is performed using a Mettler DSC30 instrument (Figure 3.20). The sample is heated from 30 °C to 180 °C at 20 °C/min, kept at 180 °C for 40 minutes, cooled to -50 °C at 10 °C/min and, finally, heated at 10 °C/min up to 200 °C. The entire procedure is done under a N_2 flow of 100 sccm.

FIGURE 3.20: Mettler DSC 30.

3.10 Nuclear magnetic resonance (NMR)

The NMR analysis is carried out using a Bruker 400WB (Figure 3.21) spectrometer operating at a proton frequency of 400.13 MHz in solid state conditions at the magic angle spinning (MAS).

FIGURE 3.21: Bruker 400 WB NMR.

The NMR spectrum is acquired with cross polarization (CP) pulse sequence under the following conditions reported in Table 3.2.

^{13}C frequency [MHz]	Contact time [ms]	Decoupling length [μs]	Recycle delay [s]	# of scan
100.48	2	5.9	5	$2{\cdot}10^5$

TABLE 3.2: ^{13}C CP-MAS NMR parameters.

A 4 mm zirconia rotor is used as sample holder and spun at 11 kHz under air flow. Adamantane is used as external secondary reference.

3.11 Electron spin resonance (ESR)

Electron spin resonance spectra are acquired with a Bruker EMX-6/1 (Figure 3.22) at 293 K, equipped with a X-band microwave generator (9.1 ÷ 9.8 GHz) and a 200 mW Gunn source. The magnetic field is varied between 3000 G and 4000 G and the measurements are acquired with fixed gain ($5 \cdot 10^5$), modulation amplitude (8 G), resolution (2048 channels) and conversion time ($\approx$ 40 ms).

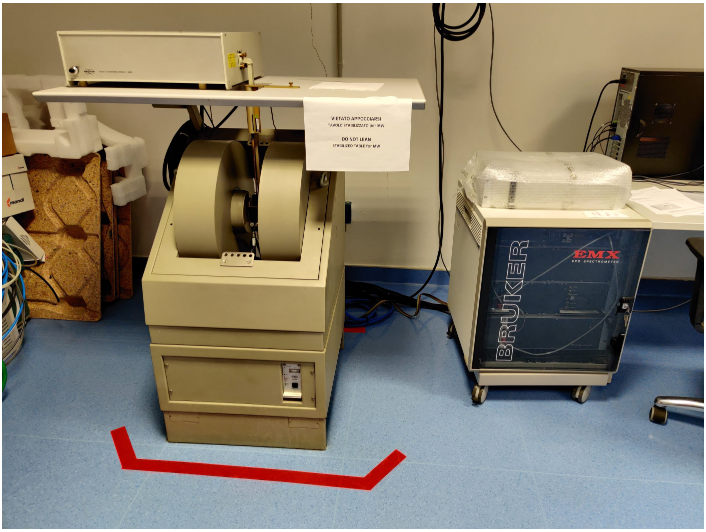

FIGURE 3.22: Bruker EMX-6 ESR

3.12 Scintillation measurements

Basic scintillation tests are performed using laboratory sources with limited activity of 1 μCi or 10μCi. An ^{241}Am source (E_α = 5.486 MeV) is employed for scintillation tests under alpha particle excitation, while a ^{133}Ba (E_C = 207.86 keV), a ^{137}Cs (E_C = 477.34 keV) and a ^{22}Na (E_C = 340.67 keV and 1061.71 keV) sources are used for the tests under gamma excitation.

The alpha and gamma-excitation measurement setup is composed of a conventional photomultiplier tube (Hamamatsu H10721-20), connected to a digitizer (Caen DT-5730), as visible in Figure 3.23.

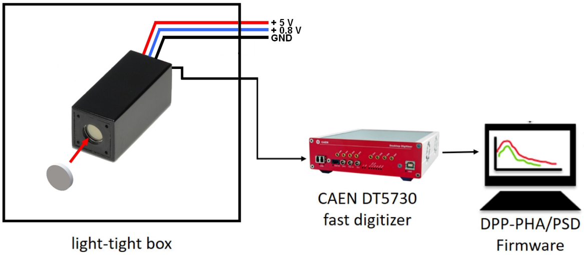

FIGURE 3.23: Scintillation acquisition setup for PDMS composite samples.

Each sample is coupled with the photocathode window of the PMT, without the need of optical grease, and the system is biased at 5 V with fixed gain at 0.8 V (corresponding to $\approx 2 \cdot 10^5$ V/V). The acquisition window is set to 1500 samples with resolution of 8 ns.

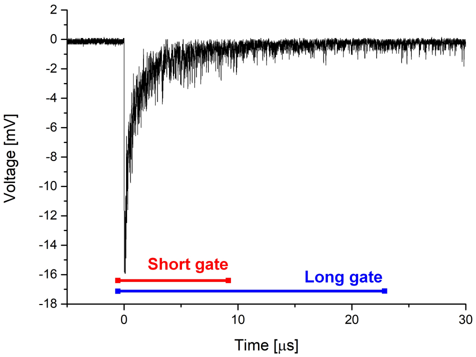

FIGURE 3.24: Short and long gate definition.

Figure 3.24 shows the definition of short and long integration gates, giving as a result the tail (short) and total (long) integral (or pulse integral).

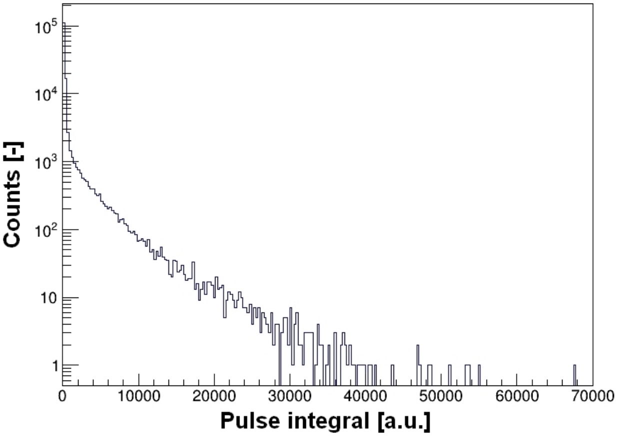

FIGURE 3.25: Example of alpha particle interaction with a ZnO:Zn loaded PDMS sample.

3.13 Ion-beam induced luminescence (IBIL)

Ion-beam induced measurements (IBIL) are acquired at the AN2000 Van de Graaf accelerator at the Legnaro national laboratories (INFN-LNL, Italy). A proton beam with 1.8 MeV energy and $\approx$ 1.5 nA current is shot on the front surface of the samples, while a silica optical fiber, connected to the portable spectrometer (OceanOptics QE65000) allows to record the real-time spectrum (Figure 3.26). The current beam of about 1.5 nA with a spot size of 2 x 2 mm^2 corresponds to $\approx 2 \cdot 10^{12} \frac{H^+}{cm^2 \cdot s}$.

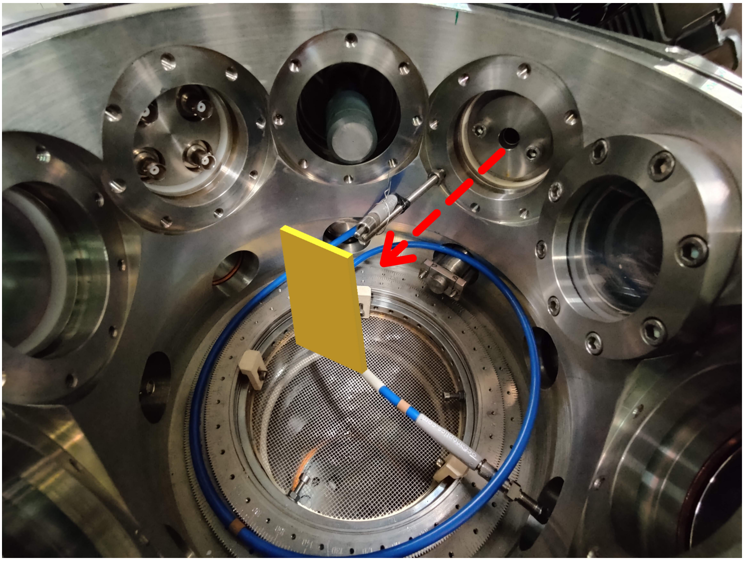

FIGURE 3.26: Scattering chamber of the 0° line of the AN-2000 accelerator with beam direction (red) and sample position (yellow).

The penetration depth of protons is PDMS was calculated using SRIM (The Stopping and Range of Ions in Matter) and resulted to be 72 ± 2 μm for 1.8 MeV energy, as visible in Figure 3.27 where the Bragg's peak is visible.

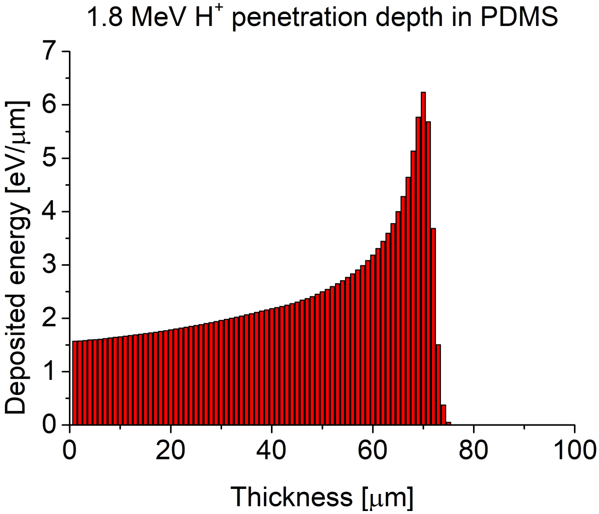

FIGURE 3.27: Penetration depth for 1.8 MeV protons in PDMS.

Chapter 4

Composite scintillators containing quantum dots

Part of this section has been published in:

ELSEVIER
Optical Materials
Volume 88, February 2019, Pages 271-276

"Photoluminescence enhancement of colloidal CdSe/ZnS quantum dots embedded in polyvinyl alcohol after 2 MeV proton irradiation: crucial role of the embedding medium"
E. Zanazzi, M. Favaro, A. Ficorella, L. Pancheri, G.F. Dalla Betta, A. Quaranta
Optical Materials, 88 (2019) 271-276

---

physica status solidi a
applications and materials science

"Real-Time Optical Response of Polysiloxane/Quantum Dot Nanocomposites under 2 MeV Proton Irradiation: Luminescence Enhancement of Polysiloxane Emission through Quantum Dot Sensitization"
E. Zanazzi, M. Favaro, A. Ficorella, L. Pancheri, G.F. Dalla Betta, A. Quaranta
Phys. Status Solidi A, 2020, 217, 1900586

THE JOURNAL OF PHYSICAL CHEMISTRY C
Article
Cite This: J. Phys. Chem. C 2018, 122, 22170−22177
pubs.acs.org/JPCC

"Proton Irradiation Effects on Colloidal InGaP/ZnS Core-Shell Quantum Dots Embedded in Polydimethylsiloxane: Discriminating Core from Shell Radiation-Induced Defects through Time-Resolved Photoluminescence Analysis"
E. Zanazzi, M. Favaro, A. Ficorella, L. Pancheri, G.F. Dalla Betta, A. Quaranta
J. Phys. Chem. C 2018, 122, 22170-22177

Nuclear Instruments and Methods in Physics Research Section B: Beam Interactions with Materials and Atoms
Volume 435, 15 November 2018, Pages 327-330

"Radiation-induced optical change of ion-irradiated CdSeS/ZnS core-shell quantum dots embedded in polyvinyl alcohol"
E. Zanazzi, M. Favaro, A. Ficorella, L. Pancheri, G.F. Dalla Betta, A. Quaranta
Nuclear Inst. and Methods in Physics Research B, 435 (2018) 327-330

In this chapter we report the study and characterization of polysiloxane-based flexible scintillators loaded with colloidal quantum dots (QD), in order to investigate the energy transfer mechanism between the matrix and the QDs. In particular, the luminescence emission has been investigated in real-time under proton beam and as steady-state and time-resolved photoluminescence before and after proton beam irradiation to evaluate the use of quantum dots embedded in polymeric matrices as acceptors.

4.1 Introduction

The use of colloidal quantum dots embedded in organic matrices has been partially investigated, with the aim of increasing the scintillation yield of polymeric-based composites under γ-rays. The use of high-Z components in low-Z polymeric matrices can enhance the γ-ray capture cross-section, leading to the creation of a more efficient composite scintillator [24]. In this work we studied the possibility of exploiting QDs as energy acceptors by producing a low-concentration composite scintillator in which the QDs should act as primary dye [100]. To obtain this result a low amount of nanocrystals is dispersed in a highly transparent phenyl-rich matrix that is employed for mechanical, optical and scintillation aspects. The working principle therefore should be based on a non-radiative energy transfer process of Förster type (FRET) between the matrix, acting as donor, and the nanocrystals acting as acceptor. A few works have suggested the possibility of FRET occurring between polymeric matrices and QDs [24, 101]. However, a controversial debate is still open on the role of QDs as acceptors, since the remarked difference in lifetime between donor (organic matrix) and acceptor, that cannot lead to an efficient energy transfer process [102]. It has been reported that their potential use as acceptors is more challenging than their use as donors [103], but the intrinsic wavelength tunability, rising from quantum confinement, could lead to a more efficient coupling with the peak of detectability of photodetectors. For these reasons, we produced and tested CdSeS/ZnS in PSS samples, monitoring the real-time luminescence under proton beam

As previously reported irradiation with high energy sources induces a quench of the QD luminescence in embedded samples [104–106]. The degradation is ascribed to the formation of radiation-induced defects in the ligands surrounding the nanocrystals with creation of surface trap states that quenches luminescence [104, 105]. Similarly, we investigated the behavior under proton beam instead of high energy photons because of the large spreading of proton beams in cancer therapy treatments. In fact, protons have gained an enormous attention in medical physics due to their ballistic behavior, releasing most of their energy at the end of the ionization track and therefore preserving the healthy surrounding tissues during cancer treatments. In this framework, passive dosimeters based on luminescence yield variation of QDs embedded in matrices can serve as accurate radiation dose indicators to verify the dose delivery and the control the beam. The interest behind the use of nanocrystals as probe for the radiation is driven by the intrinsic core-shell structure composed of a radiation-hard core (CdSeS/ZnS) and a radiation-weak shell (organic ligands). However, ligands have been found to contribute significantly to the overall PL, therefore a deepening on the radiation-induced damaging and luminescence yield monitoring is required. For these reasons, we monitored the luminescence in CdSeS/ZnS QD embedded in polyvinyl alcohol (PVOH), observing an enhancement of the PL in certain conditions. We monitored the emission spectrum and lifetime before and after proton beam irradiation to investigate the presence of energy transfer mechanisms and their efficiency.

4.2 Experimental

Commercial CdSeS/ZnS quantum dots (stabilized with octadecylamine) with emission wavelength centered at 540 ± 10 nm were employed for the experiments.

For the first experiment, CdSeS/ZnS QDs were dispersed in PSS1418 matrix at a concentration of 0.003, 0.015, 0.03, 0.3 and 1% wt. with a circular shape (Φ = 20 mm) and 5 mm thick as reported in Figure 4.1.

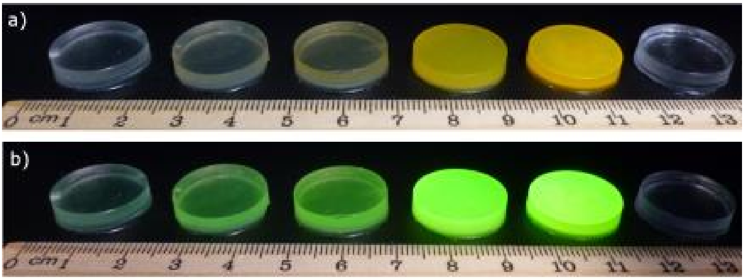

FIGURE 4.1: PSS1418 samples loaded with different amount of QDs under ambient (a) and UV light (b). The first sample on the right is the bare matrix.

Steady-state and time-resolved photoluminescence characterization were performed before proton beam irradiation at the AN2000 Van de Graaf accelerator (INFN-LNL, Italy). 2 MeV protons, with a beam spot of 3x3 mm^2 and a beam current of 40 nA corresponding to $\approx 2.8 \cdot 10^{12} \frac{H^+}{cm^2 s}$, were shot on the samples for 195 s while continuous acquisitions of 1 s were collected with the spectrometer (in front-face geometry).

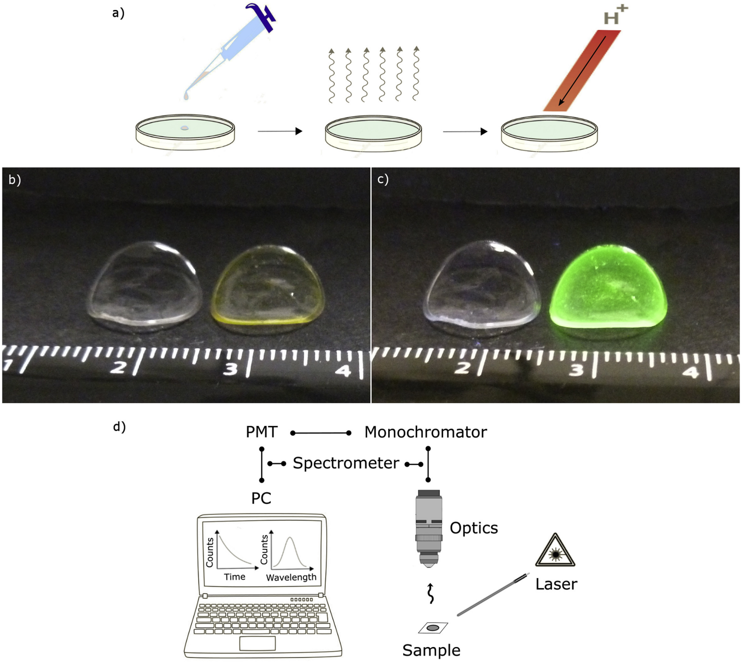

FIGURE 4.2: (a) Schematics of the PVOH-doped deposition and exposure, (b) unloaded and CdSeS/ZnS loaded PVOH sample under ambient light, (c) unloaded and CdSeS/ZnS loaded PVOH sample under UV light, (d) scheme of the steady-state and time-resolved measurement setup [107].

CdSeS/ZnS QDs were also dispersed in poly-vinyl alcohol (PVOH), starting from a 10% wt. water solution, and diluted to a final concentration of 0.7 mg/ml. The mixture was casted in circular molds of 10 mm diameter and let dry overnight in free air. Six samples with a final thickness of 70 ± 10 μm were obtained. The samples were irradiated at the AN2000 accelerator under 2 MeV proton beam with beam spot of 3x3 mm^2 and beam currents between 5 nA and 10 nA. The corresponding flux was calculated to be $\approx 5 \cdot 10^{12} \frac{H^+}{cm^2 s}$. QD-loaded and unloaded samples were irradiated with $10^{13}, 5 \cdot 10^{13}$ and $10^{14} \frac{H^+}{cm^2}$. Two samples were kept un-irradiated for comparison. Considering the thickness of the samples and the proton energy, all the ions are implanted in the sample releasing 2 MeV energy, as computed through SRIM simulation (Figure 4.3). Steady-state and time-resolved photoluminescence was investigated using a 405 nm laser diode with 10 MHz repetition rate.

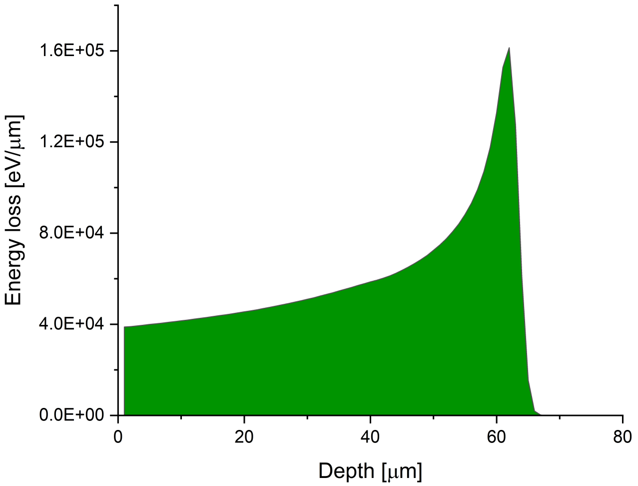

FIGURE 4.3: SRIM simulation of 2 MeV protons (H^+) in PVOH.

4.3 Results and discussion

4.3.1 QDs in poly-siloxanes (PSS)

At first, an optical characterization with the spectrophotometer and under 285 nm pulsed-LED excitation was carried out. Excitation and emission spectra of pure PSS matrix and QD loaded matrix are reported in Figure 4.4.

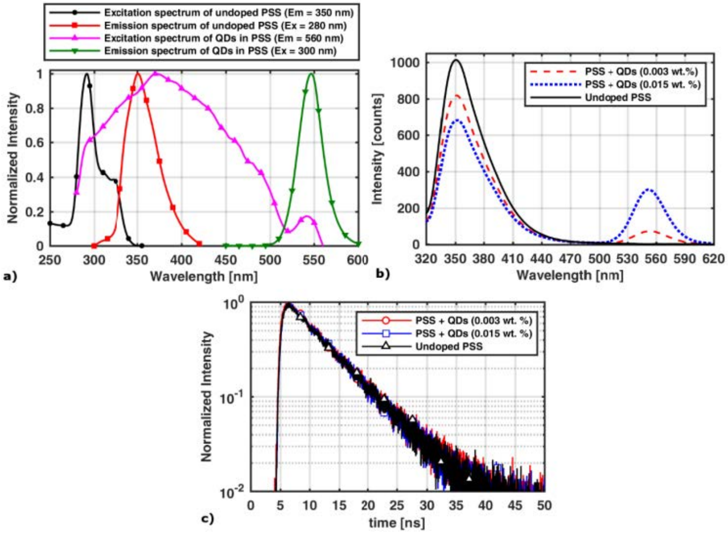

FIGURE 4.4: (a) Combined excitation-emission spectra of PSS and QD-loaded PSS matrix, (b) emission of PSS and QD-loaded PSS matrix under 285 nm LED excitation, (c) time-resolved measurements under 285 nm excitation (350 nm collection) [100].

As visible in Figure 4.4a, the emission spectrum of the matrix is peaked around 350 nm and overlays well the excitation spectrum of quantum dots. In this way, the hypothesis of energy transfer between the matrix and the QD finds the basic condition for taking place. In Figure 4.4b, the emission spectra of pure and loaded PSS matrix are reported, showing that the 350 nm emission decreases with the increase of QD loading. Moreover, the emission of QD at 550 nm increases with the concentration, suggesting the occurrence of energy transfer. However, when dealing with Förster type mechanisms, the donor lifetime (matrix) should be affected by the presence of the acceptor (quantum dots) [108]. To investigate this behavior, time-resolved measurements were acquired under nano-second pulsed LED source at 285 nm. The resulting decay curves are reported in Figure 4.4c, where no significant changes can be appreciated. The absence of non-radiative energy transfer between the matrix and quantum dots was previously investigated by *Clapp et al.* [102], that attribute the possible cause to a difference in the radiative lifetime between the fast decay of the matrix and the slow FRET decay due to a long exciton lifetime of the acceptor. However, the excitation spectrum of QDs extends far in the UV region, meaning that the recorded increase of signal derives from a direct QD contribution correlated with the concentration.

In order to investigate deeper QD-matrix optical interaction, IBIL measurements were carried out.

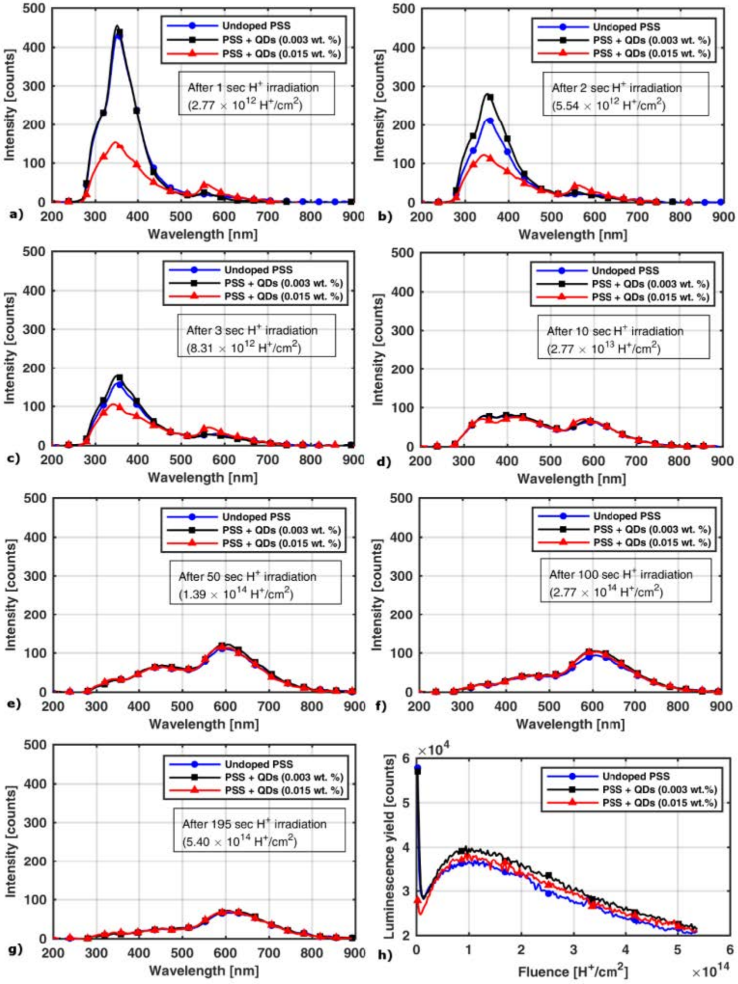

FIGURE 4.5: (a) → (g) Emission spectra under proton beam (different exposure times: 1, 2, 3,10, 50, 100 and 195 s), (h) integral of the emission contributions as function of the fluence [100].

Figure 4.5 reports the changes in spectral emissions under proton beam at different fluences (exposure times). As it can be noticed, the interaction of the proton beam with the sample induces significant changes from the beginning of the irradiation procedure, with the progressive decrease of the matrix emission at 350 nm, in accordance with all the optical measurements, and the rise of the QD emission at 550 nm. Even if the excitation mechanisms under proton beam occurs via secondary electron generated along the particle track [14], the recorded results gives the same emission bands as under UV excitation. The increase in the 550 nm emission band associated with QD emission arises from radiation-induced defects such as radicals. These phenomena may lead to the cleavage of a Si-O-Si bond in the matrix, resulting in an altered optical emission.

In general, the integral of each luminescence spectrum as a function of the fluence (Figure 4.5h) shows a slight luminescence yield increase that can be quantified as +8% for the 0.003% wt. and a +3% for the 0.015% wt. QD concentration. If we consider the QD optical contribution as negligible, the increase in light yield is correlated with nanocrystals high-Z sensitization. In fact, the sensitization due to inorganic nanocrystals embedded in an organic matrix is a mechanism that effectively converts γ-photons into photoelectrons [109].

The high average Z of QDs enhances the ionization energy released along the particle track leading to an increase of scintillation light yield. However, the enhancement was limited due to the low amount of QDs embedded in the matrix.

4.3.2 QDs in polyvinyl alcohol (PVOH)

In a similar way to the sensitization experiment, CdSeS/ZnS QDs embedded in polyvinyl alcohol (PVOH) were irradiated with 2 MeV protons at different fluences. Intensity resolved and wavelength resolved measurements were monitored as a function of the fluence and are depicted in Figure 4.6.

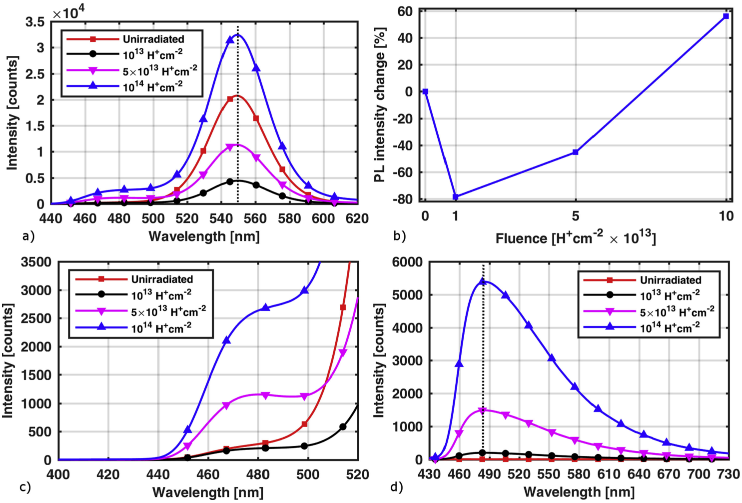

FIGURE 4.6: (a) Luminescence spectra of CdSeS/ZnS in PVOH under 405 nm excitation, (b) PL emission yield as function of the fluence, (c) enlargement of the radiation-induced luminescence band (d) emission spectra of unloaded sample after proton irradiation [107].

Steady-state PL measurements were collected under 405 nm laser excitation (Figure 4.6a) showing a substantial variation of the PL yield as a function of the fluence. The initial fluence ($10^{13}\frac{H^+}{cm^2}$) causes an drop of luminescence yield (-80%, Figure 4.6b) that is partially recovered for the intermediate fluence and overcome (+55%) for the highest fluence ($10^{14}\frac{H^+}{cm^2}$). Moreover, the irradiation does not induce any significant peak shift for the QD emission band but the growth of a new PL band peaked around

480 nm. This feature (Figure 4.6c) was previously observed for in similar samples embedding CdSeS/ZnS QDs in PVOH [110] and is ascribed to a radiation-induced damaging of the polymeric network. To prove this hypothesis, Figure 4.6d shows the emission of unloaded PVOH samples subjected to the same fluences. The appearance of blue band at 480 nm with intensity proportional to the fluence suggests that the interaction of protons with the polymer generates radicals, leading to the formation of unsaturated $C = C$ bonds and finally to graphitic clusters.

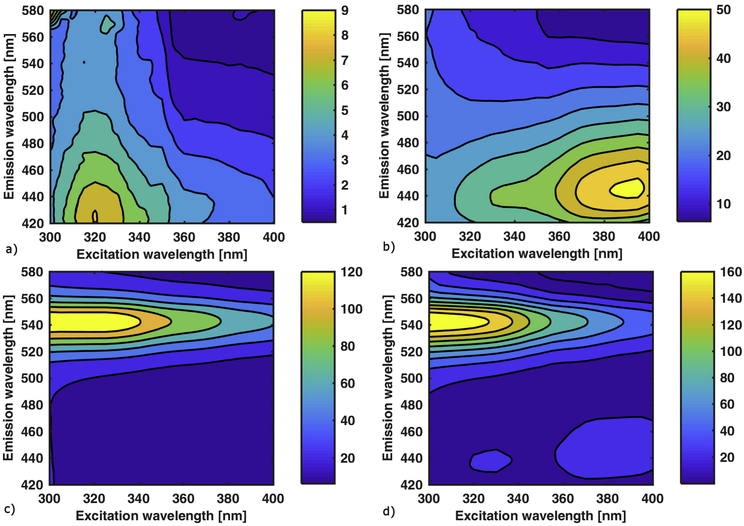

FIGURE 4.7: Contour plots of: (a) un-irradiated unloaded PVOH, (b) irradiated unloaded PVOH ($10^{14} \frac{H^+}{cm^2}$), (c) un-irradiated loaded PVOH and (d) irradiated loaded PVOH ($10^{14} \frac{H^+}{cm^2}$). The intensity scale is reported [107].

A deeper investigation was performed with conventional spectrofluorimetric measurements. Contour plots in Figure 4.7 shows the emission of different samples under UV excitation (300÷400 nm range). It can be noticed that the unloaded un-irradiated sample (Figure 4.7a) shows a signal comparable to the background level, meaning that no significant contributions are present, while the corresponding irradiated sample (Figure 4.7b) shows a blue band at 450 nm, in accordance with the previous laser measurements (Figure 4.6). Similarly, for un-irradiated and irradiated loaded samples (Figure 4.7c and d, respectively) a substantial increase in the light yield is recorded upon irradiation.

The recovering and increase in PL QD yield are attributed to energy transfer mechanisms between the radiation-induced defects in the matrix (donor) and the quantum dots (acceptors). As for the previous case of sensitization (subsection 4.3.1), lifetime measurements were carried out to prove the energy transfer mechanisms between donor and acceptor.

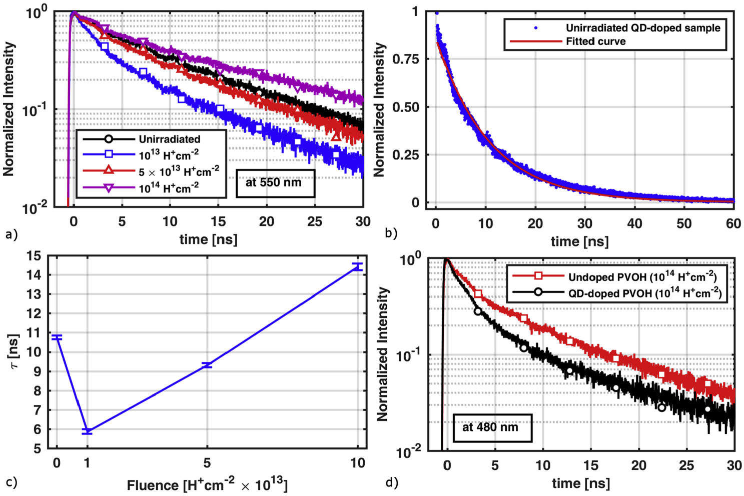

FIGURE 4.8: (a) lifetime decay curves measured at 550 nm (QD emission, acceptor), (b) example of fitted curve, (c) lifetime as function of the fluence and (d) lifetime decay curves measured at 480 nm (matrix emission, donor) [107].

Figure 4.8a shows the lifetime curves measured at the QD emission wavelength for un-irradiated and irradiated samples. It can be noticed that the fluence causes an initial drop of the lifetime, followed by a substantial increase for the highest fluence ($10^{14}\,\frac{H^+}{cm^2}$). For a better understanding, the results of fitting are plotted in Figure 4.8c as function of the fluence. It can be noticed that a strong correlation between the PL intensity (Figure 4.7b) and the decay lifetime (Figure 4.8c) exists. A single-exponential model was employed to fit the experimental curves (Figure 4.8b) following the equation (4.1):

$$I = A \cdot e^{-\frac{t}{\tau}} \tag{4.1}$$

A similar result was obtained for the un-irradiated and irradiated ($10^{14} \frac{H^+}{cm^2}$) by measuring the lifetime at 480 nm (donor). The curves reported in Figure 4.8d shows a substantial decrease of the lifetime in presence of the acceptor (QD), meaning that an energy transfer occurs. In particular, the donor lifetime decreases from 7.1 $\pm$ 0.2 ns in undoped PVOH to 3.8 $\pm$ 0.1 ns in QD-doped PVOH, meaning that the efficiency of energy transfer is $\approx$ 46%.

4.4 Summary

The effects of 2 MeV protons on the energy transfer mechanisms have been reported. On one hand, the effect of proton irradiation on CdSeS/ZnS loaded PSS matrix showed the absence of Förster resonance energy transfer (FRET) from the matrix to the quantum dots; whereas in the case of CdSeS/ZnS loaded PVOH matrix a non-radiative energy transfer mechanism was proved to occur. In the first case, the absence was ascribed to the dominance of the relatively fast radiative decay of the matrix compared to the slow FRET decay rate. Moreover, the optical measurements indicated the possibility of a radiative energy transfer (RET) mechanism with the absorption of a matrix-emitted photon by the QDs and the consequent emission at the QD characteristic wavelength. This hypothesis was also proved by measuring the response under proton beam excitation.

Conversely, PVOH samples showed a non-radiative energy transfer mechanism between the radiation-induced defect centers and the quantum dots, that lead to a recovery and an enhancement of the emitted light yield. These results demonstrate that quantum dots, in certain conditions, can act as acceptors in non-radiative energy transfer mechanisms.

In general, QDs are less effective in the matrix sensitization with respect to conventional organic dyes. QDs cannot be treated with the molecular theory of energy transfer, probably because the energy transfer mechanism is different and not characterized by the same problems.

Chapter 5

Fabrication of zinc oxide loaded flexible scintillators

Part of this section is going to be published in:

Journal of Applied Physics ARTICLE scitation.org/journal/jap

"Optical and radioluminescence properties of ZnO:Zn as a function of reduction degree and treatment temperature"
M. Favaro, R. Ceccato, S. Diré, E. Callone, A. Quaranta

Flexible scintillators based on ZnO:Zn loaded PDMS were realized and tested under alpha particles, X-rays, gamma rays and proton beam excitation. A commercial ZnO powder was heat treated for 2 hours in a furnace under Ar/H_2 flow (3%) to promote reduction. Different batches of powders were thermally reduced at temperatures ranging between 600 °C and 1000 °C. Pristine and treated powders were morphologically, structurally and optically analyzed before being incorporated in PDMS and PSS matrices. At first, the evaluation of the reduction degree was obtained through SEM/EDS analysis and stoichiometry reconstruction. The value of reduction ranges from 0% for the pristine powder up to 25% for the 1000 °C sample. X-ray diffraction measurements highlighted a substantial crystallite and grain growth with the increase of temperature, as confirmed by SEM imaging. The powders average grain size increase from 0.35 ± 0.15 μm to 6.4 ± 1.6 μm, with a remarked decrease of the relative size dispersion. The skeletal density follows a similar trend, decreasing from 5.63 ± 0.02 $\frac{g}{cm^3}$ for the pristine powder to 4.74 ± 0.02 $\frac{g}{cm^3}$ for the 1000 °C sample.

The reduction effect with modification of the oxygen vacancies and recombination dynamics was investigated with ESR measurements. Laser-induced PL measurements showed a remarked increase of the defective luminescence yield correlated with oxygen vacancies and an increase of the slow recombination component in PL dynamics measurements. A small bandgap contraction upon thermal reduction was measured via diffuse reflectance, with a decrease from 3.25 eV to 3.21 eV. Radioluminescence measurements showed promising results with an increase of luminescence yield as a function of the reduction degree, similarly to UV-excitation measurements. Alpha particle scintillation was observed upon exposure to a ^{241}Am source, with promising results for the PDMS matrix. Finally, IBIL measurements were acquired at the AN2000 Van de Graaf accelerator at the INFN-LNL (Laboratorio Nazionali di Legnaro, Padova, Italy) facility under 1.8 MeV proton beam, showing an optical response similar to UV and X-rays excitation.

5.1 Introduction

So far, as of today, zinc oxide have been widely investigated and employed in many different fields. Being re-discovered in the ’60s owing to its optical and electrical properties, it has re-attracted interest in the last decade for its scintillation behavior under mixed radiations [51, 111–115]. Beside scintillation, it is currently used in other technological application including solar cells [116–118], transparent transistors and UV-absorbing sunscreens [25, 119]. The luminescence features can be tuned by doping with different elements or by adjusting the stoichiometry. Non-stoichiometric zinc-rich phosphors (ZnO:Zn) are characterized by a remarked green luminescence that is the convolution of several transitions involving point defects present in the crystal structure. The hexagonal cell, in fact, is ideal for hosting different type of defects, such as Zn interstitials (Zn_i), Zn vacancies (V_{Zn}), oxygen interstitials (O_i) and oxygen vacancies (V_O). All these defects contributes to the visible emission of zinc oxide within different spectral region, from green (Zn-related defects) to red (O-related transition) [120–123]. All these features makes ZnO:Zn interesting for applications such as field emission display [46], flat panel display [47], optoelectronic components [47, 48] and white LED [124, 125].

ZnO single crystals, powders or thin films are generally produced using a variety of techniques such as melt grown [126], magnetron-sputtering [127], hydrothermal growth [128–130] ,CVD [131] or carbothermal reduction [112].

As previously introduced, ZnO has also been investigated as potential scintillator for mixed radiations. Characterized by a high radiation hardness and a fast excitonic transition, pure ZnO has been tested under X-rays and alpha particles showing promising results [42, 126, 132, 133]. However, a remarked increase of the performance is achieved only by doping with trivalent elements, such as gallium [132, 134] or indium [45, 135, 136], that creates an n-type doping. Both elements reduces the visible slow fluorescent component and enhances the fast near-UV transition, at the expenses of reduced light yield. In particular, gallium doping increases the sensitivity toward α-particles while decreasing the scintillation decay time [41, 115, 132, 133]. Beside the doping effect on α-particle sensitivity and scintillation decay time, the synthesis technique and atmosphere were reported to affect the luminescence light yield and the emission dynamics [41]. A remarked increase of light yield in gallium-doped ZnO was reported by *Derenzo et al.* [50] after synthesis in H_2-rich atmosphere, enabling for active an modification of oxygen and zinc vacancies and resulting in a decrease of the emission lifetime.

Additionally, the Ga-doping offers a unique feature to ZnO:Ga that resides in the pulse shape discrimination (PSD) capability, being the material able to respond in a different way depending on the interacting radiation (α-particle, γ-ray, etc.) [42, 137]. This feature is extremely important for a proper mixed radiation detection capability, however it has been partially proved only in the case of gallium doping.

Beside doping with additional elements, self-doped ZnO:Zn phosphors have been partially explored under X-rays [138] and charged particle sources

[36, 50, 139] showing promising results [49–52]. In particular, the possibility of pulse shape discrimination of the incident radiation was hypothesized by *Chen et al.* [42].

Moreover, the detection of γ-rays and neutrons opens an important discussion on the overall interest for zinc oxide structures. The use of powder-based systems limits the detection capabilities and no proper Compton edges can be detected [38].

Traditional ZnO systems based on the excitonic emission possesses response speeds faster than claimed fast plastic scintillators [38, 140], making it attractive for high count rate and timing applications.

In the neutron detection field, ZnO:Zn/^{6}LiF detectors can be an alternative to conventional ZnS:Ag/^{6}LiF by detecting the same reaction products but being less expensive and with low afterglow, at the expense of a light output that is on average just half of the ZnS:Ag-based [139].

ZnO:Zn powders can be easily obtained by thermal reduction in H_2-rich atmosphere and can be fitted in flexible detectors [11] by embedding in a flexible matrix. Polysiloxane-based flexible detectors offers conformability and real-time detection of the dose delivered to the patient in radiotherapy treatments.

In general, hydrogen reduction deeply affects the photoluminescence behavior, with a remarked increase of the defective emission ("green emission") that is ascribed to oxygen vacancies and zinc interstitial [27]. Moreover, the temperature effect is not limited to an increase of the diffusion coefficient of hydrogen with consequent increase of the reduction degree, but the size effect connected with the coalescence phenomenon and the modification of oxygen vacancy levels allows to obtain different phosphors [49].

A deeper investigation on the effects of hydrogen reduction on ZnO:Zn phosphors was proposed by *Vanheusden et al.* [27, 28], who investigated the mechanism of green luminescence with complementary techniques to understand the role of oxygen vacancies and defects. For this purpose, ESR measurements were extensively run [29, 141–143] to determine the role of vacancies and interstitials on the final luminescence. They pointed out that the reduction mechanism itself is influenced by other parameters like the treatment temperature and the atmosphere composition.

Based on these experimental evidences, we systematically studied the reduction of zinc oxide powders in the temperature range between 600 and 1000 °C. We found that this temperature range is extremely critical for many properties that are correlated with the reduction degree. Based on the ZnO:Zn phosphors, we realized a series of flexible multi-layered detectors based on PDMS or PSS resins. The samples gave promising results under X-rays, α-particle, γ-rays and proton beam excitation.

5.2 Experimental

Commercial zinc oxide (Baker, 99.0 %, labeled as "TQ") was heat-treated in a silica furnace in controlled atmosphere to produce zinc-rich ZnO powders. Batches of powder were annealed in Ar/H_2 atmosphere (3% vol. H_2, 97% vol. Ar) in the temperature range between 600 °C and 1000 °C (corresponding labeling in Table 5.1). After the thermal treatment, each batch was crushed in a mortar before being characterized. Pristine and reduced powders were investigated with X-ray diffraction (XRD), scanning electron microscopy (SEM), energy dispersive spectroscopy (EDS), diffuse reflectance (DR), photoluminescence (PL), X-ray radioluminescence (XRL); PDMS composites were also investigated under α-particle scintillation and proton-beam luminescence spectroscopy (IBIL).

Electron paramagnetic resonance (ESR) measurements investigated the presence and behavior of vacancies and defects correlating their effects on luminescence and recombination dynamics. Scintillation was observed under x-ray with a collimated Co source for powders and composites, α-particles with a ^{241}Am source, γ-rays from ^{133}Ba, ^{137}Cs, ^{60}Co sources and H^+ beam with a Van de Graaf accelerator for the PDMS composites.

The characterized powders were employed to fabricate ZnO:Zn loaded poly-dimethyl-siloxane (PDMS) samples. Multilayers were produced by first drop casting a base PDMS matrix, followed by a top loading with a 20:80 (% wt.) mixture of powder in resin. Figure 5.1 illustrates the procedure used to prepare the multi-layers.

PDMS was selected for its superior transparency and flexibility, although its intrinsic scintillation contribution is negligible because of the absence of phenyl groups. However, other phenyl-rich PDMS-based resins were tested: PSS1418, PSS22 and PSS100. The increasing phenyl content resulted in an unexpected decrease of the light yield under UV and negligible response under X-ray excitation, making these samples not attractive for the development of a flexible scintillator. The phenyl-containing matrices, in fact, were selected for the specific optical emission band centered around 340 nm, that matches the absorption edge of zinc oxide, theoretically allowing for a matrix-particle energy transfer.

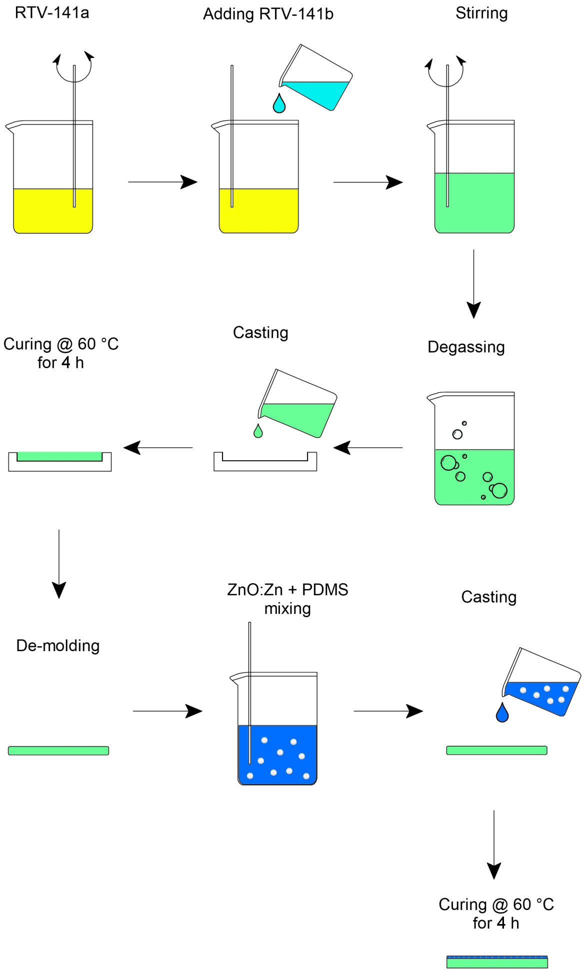

FIGURE 5.1: Preparation scheme for casting of transparent supports and loading with the active material.

PDMS base resin (part A) was mixed with PDMS hardener (part B) in a 10:1 ratio, followed by degassing at room temperature and casting of 0.80 g of compound in circular molds of 20 mm diameter. Molds were placed in a vacuum oven at 60 °C for 4 hours to promote crosslinking. After demolding, 1.5 mm thick fully transparent circular support were obtained. The active layer containing ZnO:Zn phosphor was produced by mixing a specific amount of powder with the PDMS resin (part A + B, degassed) in a 20:80 % by weight ratio. A specific amount of mixture (powder + resin) was casted on top of the transparent support to obtain a thin layer of controlled thickness ($\approx 250\,\mu m$). The active layer thickness was carefully engineered to obtain a full absorption of 5.5 MeV alpha particles from the ^{241}Am source without a remarked loss of UV-excited photons.

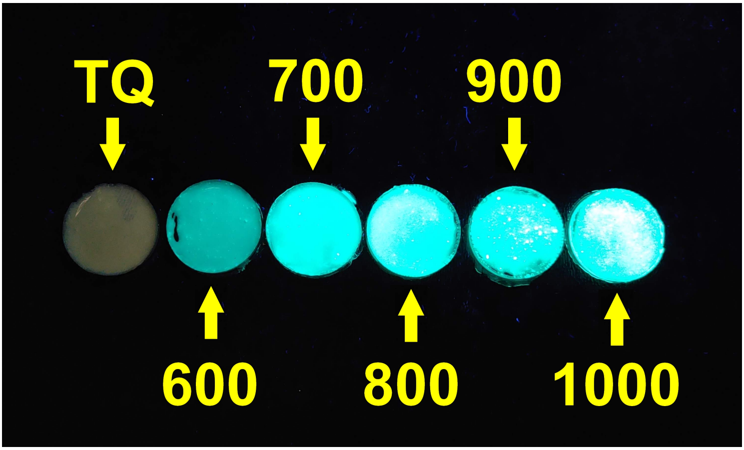

FIGURE 5.2: ZnO:Zn loaded PDMS samples showing photoluminescence upon excitation with a 365 nm UV lamp as function of the reduction temperature.

Sample	**Treatment T [°C]**	**Reduction degree [%]**	**Label**
TQ	-	0 ± 2	TQ_0
600	600 °C	7 ± 1	600_7
700	700 °C	13 ± 2	700_13
800	800 °C	20 ± 2	800_20
900	900 °C	23 ± 1	900_23
1000	1000 °C	25 ± 1	1000_25

TABLE 5.1: List of samples with the corresponding heat treatment, reduction degree and label.

5.3 Results and discussion

5.3.1 ZnO and ZnO:Zn powders

To study the effects of thermal reduction on ZnO powders in Ar/H_2 atmosphere, a commercial powder was heat treated in the temperature range between 600 °C and 1000 °C and characterized in terms of structural, morphological and optical properties.

At first, the evaluation of the reduction degree was obtained through EDS measurements and stoichiometry reconstruction. The EDS spectra (Figures 5.3a) shows the characteristic signals of zinc oxide with zinc K- and L-lines and oxygen L-lines, combined with the platinum and palladium L-lines derived by the top conductive coating. No other contamination are detected.

In Figure 5.3b a clearly increasing trend in the zinc atomic content is visible starting from 50% at. in pristine powder to 62% at. in the 1000_25 sample. The zinc curve, and for symmetry the oxygen curve, shows that the content at 1000 °C is close to reach a plateau condition. From these values it can be calculated the corresponding reduction degree, listed in Table 5.2, that ranges from 0% for pristine to 25% for the 1000_25 sample. The trend is linearly increasing in the temperature range between 600 °C and 800 °C, while it increases at a slower rate between 800 °C and 1000 °C.

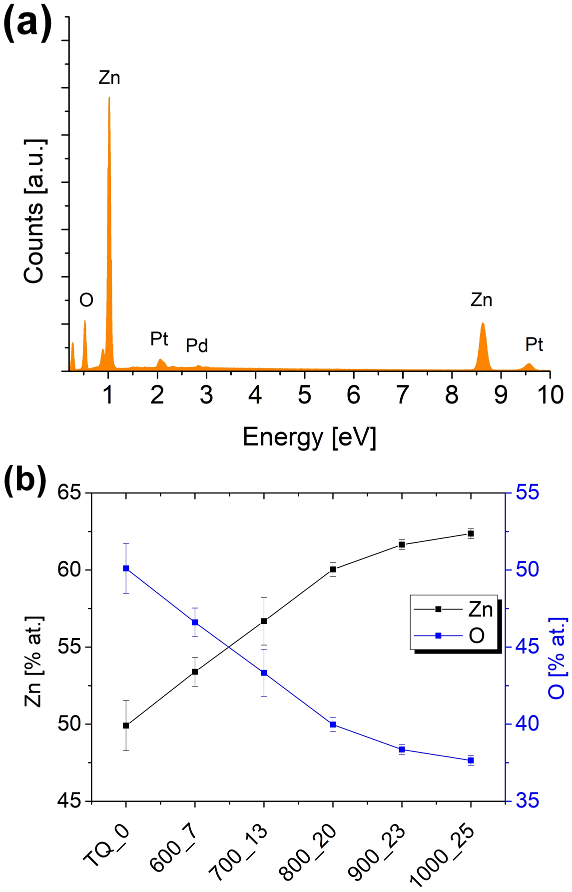

FIGURE 5.3: EDS spectra of the pristine powder (a) and atomic concentration (b) as function of the treatment temperature.

Sample	**SEM grain size [μm]**	**Zn [% at.]**	**O [% at.]**	**Reduction degree [%]**
TQ_0	0.35 ± 0.15	50.0 ± 2.0	50.0 ± 2.0	0 ± 2
600_7	0.45 ± 0.15	53.4 ± 0.9	46.6 ± 0.9	7 ± 1
700_13	0.45 ± 0.15	56.7 ± 1.5	43.3 ± 1.5	13 ± 2
800_20	1.7 ± 0.6	60.0 ± 0.5	40.0 ± 0.5	20 ± 2
900_23	2.5 ± 0.9	61.6 ± 0.3	38.4 ± 0.3	23 ± 1
1000_25	6.4 ± 1.6	62.4 ± 0.3	37.7 ± 0.3	25 ± 1

TABLE 5.2: Average SEM grain size, Zn and O_2 content from EDS measurements, and estimated reduction degree as a function of the treatment temperature.

Combined with the EDS comes also the SEM imaging analysis on the grain size. Figure 5.4 shows the top-view of untreated and reduced powders showing a remarkable growth effect. In fact, the average grain dimension (Table 5.2), measured with ImageJ software (v. 1.53c), is estimated to range from 350 ± 150 nm for the pristine powder (TQ_0) to 6.4 ± 1.6 μm for the highest treatment temperature sample (1000_25). This effect is ascribed to high temperature coalescence, that drives a substantial variation of the surface-to-volume ratio with remarked consequences on the optical properties.

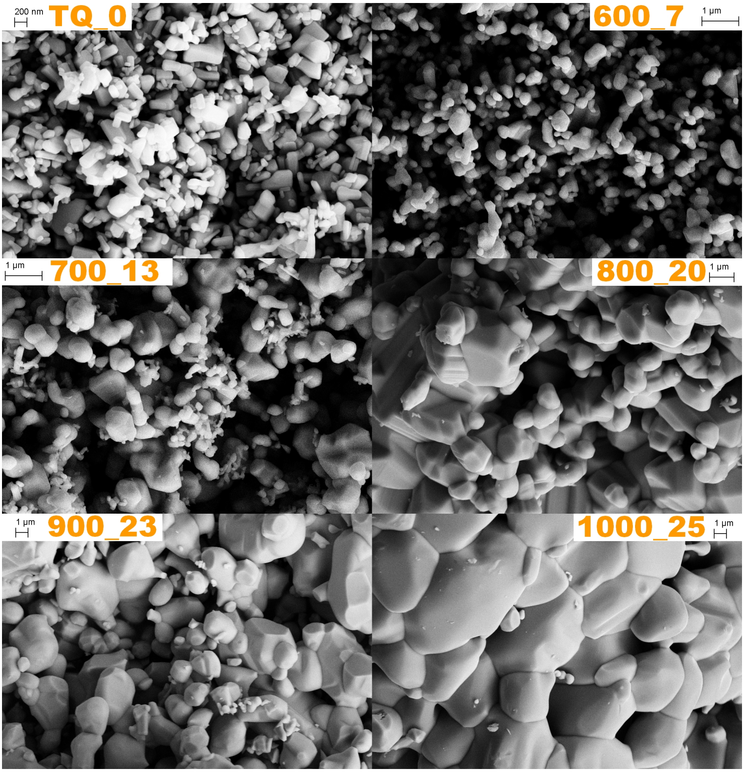

FIGURE 5.4: SEM top-view of the pristine and treated powders.

The size dispersion (Table 5.2), that at a first approximation can be estimated with the standard deviation of the diameter, changes significantly between 700 °C and 800 °C, where we hypothesize that coalescence becomes predominant. Therefore, the size dispersion above this temperature threshold is very small because of a massive growth with incorporation of the smaller grains in the bigger ones.

To support the structural analysis, X-ray diffraction patterns were acquired on pristine and reduced powders to get information on the crystallinity, average crystallite size and texture effects. The diffraction patterns for the pristine and reduced powders are shown in Figure 5.5. All the patterns are characterized by the presence of nine main peaks observed at 2θ = 31.80°, 34.42°, 36.23°, 47.43°, 56.37°, 62.61°, 66.04°, 67.66°, 68.79° which correspond to (100), (002), (101), (102), (110), (103), (200), (112) and (201), respectively. Other minor peaks are detected at 2θ = 89.11° and 94.77° corresponding to (203) and (211), respectively. All the peaks detected are ascribed to hexagonal (wurtzite) zinc oxide, without impurities. The pristine powder crystallinity is high, with crystallite dimension of 192 ± 1 nm, and is retained upon thermal treatment with a final crystallite dimension of 1057 ± 14 nm for the 1000 °C sample. No evident texture effect is detected, as confirmed by the calculation of the degree of orientation (always close to 1) [144]. The characteristic lattice parameters for the hexagonal cell a,c does not change significantly with the treatment (a = 3.2691 Å, c = 5.2357 Å) but are generally higher than the JCPDS standard (a = 3.2498 Å, c = 5.2066 Å). The purification and calcination methods used in at industrial scale to produce bulk quantities of ZnO can affect the final parameters, inducing remarked differences with the standard material. As a matter of fact, the computation of the theoretical density [145] gives values in good agreement with the measured skeletal density obtained through pycnometry (Table 5.3) and the JCPDS card value.

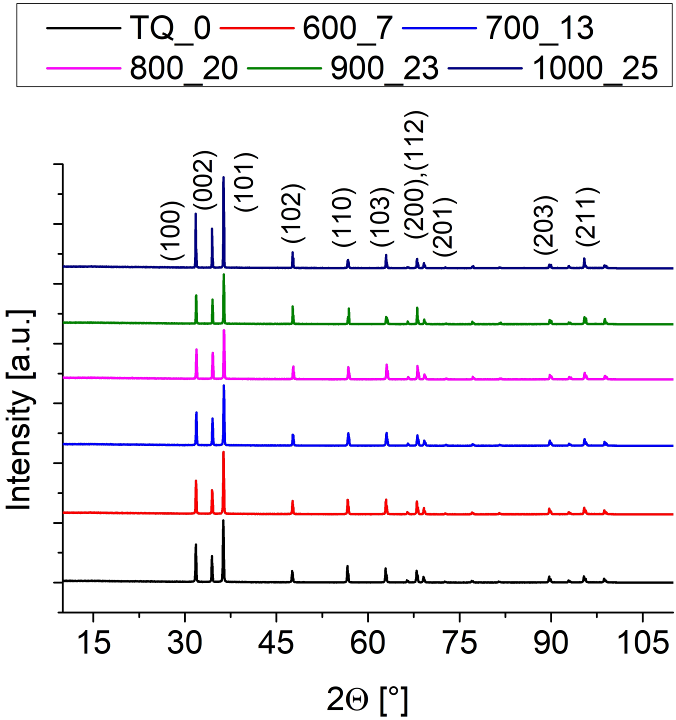

FIGURE 5.5: X-ray diffraction pattern as function of the reduction temperature (main peaks and corresponding plane family are reported).

Skeletal density measurements were assessed via helium pycnometry. The experimental values are reported in Table 5.3, where they can be compared to the corresponding theoretical value obtained with Equation 5.1 (for TQ_0) and 5.2 (for all the other samples). The experimental density starts from 5.63 ± 0.02 g/cm^3 (TQ_0) and reaches 5.2 ± 0.1 g/cm^3 for the 1000_25 sample. As it can be noticed, the initial values is close to the JCPDS standard (ρ = 5.675 g/cm^3), whereas the difference between experimental and theoretical values increases along the reduction series because the theoretical equations (Eq. 5.1, 5.2) does not account for the formation of shell vacancies.

$$\rho_{th} = \frac{2 \cdot MW_{ZnO} \cdot 1.6605}{(\frac{\sqrt{3} \cdot a^2 \cdot c}{2})} \tag{5.1}$$

where MW_{ZnO} is the molecular weight of zinc oxide and the denominator represents the cell volume.
However, equation 5.1 should be adapted in order to obtain a correct estimate of the density when losing oxygen from the cell structure.
Equation 5.2 gives a better estimate by accounting for the presence of zinc in the ZnO structure:

$$\rho_{th} = \frac{2 \cdot (MW_{ZnO} \cdot \chi_{ZnO} + MW_{Zn} \cdot \chi_{Zn}) \cdot 1.6605}{(\frac{\sqrt{3} \cdot a^2 \cdot c}{2})} \tag{5.2}$$

Sample	**Density [g/cm^3]**	**Theoretical density [g/cm^3]**
TQ_0	5.63 ± 0.02	5.675
600_7	5.38 ± 0.01	5.596
700_13	5.38 ± 0.01	5.529
800_20	5.35 ± 0.01	5.451
900_23	5.33 ± 0.01	5.417
1000_25	5.2 ± 0.1	5.395

TABLE 5.3: Skeletal density measured through helium pycnometry.

Alongside with the other structural and compositional analyses, ESR measurements on pristine and reduced powder were acquired. The ESR spectrum of the pristine powder shows only one resonance at g = 1.9596, whereas all the reduced samples shows the main resonance alongside with minor signals. Interestingly, the heat treatment in H_2 seems to have a double effect: on one side, it increases the intensity of the main peak up to 800 °C, followed by a significant reduction for the 900_23 and 1000_25 samples; on the other side, it causes the appearance of a new signal at g = 2.0010

for the 600_ and 700_13 samples, that disappears when exceeding 800 °C in favor of a new feature at g = 2.0105, that increases up to 1000 °C. The specific area over mass values for each signal are reported in Table 5.4.
Following the works reported in the literature, the main signal at g = 1.9596 is ascribed to singly-ionized oxygen vacancies ($V_0^{\bullet}$) [27, 141, 146, 147], while the features at g = 2.0010 and g = 2.0105 are generally assigned to zinc vacancies [148–150].

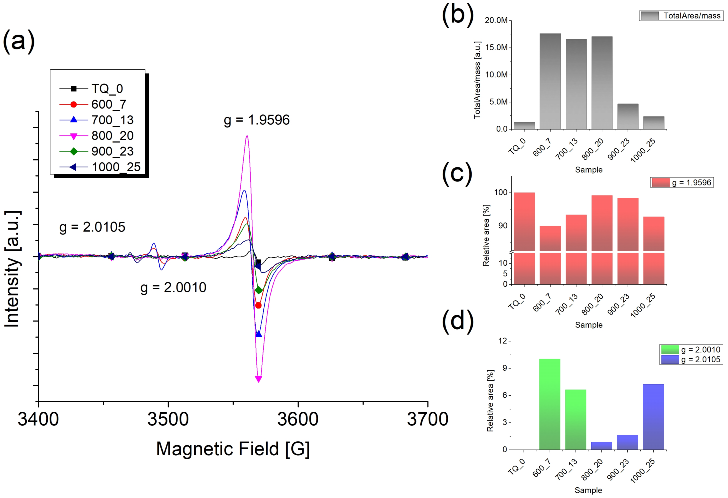

FIGURE 5.6: (a) CW-ESR spectra of the pristine and treated powders, (b) total area over mass, (c) relative area for the main signal at g = 1.9596, and (d) relative area for minor signals at g = 2.0010 and g = 2.0105.

Sample	**Total area/mass $[\frac{cm^2}{g}]$**	**Area/mass $[\frac{cm^2}{g}]$ (g = 1.9596)**	**Area/mass $[\frac{cm^2}{g}]$ (g = 2.0010)**	**Area/mass $[\frac{cm^2}{g}]$ (g = 2.0105)**
TQ_0	$1.3 \cdot 10^6$	$1.3 \cdot 10^6$	-	-
600_7	$1.8 \cdot 10^7$	$1.6 \cdot 10^7$	$1.8 \cdot 10^6$	-
700_13	$1.7 \cdot 10^7$	$1.6 \cdot 10^7$	$1.1 \cdot 10^6$	-
800_20	$1.7 \cdot 10^7$	$1.7 \cdot 10^7$	-	$14.8 \cdot 10^4$
900_23	$4.7 \cdot 10^6$	$4.6 \cdot 10^6$	-	$7.6 \cdot 10^4$
1000_25	$2.3 \cdot 10^6$	$2.2 \cdot 10^6$	-	$17.0 \cdot 10^4$

TABLE 5.4: ESR total area over mass and single defects contributions.

Laser induced fluorescence (Figure 5.7) acquired under 266 nm excitation (left) and 355 nm (right) shows an increasing light yield output as function of the reduction temperature. The two different excitation wavelengths allows to highlight luminescence contributions from different regions: surface related defects are likely to be excited under 266 nm, while the higher penetration depth of the 355 nm excitation gives rise to fluorescence signals mainly from the core. In the spectra acquired under 266 nm excitation (Figure 5.7, left) the defective emission shows a remarked increase in the light yield while the excitonic emission is strongly suppressed. The excitonic to defective band ratio changes from 24:1 down to 0.01:1 as a function of the reduction degree. The defective emission band, centered around 520 nm, grows of about three orders of magnitude with the reduction temperature reaching the upper detection limit. A similar trend is observed also under 355 nm excitation (Figure 5.7, right) where the excitonic emission is also clearly visible. The main ZnO and ZnO:Zn emission are reported in Figure 5.8, associated with the energy levels.

The increase of PL intensity with the reduction degree is correlated with the combination at singly-ionized and non-ionized oxygen vacancies centers, giving both a green emission. However, ESR is only able to investigate the singly-ionized V_O, so the saturation at 800 °C is showing only one face of the medal.

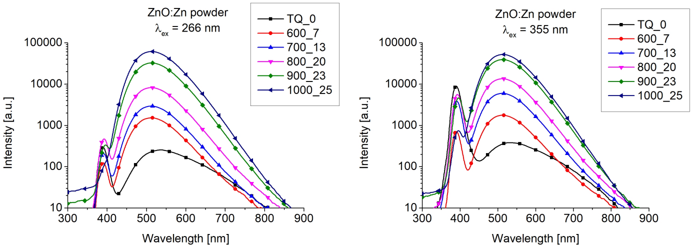

FIGURE 5.7: PL spectra (log-scale) under $\lambda_{ex} = 266$ nm (left) and $\lambda_{ex} = 355$ nm (right) laser excitation as function of the reduction temperature.

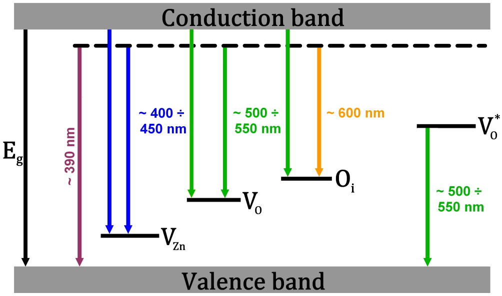

FIGURE 5.8: Schematic diagram of ZnO:Zn energy levels and transitions.

A deeper analysis of the PL spectra is proposed in Figure 5.9, where the effect of the single luminescence contributes is analyzed with a peak deconvolution under λ_{ex} = 266 nm excitation. This wavelength was selected because it excites surface related defects, therefore it allows to probe the role of defects as a function of the reduction degree and of the surface-to-volume ratio. Three main components are observed: the excitonic component at 390 nm and two defective components at 500 nm and 550 nm. The near band-edge emission intensity drops from an initial 13.7 % (TQ_0) of the overall emission down to 0 % for the 1000 °C sample, while the defective emission evolution more complex. Starting from the TQ_0 sample, it an be noticed that the defective band can be due to the convolution of three transitions, one at 500 nm, one at 550 nm and one around 600 nm. While the former two are also present in the other samples, the latter affects only the pristine powder and could be related to the presence of interstitial oxygen that is lately removed with the thermal treatment. The convolution of such defects generates a band centered around 540 nm for the TQ_0 sample that rapidly moves to 520 nm for all the reduced phosphors, as a result of the convolution of 500 nm and 550 nm transitions only. Moreover, the increase in light yield of the defective band at 520 nm (convolution of the two single contributions) is ascribed to electron transitions between the conduction band and singly ionized oxygen vacancy centers created with the thermal treatment [27, 49], together with other defects promoted by reduction. The measurement performed under 355 nm excitation source showed the same DBE shift from pristine to reduced samples, with peak moving from 540 nm to 520 nm.

The relative amount of the 500 nm band does not change with the reduction temperature with respect to the 550 nm band, meaning that the single contributions are likely to come from the same defect.

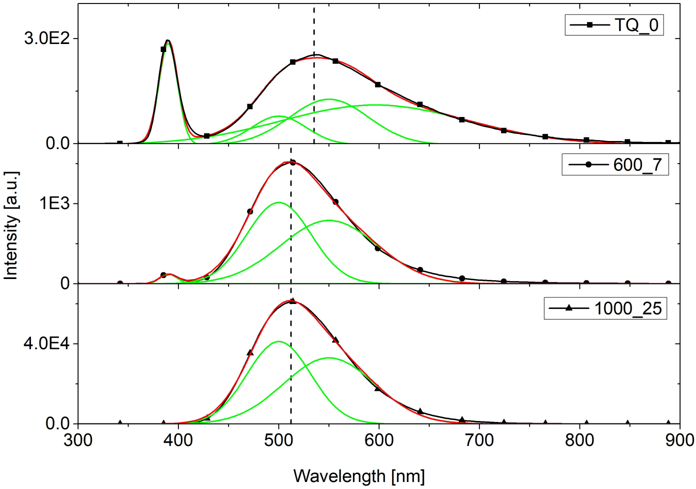

FIGURE 5.9: Peak deconvolution analysis of the TQ_0, 600_7 and 1000_25 reduced powders under 266 nm excitation.

$$I(t) = A \cdot e^{-\left(\frac{t}{\tau}\right)} \tag{5.3}$$

$$I(t) = A_s \cdot e^{-\left(\frac{t}{\tau_s}\right)} + A_f \cdot e^{-\left(\frac{t}{\tau_f}\right)} \tag{5.4}$$

The PL dynamics lifetime for the excitonic and defective emission are reported in Figure 5.10,5.11. The excitonic emission dynamics is characterized by a mono-exponential decay (Eq. 5.3) while the defective emission by a double-exponential decay profile (Eq. 5.4, where A_s and A_f are the pre-exponential coefficients). Therefore, the excitonic emission is characterized by a single coefficient while the defective emission by two coefficients, formerly the fast (τ_f) and slow (τ_s) transitions. Error bars are within the marker size.

The excitonic lifetime shows a substantial decrease between the pristine and the first treatment temperature (600 °C) reaching a plateau that is retained for all the treatment temperatures. The values measured are in good agreement with previously reported ones [25, 151]. The remarked decrease can be explained by the effect of hydrogen in the zinc oxide structure, that acts as shallow donor, enhancing the transition speed as occurring for other dopants [37, 41].

A completely different behavior is observed for the defective lifetime components, showing an increase of both the fast and slow components up to 900 °C, followed by an abrupt decrease for the 1000 °C sample. The remarked increase of the fast and slow components can be ascribed to a size scale-up effect, as previously observed by *Layek et al.* [152] and *Matsumoto et al.* [153], but also to the formation of surface traps, highlighted with the ESR measurements, that produces delayed fluorescence. In any case, the reduction effect by hydrogen treatment determines the creation of Zn-rich powders through modification and formation of point defects in the crystal lattice. This hydrogen doping-like effect is likely to be responsible for the intrinsic *n*-type behavior of zinc oxide in Zn-rich conditions, as previously reported by *Zhang et al.* [30]. Zinc interstitials (Zn_i) and ionized oxygen vacancies ($V_O^{\bullet}$) could represent the cause of such photoluminescence recombination behavior.

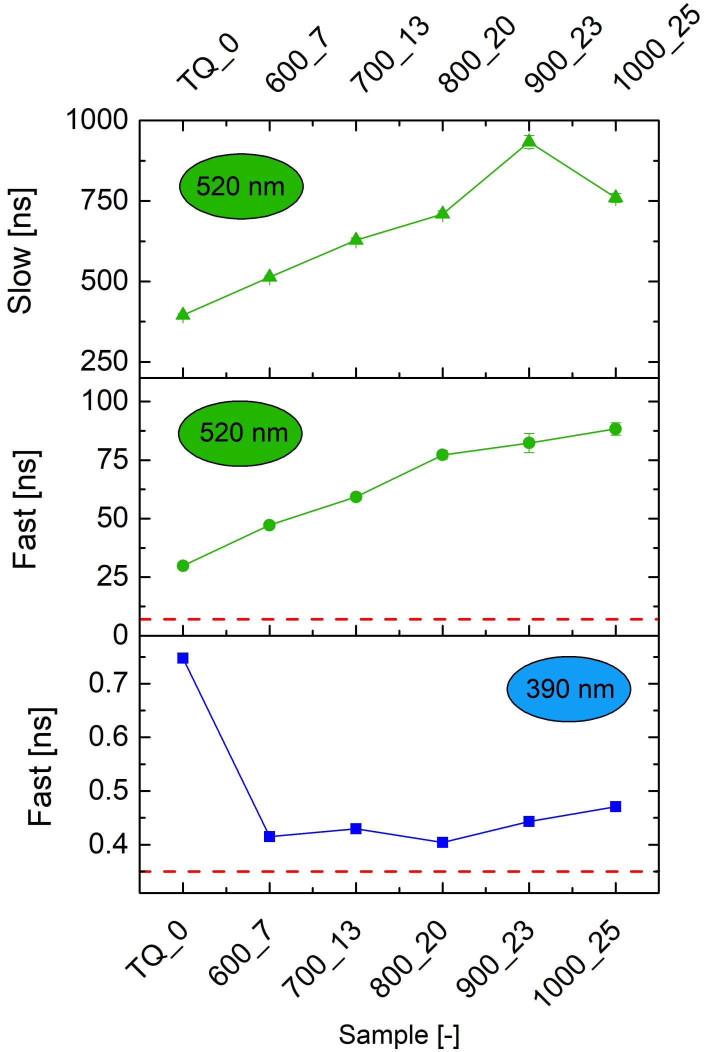

FIGURE 5.10: PL dynamics lifetime coefficients for the excitonic and defective emission (dashed line represents the laser pulse width).

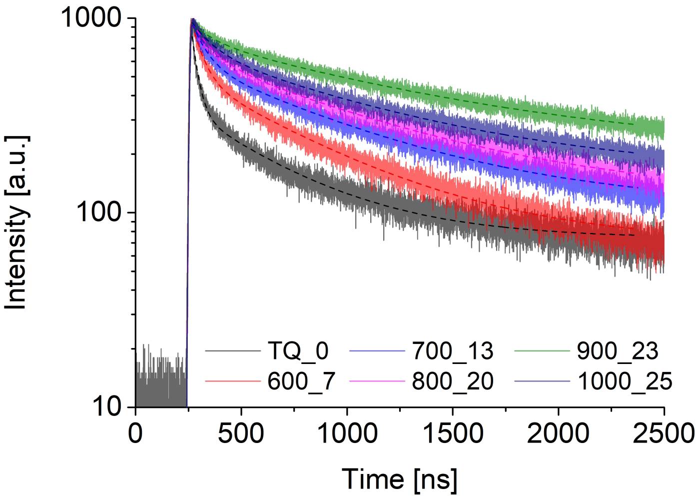

FIGURE 5.11: PL decay curves under 355 nm excitation (dashed-line represents the fitted trend).

In order to investigate the effect of defects on the bandgap, diffuse reflectance measurements were acquired and converted to $(F(R)h\nu)^2$ plots using the Kubelka-Munk theory [154]. The Tauc plots are reported in Figure 5.12, showing the part (yellow box) fitted for the linear extrapolation to the axis intercept. An esteem of the bandgap energy, in fact, is obtained by finding the intercept with the energy axis.

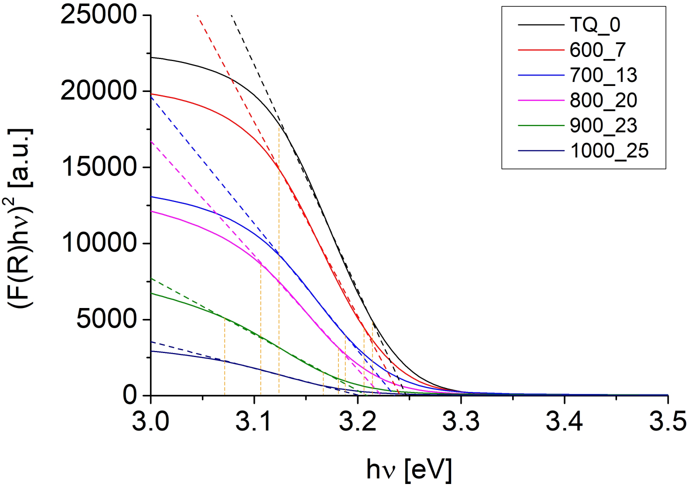

FIGURE 5.12: Tauc plot of the powders as a function of reduction degree.

A slight decrease of the bandgap energy is recorded as a function of the reduction temperature. The value for the pristine powder (3.25 eV) was also previously observed by *Makino et al.* [155] in ZnO nanorods and by *Rodnyi et al.* [156] on nanopowders. The value decreases as a function of the reduction temperature, dropping down to 3.21 eV for the 1000_25 sample, being in good agreement with previously reported values by *Hong et al.* [157].

As previously evidenced by SEM, ESR and PL lifetime measurements, the hypothesis of a critical temperature threshold is supported also by the bandgap measurements, showing an appreciable difference after the 800 °C. In any case, the evaluation of the band gap energy through diffuse reflectance measurements gives an esteem of the real energy value because is affected by the presence of defects that perturb the measurement.

Sample	Bandgap extrapolation [eV]
TQ_0%	3.25 ± 0.08
600_7	3.24 ± 0.08
700_13	3.24 ± 0.06
800_20	3.22 ± 0.08
900_23	3.21 ± 0.06
1000_25	3.21 ± 0.06

TABLE 5.5: Bandgap energy extrapolation from the Tauc plot.

In a similar way to the PL measurements, the exposition to a collimated X-ray beam produced a visible luminescence, formerly radioluminescence, that is reported in Figure 5.13. The log-scale emphasizes the increase of light yield that is achieved by the reduction treatment. In particular, the first samples (600_7, 700_13 and 800_20) shows a non-linear response with the reduction degree. Conversely, the most reduced samples (900_23 and 1000_25) exhibits a remarked light yield increase that occurs just above the hypothesized temperature threshold (near 800 °C). It can be noticed that the excitonic emission completely disappears while the defective emission increases. This effect was previously observed by *Rodnyi et al.*, *Demidenko et al.* and *Neal et al.* [51, 158, 159], and is correlated with the generation at specific luminescence centers. The complete disappearing of the excitonic emission have been reported by *Sykora et al.* [139] and *Santos et al.* [138], and was ascribed to self-absorption and scattering effects.

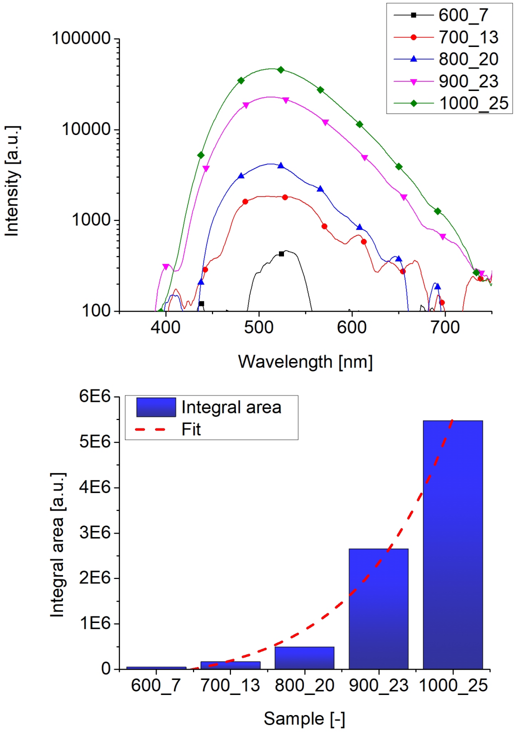

FIGURE 5.13: (a) Radioluminescence spectra under X-ray beam excitation and (b) total signal area as a function of the reduction degree.

5.3.2 Incorporation in PDMS and PSS matrices

After a complete characterization, the powders were incorporated in different polymeric matrices to build experimental multi-layered detectors. In particular, a base circular support of poly-dimethyl-siloxane (PDMS) was casted in disk-shaped samples with 20 mm diameter and $\approx$ 1.5 mm thickness. The superior transparency of PDMS in the visible range and its flexibility were exploited to produce supporting waveguides with good conformability. Samples were obtained by mixing the two components of the PDMS resin (part A and part B) in a 10:1 mass ratio. After degassing in a vacuum oven, the crosslinking was let to occur at 60 °C for 4 hours. A graphical representation of the casting procedure is visible in Figure 5.14.

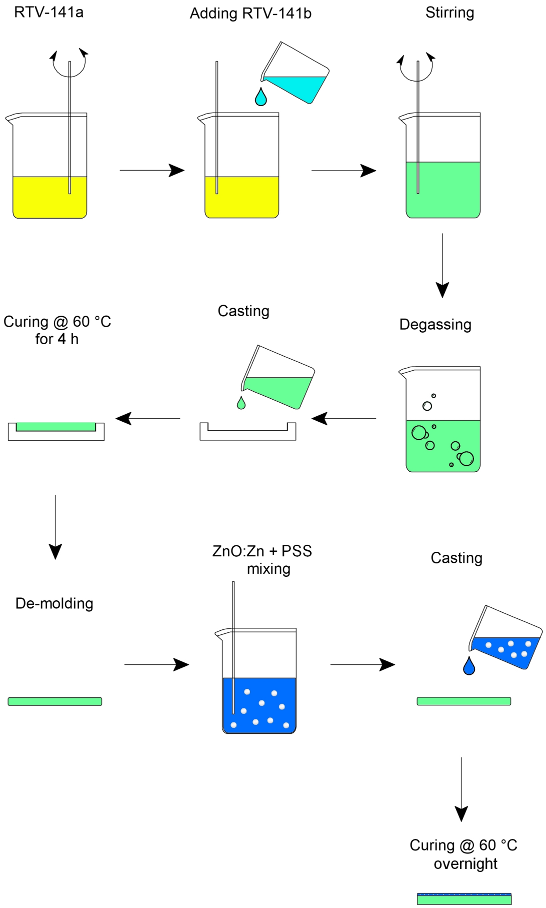

FIGURE 5.14: Graphical representation of the casting procedure for multi-layered samples.

After crosslinking, the transparent supports were loaded on top with a thin layer of ZnO:Zn powder (20 % wt.) dispersed in PDMS (80 % wt). The layer thickness was carefully engineered to ≈ 250 μm in order to maximize the alpha particle absorption while maintaining sufficient photon collection capability. The loaded layer was let to crosslink at 60 °C in vacuum oven for 4 hours.

A similar procedure was employed for the deposition of PSS-based samples, except for the crosslinking step that was done in vacuum oven at 60 °C overnight.

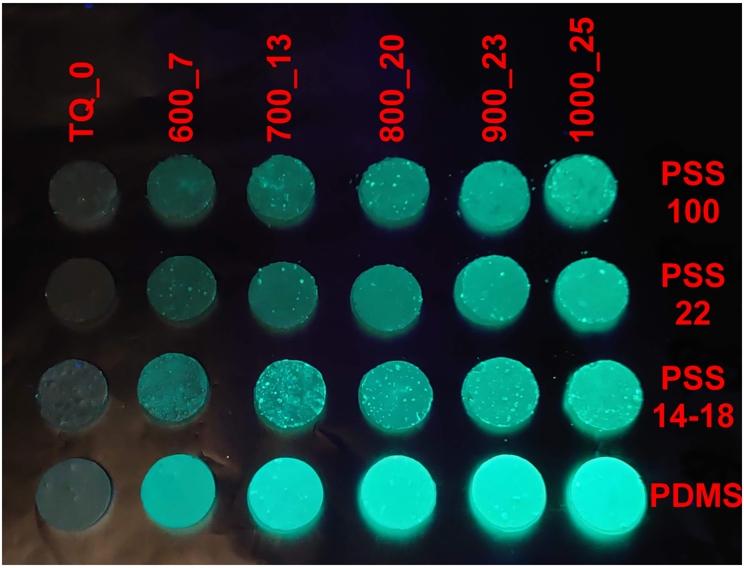

FIGURE 5.15: ZnO:Zn series in PDMS and PSS under UV excitation (λ_{ex} = 254 nm). Sample diameter was reduced to 10 mm in order to match the PMT photocathode.

The resulting samples (Figure 5.15) were optically characterized with steady-state PL measurements, radioluminescence measurements under X-ray excitation and scintillation measurements under α-particle, γ-rays and proton beam excitation (IBIL).

5.3.3 Mixed-radiation scintillation measurements

PSS-based systems

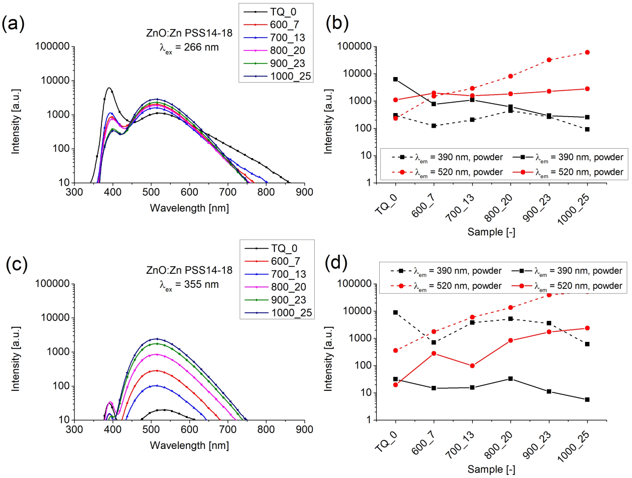

FIGURE 5.16: PL spectra under 266 nm (a) and intensity comparison (b), PL spectra under 355 nm (c) and intensity comparison (d) of ZnO:Zn powders embedded in PSS-1418 matrix.

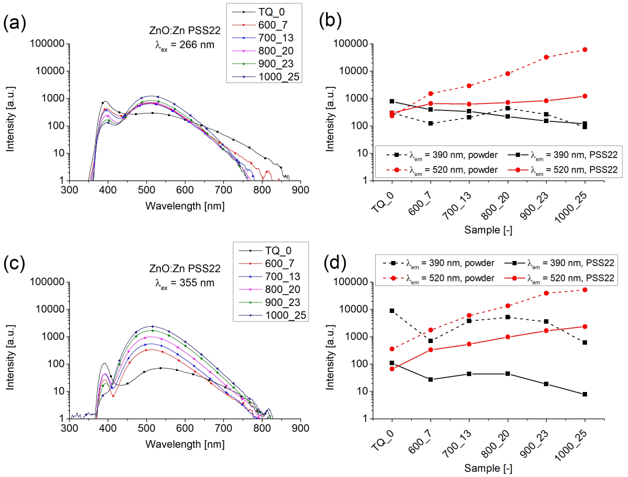

FIGURE 5.17: PL spectra under 266 nm (a) and intensity comparison (b), PL spectra under 355 nm (c) and intensity comparison (d) of ZnO:Zn powders embedded in PSS-22 matrix.

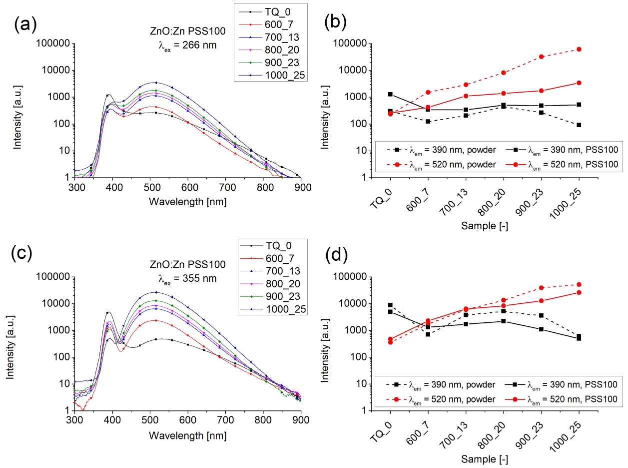

FIGURE 5.18: PL spectra under 266 nm (a) and intensity comparison (b), PL spectra under 355 nm (c) and intensity comparison (d) of ZnO:Zn powders embedded in PSS-100 matrix.

Different PL results are obtained for the powders embedded in PSS-1418 (Figure 5.16), PSS-22 (Figure 5.17) and PSS-100 matrices (Figure 5.18). The intensity of embedded powders in phenyl-containing resins is generally lower than the one in linear-chain PDMS resin, as a consequence of the direct absorption of part of the UV excitation light by the polymeric matrix. In fact, the experimental procedure of mixing the powder with the resin results in a thin layer of polymers covering the powder. This layer can interact with the impinging radiation and is the underlying cause of the absence of a peak in the alpha particle measurements.
Indeed, the polymeric capping layer was intentionally introduced in order to study the energy transfer from the matrix to ZnO:Zn phosphors. In fact, phenyl-containing PSS matrices have the maximum fluorescence emission in the 330 - 340 nm range. Such range partially overlaps to the ZnO:Zn phosphors absorption, that is peaked around 350 nm, making the energy transfer process possible. However, as observable in the PL graphs above, the PL intensity does not increase with the incorporation in PSS matrix, but decreases as a result of the absorption of the impinging radiation by the polymeric outer layer. Therefore, the work focuses on the use of PDMS matrix for the realization of multilayered composite systems.

PDMS-based systems

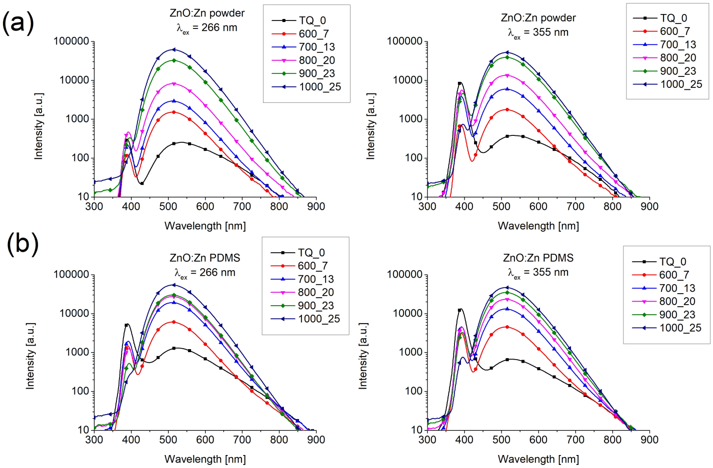

FIGURE 5.19: PL curves under UV excitation (λ_{ex} = 266 nm on the left, λ_{ex} = 355 nm on the right) of pristine and treated standalone powders (upper part) and after embedding in PDMS (lower part).

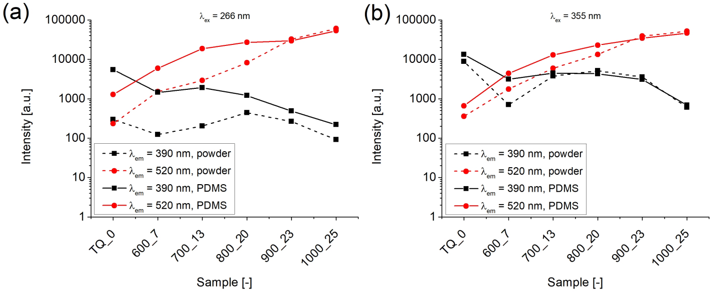

FIGURE 5.20: PL intensity for powders and PDMS embedded phosphors under (a) 266 nm excitation and (b) 355 nm excitation.

PL measurements under 266 nm (left) and 355 nm (right) UV-excitation are reported in Figure 5.19a,b. Spectra in Figure 5.19a refers to pristine and reduced powders while spectra in graph 5.19b shows the PL of powders embedded in PDMS. It can be noticed (Figure 5.20) that the embedding produces an increase of the PL intensity, being more remarked for low reduction degrees (samples TQ_0, 600_7 and 700_13), while less effective for high temperature treatments (above 800 °C). The PL spectra shows a slight blue-shift of the defective emission band from 540 nm to 520 nm (sample TQ_0) before and after the embedding in PDMS, as a result of effective polymeric capping with passivation of the surface defects.

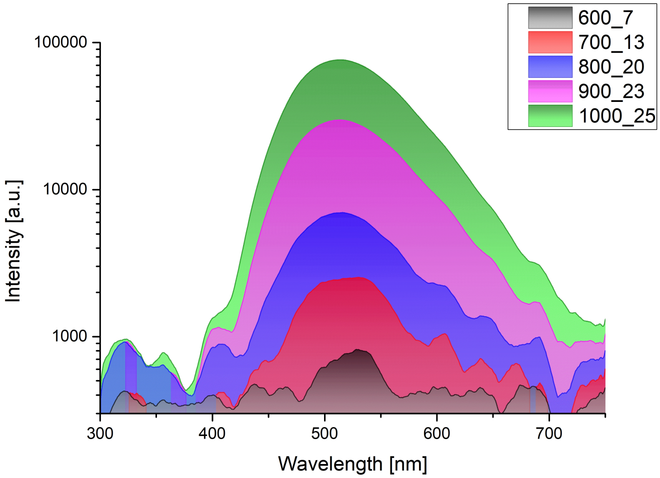

FIGURE 5.21: Radioluminescence under collimated X-ray beam excitation of ZnO:Zn powders embedded in PDMS sample.

The radioluminescence spectra of composite ZnO:Zn/PDMS samples under X-ray beam excitation are reported in Figure 5.21. As reported previously for the powders, the emission spectra are characterized by the presence of one peak only, ascribed to the defective emission of phosphors, whereas the excitonic emission is missing. In fact, the spectrum of sample TQ_0 is missing because of the flat radioluminescence response. The lack of the near UV component in radioluminescence spectra is intriguing because the collection setup, composed on a silica optical fiber, should be able to collect the emitted photons. The effect was previously observed and attributed to a self-absorption effect combined with scattering due to the bulk generation mechanism induced by X-rays [138, 139], however we hypothesize that it derives from the different excitation mechanism. In fact, for each X-ray absorbed one single electron is created, whereas in the case of IBIL protons creates a bunch on excited states. In any case, the main XRL signal lies around 520 nm, being in good agreement with the PL measurements.

As part of the scintillation measurements, alpha particle and gamma ray excitation measurements were carried out. The uncalibrated response under α-particle excitation is reported in Figure 5.22 and Figure 5.23. Samples were coupled with the photocathode of a fast PMT and the ^{241}Am source was putted in direct contact with the ZnO:Zn layer of the composite samples. As explained previously, the presence of a thin polymeric layer with passivation capability changes the alpha-particle absorption due to scattering and partial energy release. Therefore, as visible in the spectra (Figure 5.22,5.23), the characteristic quasi mono-energetic peak is not visible but is replaced with a continuous energy distribution. This response can be attributed to the combined effects of using powders and the presence of a thin polymeric layer, that holds the phosphors in place, producing scattering and energy losses effects at the interface.

In any case, a characteristic trend as a function of the reduction degree can be highlighted by extrapolating the bin number corresponding to the total integral. In fact, a deeper analysis of the energy distribution spectrum shows that the light yield of the two samples is different, with the extrapolation to the energy axis that reaches the 40000 bin for the 800_20 sample (Fig. 5.22) whereas the 50000 bin for the 1000_25 sample (Fig. 5.23). This increase of bin number is directly related to an increase of energy, since the total integral represents the integral of a scintillation pulse over a fixed interval (long gate, Sec. 3.12).

Due to this characteristic energy distribution and the long decay time of alpha interaction events, the direct comparison with typical scintillation standards (such as EJ-426 or CsI crystals) is difficult and was not possible.

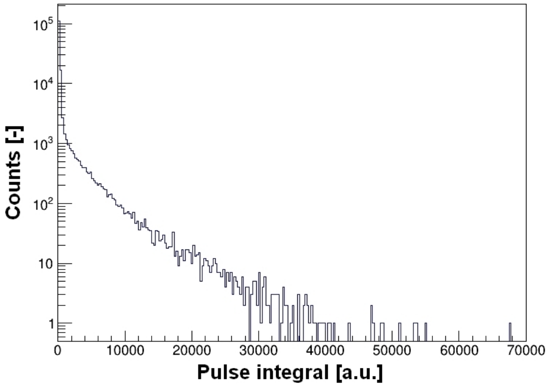

FIGURE 5.22: Scintillation under ^{241}Am α-particle source of the PDMS 800_20 composite sample.

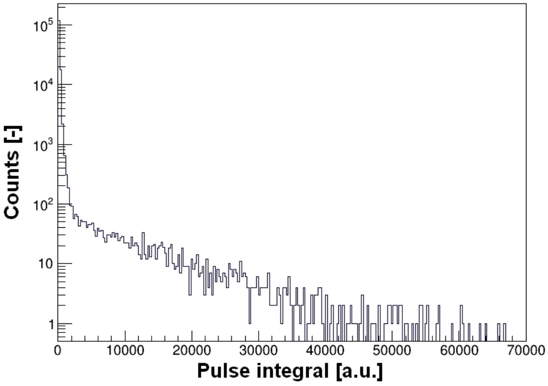

FIGURE 5.23: Scintillation under ^{241}Am α-particle source of the PDMS 1000_25 composite sample.

Based on these results, the scintillation measurements with gamma source were carried out only on the 1000_25 sample. The resulting spectra (uncalibrated) are reported in Figure 5.24. As observed for alpha scintillation, the gamma spectrum lacks of characteristic peaks (Compton edge or photopeak) due to the use of ZnO:Zn powders. The optimized thickness for alpha particle capture, in fact, in not sufficient for a good gamma conversion being the absorption depth too small.
However, as highlighted in alpha measurements, the use gamma sources with various energy produces a different response. This variation of response can be appreciated by observing the different intercept with the energy axis, that varies accordingly with the gamma photon energy (E_{Ba} = 207.26 keV < E_{Cs} = 477.34 keV < E_{Na} = 1061.71 keV). The gamma scintillation response derives only by interaction with the phosphor-containing layer because the matrix is not sensitive to such radiation.

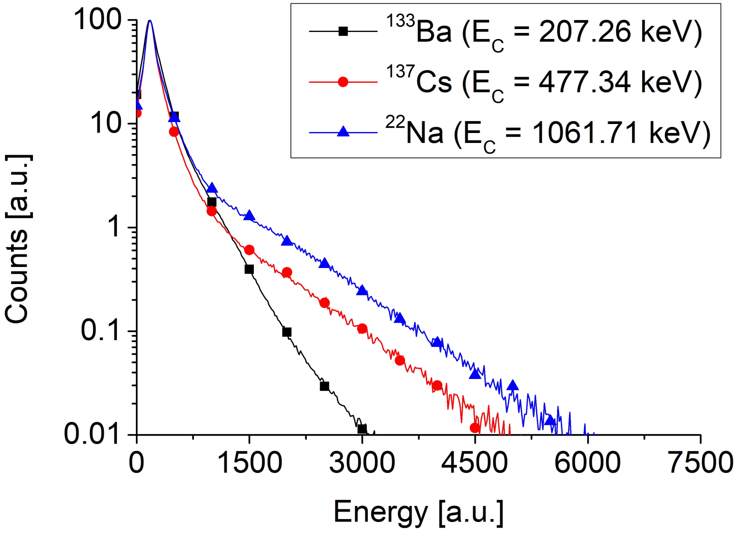

FIGURE 5.24: Scintillation response under ^{133}Ba, ^{137}Cs and ^{22}Na γ-sources of the PDMS 1000_25 sample.

5.3.4 IBIL measurements

To complete the scintillation analysis, ion-beam induced luminescence (IBIL) spectroscopy was carried out at the AN-2000 Van de Graaf accelerator at LNL laboratories. The wavelength-resolved luminescence response to 1.8 MeV proton beam after 30 seconds exposure (equivalent to $1.4 \cdot 10^{13}$ H^+/cm^2) is illustrated in Figure 5.25a. Irradiation parameters were calculated to be: flux equal to $\approx 4.7 \cdot 10^{11}$ $\frac{H^+}{cm^2\, s}$ for a beam current of 3 nA and a spot size of 2·2 mm^2.
The calculated penetration depth (Section 3.13), through SRIM simulation, of 1.8 MeV protons in PDMS is 72 ± 2 μm, so the entire proton energy is stopped and completely released in the phosphor-containing layer.

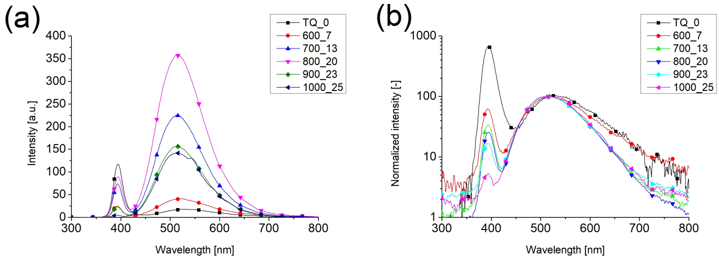

FIGURE 5.25: (a) Instant ion-beam induced luminescence curves acquired under 1.8 MeV proton beam excitation after 30 s exposure, (b) corresponding normalized spectra of ZnO:Zn/PDMS samples.

Figure 5.25b shows the freeze-shot normalized spectra of ZnO:Zn/PDMS samples after 30 seconds exposure (to ensure a proper beam current stabilization). Unexpectedly, the 800_20 sample is the brightest, being in disagreement with PL and XRL measurements, in which the increasing reduction degree produces an increase of the luminescence light yield. In this case, being the excitation mechanism much different from the previous ones, the maximum emission intensity is reached in agreement with the ESR signal of singly ionized oxygen vacancies, allowing to hypothesize that the green emission upon proton excitation is driven by that luminescence centers. Conversely, in PL and XRL, other defective states, such as zinc vacancies, contributes to the overall phosphor emission, giving an increase of light yield with the reduction temperature.

In any case, beside the luminescence intensity emission itself, IBIL measurements are extremely useful to study the irradiation damaging in real-time as a function of the proton fluence.

A deeper analysis is reported in Figure 5.26, 5.27 and 5.28. IBIL spectra are plotted at time t = 1 s, t = 10 s, t = 30 s and t = 60 s, corresponding to a fluence of $4.7 \cdot 10^{11} \frac{H^+}{cm^2}$, $4.7 \cdot 10^{12} \frac{H^+}{cm^2}$, $1.4 \cdot 10^{13} \frac{H^+}{cm^2}$ and $2.8 \cdot 10^{13} \frac{H^+}{cm^2}$, respectively.

The first seconds of irradiation produces a remarkable decrease of the fluorescence, that continuously drops as a function of the fluence. Along the phosphor series, the exposure to an increasing fluence of protons produces a decrease of the luminescence intensity, that could be correlated to radiation induced damaging of the polymeric matrix capping the luminescent powders. However, since the penetration depth of protons is in the range of few tens of micrometers, a direct damaging of the luminescent phosphors cannot be excluded. However, no visible losses of transparency or yellowing are visually detected after irradiation. Therefore, the luminescence quenching is likely to derive from radiation-induced trap states in the powder because, as reported previously [160], the radiation hardness of PDMS is high and this range of fluences is not sufficient to produce an appreciable amount of matrix-related defects.

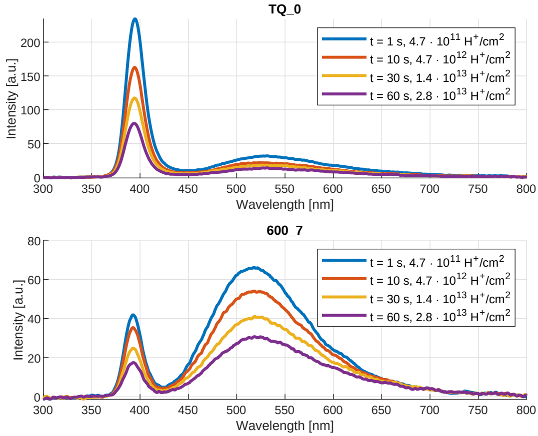

FIGURE 5.26: IBIL curves of TQ_0 and 600_7 samples taken at *t* = 1 s, 10 s, 30 s and 60 s.

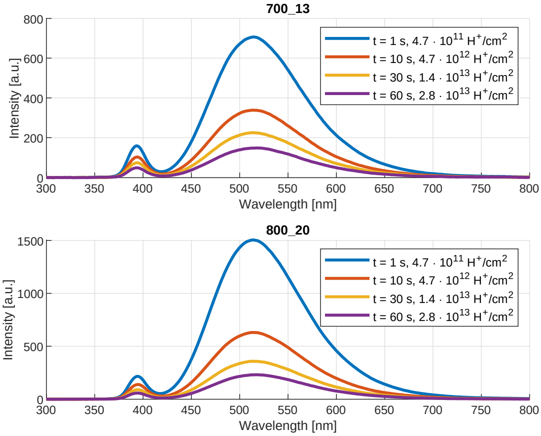

FIGURE 5.27: IBIL curves of 700_13 and 800_20 samples taken at *t* = 1 s, 10 s, 30 s and 60 s.

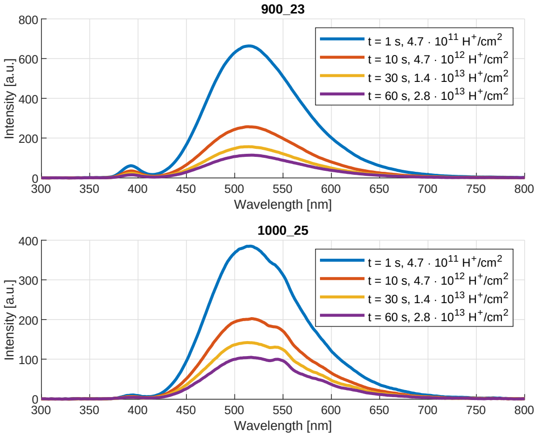

FIGURE 5.28: IBIL curves of 900_23 and 1000_25 samples taken at *t* = 1 s, 10 s, 30 s and 60 s.

As reported in Figure 5.25, the instantaneous defect-related luminescence band grows non-linearly as a function of the reduction degree, reaching a maximum for the 800_20 sample. ESR measurements on the phosphors agrees with IBIL experimental data, allowing to hypothesize that the charged-particle light response of the material can be correlated with defects lying at g = 2.0010, whereas the high-energy and UV photons (PL and XRL) produces a green emission that can be correlated with defects lying at g = 2.0105.

A more interesting feature appears in the emission spectrum of 1000_25 sample, in which a second peak centered at 550 nm pops up. As highlighted previously, the convolution of point defect emissions generates the luminescence band ranging from the blue-green region up to the red region of the spectrum. Many studies reported on generation and assignment of such luminescence band to the respective point defect [28, 47, 161]. Two separate contributions to the green band were isolated: one coming from isolated singly-ionized oxygen vacancies and one from complexes of such vacancies. Therefore, we hypothesize that the second peak emerging in the IBIL spectrum can be due to the luminescence from complexes of oxygen vacancies. This hypothesis is supported by ESR measurements, in which the intensity of the signal at g = 2.0105 grows to about 10% of the total signal in the 1000_25 sample. In any case, the assignment is not straight forward and a deeper investigation is required.

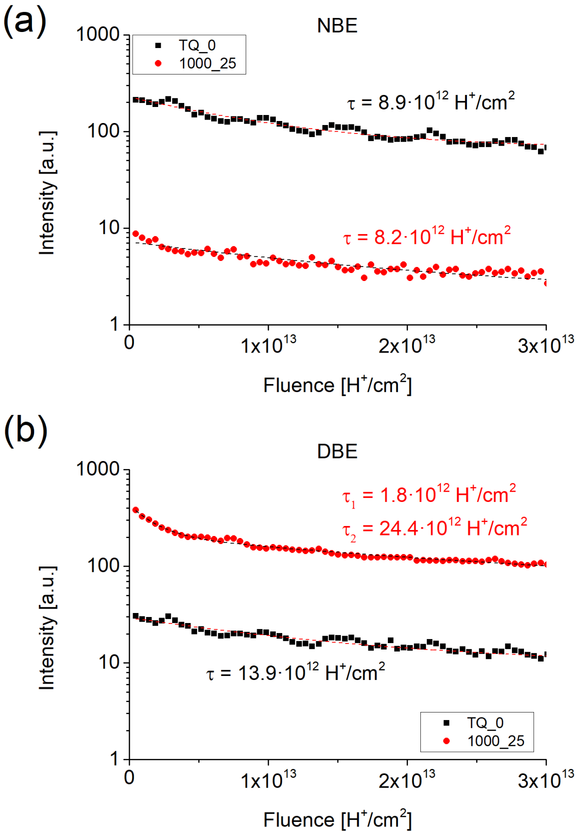

FIGURE 5.29: Log-scale light yield decay profile of: (a) near-band-edge emission at λ = 390 nm for the TQ_0 and 1000_25 samples, (b) defective band emission (DBE) at λ = 520 nm for the TQ_0 and 1000_25 samples as a function of the fluence (i.e. exposure time).

To study the damaging effects on the luminescence emission intensity, the maxima of excitonic and defective peaks were plotted as a function of the total fluence. Figure 5.29a shows the intensity decay profile of the near-band-edge emission for the TQ_0 and 1000_25 samples, while Figure 5.29b the decay profile of the defective emission. It can be observed that the NBE decay profile follows a single exponential model with time constants $\tau_{TQ\_0,\,NBE} = (8.9 \pm 0.3) \cdot 10^{12}\, H^{+}/cm^{2}$ and $\tau_{1000\_25,\,NBE} = (8.2 \pm 0.2) \cdot 10^{12} H^{+}/cm^{2}$.

A similar behavior is recorded for the DBE emission of TQ_0 sample, characterized by a decay constant of $\tau_{TQ\_0,\,DBE} = (13.9 \pm 2.8) \cdot 10^{12} H^{+}/cm^{2}$. Conversely, the DBE decay profile of the 1000_25 sample follows a double exponential decay model, with characteristic constants of $\tau_{1000\_25,\,DBE,\,fast} = (17.9 \pm 3.4) \cdot 10^{12} H^{+}/cm^{2}$ and $\tau_{1000\_25,\,DBE,\,slow} = (24.4 \pm 1.8) \cdot 10^{12} H^{+}/cm^{2}$.

Sample	τ_{NBE} [$\cdot 10^{12}$ H^{+}/cm^{2}]	τ_{DBE_1} [$\cdot 10^{12}$ H^{+}/cm^{2}]	τ_{DBE_2} [$\cdot 10^{12}$ H^{+}/cm^{2}]
TQ_0	8.9 ± 0.3	13.9 ± 2.8	-
600_7	-	-	-
700_13	7.8 ± 0.3	2.7 ± 0.2	17.9 ± 3.4
800_20	8.6 ± 0.2	3.3 ± 0.2	20.9 ± 5.7
900_23	7.9 ± 0.4	2.9 ± 0.2	35.1 ± 17.6
1000_25	8.2 ± 0.2	1.8 ± 0.2	24.4 ± 1.8

TABLE 5.6: Damaging threshold limit as a function of the reduction degree of the phosphor for NBE and DBE emissions.

Similar damaging threshold results are obtained along the phosphors series (Table 5.6) meaning that the radiation hardness is likely to be related to the phosphor material, as previously hypothesized.

5.3.5 α/γ pulse shape discrimination

As observed and hypothesized by *Chen et al.* [137], ZnO possesses intrinsic pulse shape discrimination capability. Given that such work presents only a preliminary study, a deeper analysis of the PSD capability of ZnO:Zn phosphors is presented.

In particular, sample 800_20 was selected as candidate for being tested under ^{241}Am and ^{137}Cs sources. The sample was coupled to a 1" inch fast PMT tube (Hamamatsu H6520) that is designed on purpose for scintillation. The ^{241}Am source (3 KBq activity) was placed closed to the sample (about 5 mm) while the ^{137}Cs source (10 μCi activity) at a distance of about 10 mm. The PMT raw signal was fed into a digitizer (CAEN DT5730) for the acquisition, while the PSD analysis was performed in post-processing. The PSD parameter was defined as:

$$PSD = \frac{Q_{tail}}{Q_{total}} \tag{5.5}$$

Total integral versus PSD parameter plots are reported in Figure 5.30a,5.31a and 5.32a.

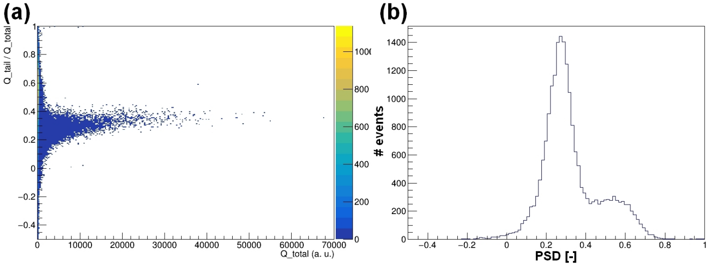

FIGURE 5.30: (a) Total integral versus PSD parameter for the 800_20 sample under ^{241}Am source, (b) PSD histogram of the events.

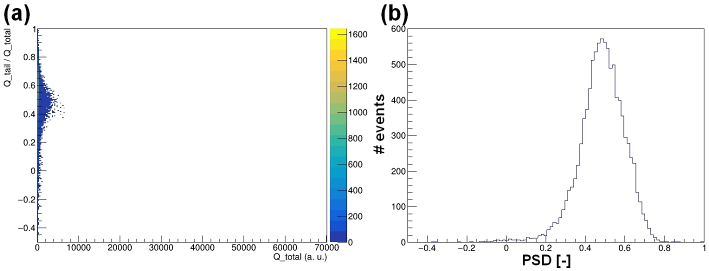

FIGURE 5.31: (a) Total integral versus PSD parameter for the 800_20 sample under ^{137}Cs source, (b) PSD histogram of the events.

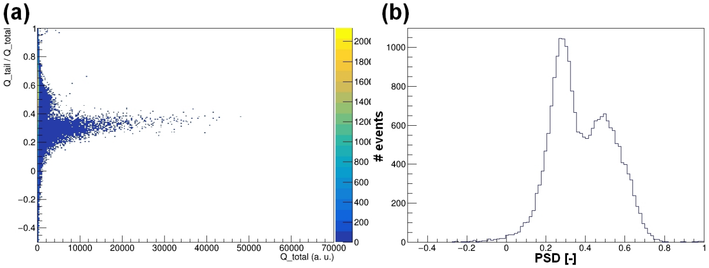

FIGURE 5.32: (a) Total integral versus PSD parameter for the 800_20 sample under ^{241}Am and ^{137}Cs source, (b) PSD histogram of the events.

The PSD parameter ranges between 0.2 and 0.4 for alpha interaction events, as it can be noticed in Figure 5.30a, while between 0.4 and 0.6 for gamma interaction events (Figure 5.31a).

Histograms of PSD events are reported in Figures 5.30b, 5.31b and 5.32b. It can be noticed that, in the case of ^{241}Am source only, a small shoulder peak in the gamma region is present. This peak is likely to derive from the 59.5 keV gamma emitted by the americium decay process.

Even though the sample and the acquisition parameters are not optimal, a PSD capability is visible (Figure 5.32 a,b). Generally, PSD is compared to standards through a Figure of Merit (FoM) that measures the separation of the two peaks in absolute terms, calculated in specific energy intervals.

Although not extraordinary, a FoM of 0.55 ± 0.05 is obtained by considering the whole energy range.

5.4 Summary

In this chapter, the effects of thermal reduction (600-1000 °C) of ZnO powders in H_2-rich atmosphere on optical, structural, morphological and scintillation behavior have been analyzed. The evaluation of reduction degree achieved after the thermal treatment was estimated through EDS analysis and stoichiometry reconstruction, ranging from 0% (TQ_0) to 25% (1000_25). The creation of point defects (Zn interstitials, O vacancies ...) was investigated via ESR spectroscopy, showing that the thermal reduction produces different type of defects as a function of the temperature range. The variation of ZnO cell structure components with introduction of defects reflected on the skeletal density, with decreasing values as a function of the reduction degree.
Secondary effects, such as the morphology and the crystallite size, were evaluated through SEM imaging and XRD, giving consistent results.
The analysis of point defects was correlated with steady-state photoluminescence and radioluminescence measurements, showing an increase of the defective emission intensity along the phosphor series. Such luminescence increase was ascribed to recombination at singly ionized oxygen vacancies or non-ionized oxygen vacancies. Luminescence dynamics measurements highlighted an increase of the fast and slow lifetime that could be attributed to trap states created with the reduction treatment, as also observed via ESR. The optical bandgap, measured through diffuse reflectance, showed a slight contraction from 3.25 eV (TQ_0) to 3.21 eV (1000_25).
After characterization of the phosphors, powders were incorporated in polysiloxane resins with different phenyl content from 0% (PDMS) to 100% (PSS-100). The composite thus obtained were tested under mixed radiation sources. PL and XRL measurements showed different results considering the matrices: PDMS samples showed an increase of PL intensity whereas

PSS matrices a remarked decrease. Therefore, we could conclude that the expected energy transfer from the PSS matrix to the phosphor does not take place, leading to a reduced fluorescence emission.

Alpha and gamma scintillation tests highlighted a proportional light yield with the impinging radiation energy and confirmed the hypothesis of PSD capability for ZnO:Zn phosphors.

Finally, exposure to proton beam (IBIL) resulted in a decrease of the defective emission as a function of the fluence, that could be derived by the formation of trap states on the powder surface and not by matrix damaging. Further investigations with combined IBIL-ESR measurements will be needed to deepen the role of radiation induced defects on the luminescence behavior and to better understand the damaging mechanism. Moreover, a comprehensive study on the pulse shape discrimination capability with optimized samples and parameters will complete the characterization of such phosphors.

Chapter 6

Co-deposition of plasma polymerized *n*-hexane coatings with zinc oxide particles

Part of this section has been published in:

coatings

MDPI

Article

"Thin Films of Plasma-Polymerized n-Hexane and ZnO Nanoparticles Co-Deposited via Atmospheric Pressure Plasma Jet"

M. Favaro, A. Patelli, R. Ceccato, S. Diré, E. Callone, A. Quaranta

Coatings, 2021, 11, 167

In this study, we explore the co-deposition of nanoparticles with concurrent plasma polymerization of a liquid hydrocarbon precursor for possible future application as radiation detectors. The co-deposition of organic/inorganic composite thin films containing luminescent nanoparticles through APPJ technology was achieved by mixing two feeding flows: one was an aerosol solution of zinc oxide nanoparticles in water while the other was a flow of n-hexane vapors. Zinc oxide nanoparticles were produced as standalone by wet chemistry and incorporated through the aerosol buffer solution. The n-hexane hydrocarbon chain was plasma-polymerized (PPH) in a thin film, that resulted to be chemically and thermally stable. In fact, it was subjected to several thermal tests, resulting to be a highly crosslinked network with thermal stability up to $\approx$ 300 °C. The PPH coating was also characterized with NMR, showing a structure rich in unsaturated bonds, with short aliphatic chains and a non-negligible amount of oxidized groups. The coating of zinc oxide nanoparticles with the plasma-polymerized hexane resulted in a remarked increase of the luminescence yield, ascribed to a passivation of the surface defects through polymeric encapsulation.

6.1 Introduction

As previously reported in Section 1.4, zinc oxide is a wide bandgap semiconductor with large free-exciton binding energy (60 meV) resulting in unique and interesting optical and electrical properties. It was widely investigated over the last decades and the application fields range from optoelectronic [25, 162–167] to radiation detection [41, 51, 112, 115, 168, 169] and photocatalysis [170–172].

The embedding of zinc oxide is, therefore, of great interest especially within polymeric matrices that allows for flexibility and low costs. The embedding of zinc oxide in PMMA for the creation of composite materials have been proposed for photo-catalytic and UV protection coating [171, 173–177]. The PMMA matrix is especially interesting from the optical point of view, since PMMA has a superior transparency and a refractive index of $\approx$ 1.49. A complete quench of the visible emission of zinc oxide capped with PMMA was reported by *Wen et al.* [169] and an increase of excitonic emission was confirmed by *Mahamuni et al.* [178] after PVP capping. The passivation of surface defects is fundamental for the optical properties of zinc oxide, as highlighted by *Norberg et al.* [179] that studied the effect of dodecylamine capping on the excitonic emission. A pronounced UV emission can be obtained with capping, because the role of OH groups, that are responsible for the visible luminescence, is blocked.

For photocatalysis, other geometrical and morphological parameters should be taken into account, since the dispersion, shape and size were reported to affect the final behavior [172]. However, to date only a few groups have studied the photocatalytic activity of composite embedding zinc oxide [170, 180].

An extensive application of undoped and doped zinc oxide can be found in the radiation detection field, where different detectors for different radiations were based on zinc oxide [12, 36, 39, 51, 132, 133, 135, 159, 181]. The most promising results come from the doped powder, with Zn, Ga or In dopant [38, 41, 132, 159]. In general, no radiation damage or performance loss were recorded for the zinc oxide [111] but the exposition to a severe radiation environment can induce degradation of the polymeric matrix [15].

Concerning the application of APPJ technology with hydrocarbon precursors for ZnO incorporation in plasma polymers, a few works reported on the use of n-octane and 1,7-octadiene [95, 182–185] with ZnO nanoparticles with conventional AC high voltage APPJ torches working in helium. However, these operating conditions allows for atmopsheric pressure condition but are not sufficient for the generation of cold plasmas. Moreover, the use of expensive helium needs for a more environmentally friendly replacement. n-hexane precursors was selected among the hydrocarbons because of some interesting properties such as conformal coverage [186] and its low surface tension that makes it suitable for vapor feeding. At the best of our knowledge, only a few works reported on the plasma polymerization of n-hexane but with conventional low-pressure plasmas [186–188] and only a single paper on APPJ coupled with an n-hexane electrospray [189]. However, the plasma torch described in *Sohbatzadeh et al.* is not coupled with an RF circuit for the generation of a low-temperature plasma. Moreover, the capping effects on the optical properties of zinc oxide have never been deepened. For this purpose, we decided to study the co-deposition of ZnO nanoparticles with plasma polymerized n-hexane at low temperature with an APPJ torch. The samples were structurally analyzed via FT-IR and with ^{13}C-NMR spectroscopy. The PPH coating was deeply investigated in terms of chemical stability with etching tests and in terms of thermal stability with TGA and DSC analysis. The powder crystallinity was checked with XRD measurements. The effectiveness of plasma polymer incorporation was analyzed via SEM imaging while the passivation via PL measurements.

6.2 Experimental

The realization of co-deposited plasma polymerized hexane films with zinc oxide can be divided in two steps: the chemical synthesis of zinc oxide powder and the plasma deposition of composite films.

The production of the powder started by dissolving 0.2 mol of zinc precursor (zinc acetate dihydrate, $Zn(CH_3COO)_2 \cdot 2H_2O$) in 200 mL of pure ethanol in a flask under magnetic stirring, with the addition of monoethanolamine (C_2H_7NO, 1:1 Zn-amine ratio) to promote the dissolution. The precipitation was obtained with de-ionized water (2:1 water-Zn ratio) and the mixture was filtered with a 3 μm pores filter. The pristine powder was dried overnight in oven at 70 °C, crushed in a mortar and calcinated at 600 °C for 1h in air flow to promote the crystallization.

An initial investigation on the powder was carried throughout FT-IR spectroscopy, SEM imaging and XRD analysis.

The realization of co-deposited films started by dispersing the zinc oxide powder previously obtained and characterized in a water solution (10 mg/ml) using a ultra sonicating tip. The solution was sonicated for 5-10 minutes to obtain an homogeneous dispersion and subsequently placed in a two-neck flask. An aerosol generated with a piezoelectric generator was conveyed to the plasma torch using 0.4 slm of Ar. In parallel, liquid *n*-hexane was bubbled using 0.4 slm of Ar and the two flows were merged before entering in the plasma torch head. The mixture was let to react in the plasma and deposited on a silicon wafer (*p-type*, $8 \div 12\ \Omega \cdot cm$) in controlled conditions with a 3-axis stage. Three different substrate speed between 300 mm/min and 800 mm/min were investigated. The other deposition parameters were: a constant substrate to plasma distance of 6 mm, a deposition area of 10x10 mm^2 and a total amount of layer equal 20. The deposition time ranged between 5 and 10 minutes.

6.3 Results and discussion

6.3.1 Nanoparticle synthesis

At first, the synthesized zinc oxide powder was checked for the quality and crystallinity by SEM and XRD. The results of SEM imaging and XRD analysis are visible in Figure 6.1a and 6.1c. The top-view shows a good nanopowder dimensional dispersion with multifaceted structure, indicative of a good crystallinity. The result is, in fact, confirmed also by XRD analysis, with a spectrum showing the three main peaks of zinc oxide with wide amplitude and different height. The wideness at half maximum (FWHM) is indicative of nano-sized crystallites while the height is indicative of a slight preferential growth along the (101) direction.

The average particle dimension (Figure 6.1a) is 100 $\pm$ 30 nm, while the average crystallite size was calculated to be around 100 $\pm$ 2 nm.

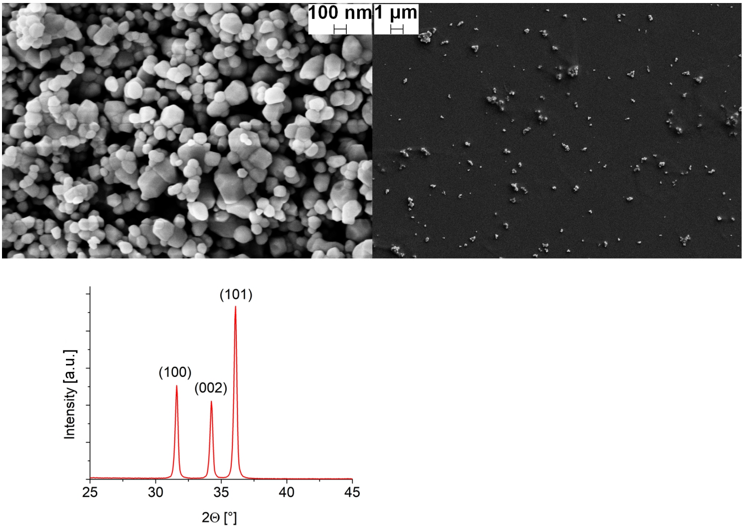

FIGURE 6.1: SEM top-view of the zinc oxide powder (a), surface dispersion of the zinc oxide powder using APPJ technique (b) and XRD spectrum of the zinc oxide powder (c).

The surface dispersion analysis was performed on samples where the dispersion was obtained by flowing an aerosol of zinc oxide powder dispersed in water and sonicated with a sonicating tip for 5 minutes. The plasma torch was fed with the aerosol using argon gas at a constant flow of 0.4 slm. The material was dispersed on a silicon substrate and the process resulted in an homogenous surface dispersion, as visible in Figure 6.1b. The surface area coverage was estimated to be 0.38 $\pm$ 0.02 % of the total area.

The amount of material can be considered low from some points of view, but the reason behind can be related with the high gas flow used to ignite and cool the plasma and a charge effect that favors the dispersion rather than the coating.

The quality of the oxide was also checked through FT-IR analysis (Figure 6.2a) and photoluminescence measurements (Figure 6.2b).

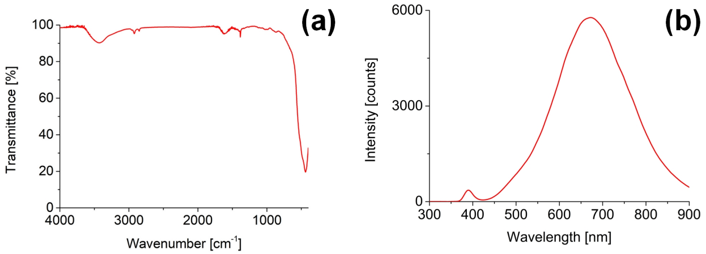

FIGURE 6.2: FT-IR transmittance (a) and PL spectrum (λ_{ex} = 355 nm) of ZnO powder (b).

Figure 6.2a shows the FT-IR spectrum of the powder after thermal treatment. It can be noticed that the main peak at 430 cm^{-1} belongs to Zn-O stretching but other signals are detected. In particular, small peaks at 2960 cm^{-1}, 2850 cm^{-1}, 1460 cm^{-1} and 1380 cm^{-1} confirms the presence of residues of precursor and the two signals at 3400 cm^{-1} and 1615 cm^{-1} the presence of trapped water.

Figure 6.2b shows the powder emission spectrum under 355 nm excitation. It should be noticed that the relative intensity of the NBE and DBE peaks and the center of the DBE band are substantially different from the commercial powder used in Chapter 5. Such differences are due to the different thermal annealing and the powder purity derived from the synthesis technique. In fact, the commercial powder is likely to be obtained by direct high-temperature calcination whereas the laboratory synthesized one was obtained through an organic zinc salt.

6.3.2 Plasma-polymerized *n-hexane*

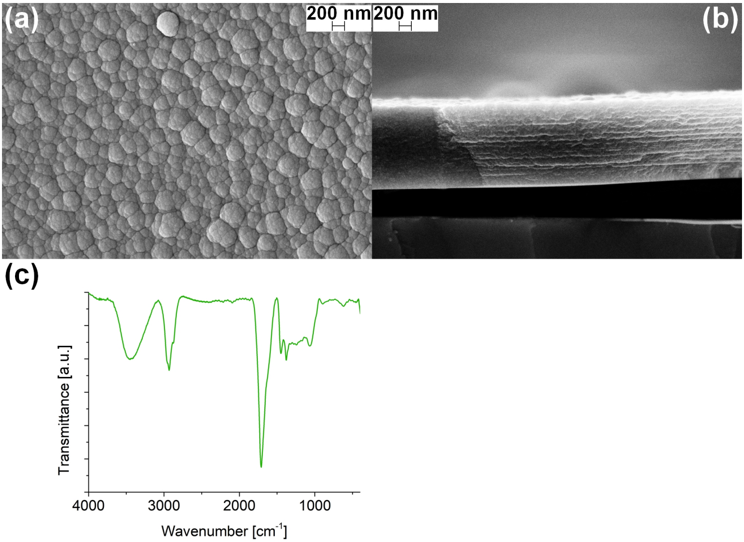

FIGURE 6.3: SEM top-view (a), SEM cross-section (b) and FT-IR spectrum (c) of the plasma-polymerized hexane film.

At first, the surface morphology (Figure 6.3a) was investigate with SEM imaging. The surface shows a bubble-like morphology with apparent pronounced roughness. However, to a deeper investigation, the roughness is not so pronounced (Figure 6.3), so the artifact comes from the image contrast. Anyway, the roughness changes upon the addition of ZnO powder, as clearly visible in Figure 6.8. This change in surface roughness is supposed to be a consequence of the addition of water coming from the aerosol solution of zinc oxide nanoparticles, that induces a change in the contact angle between the precursor and the substrate. Subsequent tests highlighted that the change is not occurring because of water but is related to the ZnO-hexane interaction. It has been reported that the presence of *n*-hexane can influence many zinc oxide properties [190].

The SEM cross-section (Figure 6.3) shows a layered structure as a result of the deposition method. The film thickness is around 650 ± 10 nm with a substrate speed of 300 mm/min, meaning that each single layer is in the order of 32.5 ± 5.0 nm.

The plasma contact time with the substrate plays an important role in the definition of each layer thickness and therefore in the final film thickness. Table 6.1 reports the measured thickness for a constant 20 layer deposition as function of the movement speed and the calculated average instantaneous deposition rate for the hexane precursor.

Substrate speed [mm/min]	**Film thickness [nm]**	**Deposition time [s]**	**Average deposition rate [nm/s]**	**Average volume deposition rate [cm^3/s]**
300	650 ± 10	≈ 640	1	$5 \cdot 10^{-7}$
500	230 ± 10	≈ 380	0.6	$3 \cdot 10^{-7}$
800	150 ± 10	≈ 240	0.6	$3 \cdot 10^{-7}$

TABLE 6.1: Plasma polymerized hexane films parameters measured and calculated.

As previously stated, the plasma contact time plays an important role in the determination of single-layer thickness. However, another important parameter is the conductivity of the substrate, that can change the plasma discharge behavior and lead to a higher monomer fragmentation and an increased recombination rate with respect to insulating substrates [98, 191].

Furthermore, the deposition rate for 500 mm/min and 800 mm/min was experimentally determined to be the same, meaning that a plateau is reached and the fragments recombination is not fully taking place on the substrate but part of the reaction products are lost in the environment. This loss is supposed to be a consequence of the turbulence generated by the torch gas in the proximity of the substrate, since the gas flow is relatively high compared to the nozzle diameter. Additionally, the environment surrounding the plasma torch cannot be assumed to be fully inert, so the presence of oxygen can lead to a partial burn out of the precursor to form water and carbon dioxide.

Figure 6.3c reports the FT-IR spectrum of the PPH sample showing a not well resolved convolution of peaks in the region of CH_3 and CH_2 signals. In particular, the signals lying at 2960 cm^1, 2925 cm^1, 2870 cm^1, 2850 cm^1, 1470 cm^1 and 1380 cm^1 are symmetric and asymmetric stretching vibrations of CH_3 and CH_2 functional groups. Moreover, a strong peak at 1715 cm^1 reveals the presence of unsaturated C=O double bonds associated to carbonyl structures. The complex structure obtained after plasma polymerization is associable with a highly cross-linked matrix and shows excellent chemical stability. A simple dissolution test using the most common solvents was carried out in order to check the plasma action effectiveness. Water, ethanol, acetone, cyclohexane and toluene were selected as suitable solvents and a drop was let to interact for 10-15 minutes. After that, the surface was analysed using an optical microscope but in all cases no visible dissolution was observed. The tests with water and ethanol highlighted that the adhesion between substrate and film is weak and a self-standing film can be obtained.

Finally, the signals lying at 3450 cm^1 and 1640 cm^1 are associated with OH groups derived by atmospheric moisture interaction.

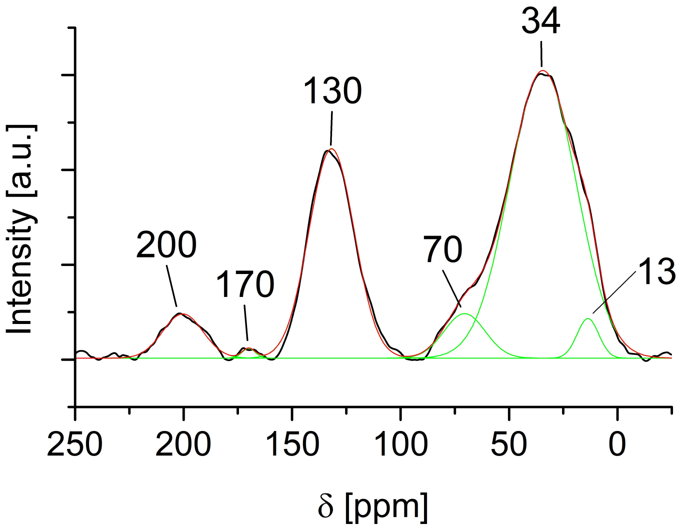

FIGURE 6.4: ^{13}C CP-MAS NMR spectrum of the PPH sample.

The carbon-13 NMR spectrum of a PPH sample is reported in Figure 6.4. Many broad resonance peaks were found, mostly confirming the information found with the FT-IR analysis. The two main resonances are centered at 130 ppm and 33 ppm and are responsible for the presence of double bonds and methylenes respectively. Additionally, minor components can be identified around 200 ppm and 170 ppm associable with ketones and carbonyl functional groups respectively. Moreover, the broad peak at 30 ppm has to be considered as the convolution of signals lying at 10, 30 and 70 ppm respectively, that are associated with methyls, methylenes and ether functional groups.

In order to derive semi-quantitative information from the spectrum, the acquisition parameters were tuned to obtain the maximum intensity of all the resonances. The values derived from this analysis are reported in Table 6.2.

δ [ppm]	Relative amount [%]	Assignment
13	6	$-CH_3$
34	57	$> CH_2$
70	3	$\equiv C-O-C \equiv$
130	30	$\equiv CH$
170	<1	$O-C=O$
200	5	$> C=O$

TABLE 6.2: Assignment of chemical shifts and relative amounts of the main spectral components.

It is worth to underline that the band around 30 ppm, due to broadening, can result from the rise of other components such as ≡CH, that are indicative of branching. In conclusion, the complex network obtained after plasma polymerization is formed by short aliphatic chains with high insaturation degree and oxidized groups derived by a partial plasma interaction with the atmospheric oxygen.

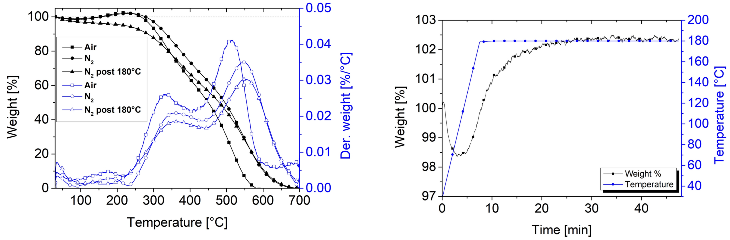

FIGURE 6.5: TGA/DTG thermograms (left) and isothermal treatment (right) on a PPH sample.

Figure 6.5 (left) shows the TGA/DTG thermograms as function of the temperature for a PPH sample. Three different tests were performed because the standard TGA analysis conduced at first revealed some interesting features to be deepened. The first test was performed in standard conditions

(●) under N_2 atmosphere and shows an initial mass loss around 100 °C attributable to the evaporation of water/moisture. An unexpected mass uptake of about 2% at 200 °C was initially attributed to a *buoyancy* effect that is common for low-density samples tested in vertical TGA instruments. However, a deeper investigation revealed that the mass uptake occurs because the nitrogen employed for the test was not fully anhydrous, therefore the saturation of double bonds by oxidation in moisture is favoured. This effect derives from the presence of unsaturated bonds, as previously highlighted by NMR and FT-IR analyses.

This hypothesis is confirmed by the second test that was performed in air (■) and shows a similar trend with initial mass loss followed by a mass gain. However, in this second case the thermal degradation starts at a lower temperature compared to nitrogen conditions.

To deepen the investigation on this unexpected effect, a third test was performed in two steps: an isothermal treatment at 180 °C for 40 minutes in N_2 (Figure 6.5, right), followed by cooling down to room temperature, permanence for 10 minutes and a TGA ramp in N_2 to 700 °C. The graph shows an initial mass loss attributable to water evaporation, followed by a mass uptake that plateaus after 20 minutes. The subsequent TGA thermogram does not show, in fact, the mass uptake, confirming that the isothermal treatment is enough for saturating all the available bonds. Moreover, the mass loss at 100 °C associated with water is still presence, symptom that the residence time in atmosphere is sufficient for letting the moisture interact with the polymer surface. This is not surprising, since the results of FT-IR analysis highlighted that hydrophilic groups are present.

The differential thermogravimetric curves (DTG, Figure 6.5, left) shows that the degradation occurs in two temperature intervals, i.e. 300-450 °C and 450-700 °C, that can likely be associated with side chains and the core chain. The position of DTG peaks in air (□) is shifted to lower values compared to N_2, meaning that the oxidation process carried out in oxygen is more effective than in moisture. However, a deeper investigation with precise moisture fractions in the carrier gas should be performed for a full understand of the phenomenon.

The differential scanning calorimetry (DSC) thermogram is reported in the upper part of Figure 6.6 while the applied temperature profile is shown in the lower part. An initial heating ramp of 20 °C/min is applied from 30 °C to 180 °C, followed by an isothermal treatment at 180 °C for 40 minutes, a controlled cooling at -10 °C/min down to -50 °C and a second heating ramp at 10 °C/min up to 200 °C.

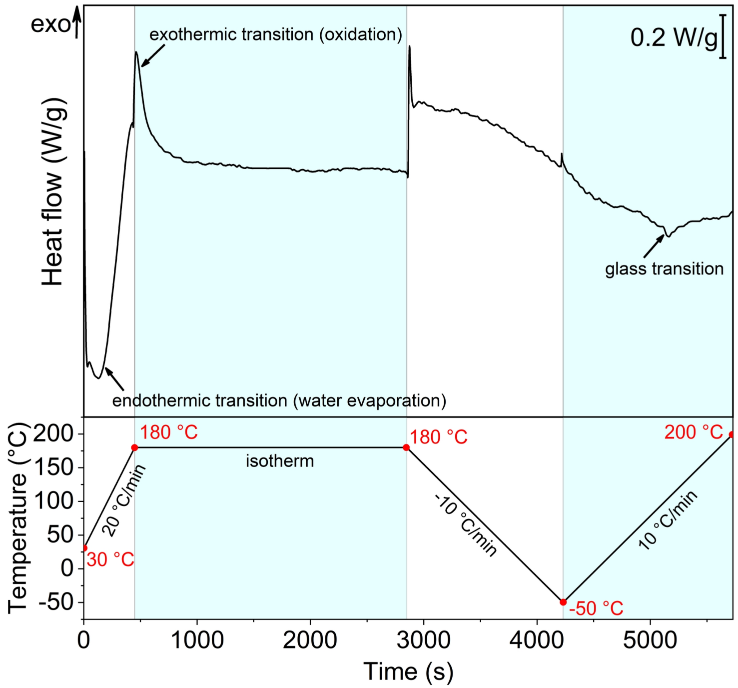

FIGURE 6.6: DSC thermogram (top) and applied profile temperature (bottom).

6.3.3 ZnO/PPH composite

The photoluminescence and photoluminescence dynamics are reported in Figure 6.7a and b respectively. A remarked increase in the intensity of the excitonic emission is followed by a decrease of intensity of the defective emission peak and a shift to lower wavelengths. This considerable increase is likely to be derived by a passivation effect of the surface defects by polymeric encapsulation, as previously reported by other authors [192–196]. In fact, it is well known that surface defects can act as traps for charges, resulting in a quenching of the recombination luminescence and a variation in the recombination dynamics.

The considerable increase in the excitonic emission in the encapsulated sample is obtained even if the encapsulation is not fully attained. The plasma environment is able to create polymer radicals that can effectively passivate the surface of the oxide leading to an improvement of the optical properties. Moreover the PL intensity of the bare powder and of the film is comparable, an greatly lower than that of the passivated powder. This evidence that a high increase of luminescence can be achieved even if the coverage ratio is low.

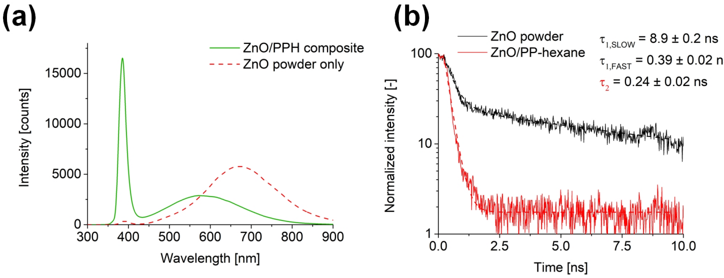

FIGURE 6.7: (a) PL spectrum (λ_{ex}= 355 nm) of the ZnO-PPH compared to the ZnO powder only (red dashed-line); (b) PL decay time (λ_{ex} = 375 nm) of the hybrid ZnO-PPH films.

The shift of the visible broad emission band from bare to passivated sample is ascribed to a double passivation effect that acts on the surface defects and on the presence of hydroxyl groups on the powder surface. In fact, it is well known that the broad defective emission band is a combination of different contributions: oxygen vacancies, oxygen interstitials and OH groups [129, 197]. Moreover, *Zhou et al.* highlighted that OH surface groups can act as quenching centers of the exciton emission [198]. Based on experimental evidences, we can conclude that the plasma co-deposition

process can effectively passivate the particle surface by a thin layer, removing the OH groups previously present. The residual defective band in the passivated sample shows the typical band related to oxygen vacancies in the particle network [27]. However, as evidenced by FT-IR, OH groups are not fully eliminated in the passivated sample, so the plasma action can result in a partial hinder of their role with a loss of trapping efficiency.
The PL dynamics is presented in Figure 6.7b, where the decay kinetics of the excitonic emission is compared. It can be noticed that the initial bi-exponential decay model, fitting the bare powder, is not followed anymore in the passivated sample, which shows a single exponential decay behavior. The initial bi-exponential decay is characterized by τ_s = 8.9 ± 0.2 ns and τ_f = 0.39 ± 0.02 ns, that reduces to tau_f = 0.24 ± 0.02 ns whose real value is limited by the system resolution and the laser pulse width, since it has been reported that pure zinc oxide is characterized by sub-nanosecond transitions [199]. To fully characterize these transitions, we should investigate the kinetics down to such values. However, the fast lifetimes observed for the two samples for excitonic transitions quenched by defects are in good agreement with the literature values [200–202]. The time difference between the two samples is ascribed to a different interaction between the defects and the exciton: in the bare powder the interaction is mainly occurring with surface defects while for the passivated sample with bulk centers. The assignment of the slow component is not straight forward but is likely to be derived by a charge release at surface trapping centers, as previously reported in the literature [128, 203]. A similar component of around 14 ns was observed by *Koida et al.* in pure ZnO crystals and ascribed to trapping effects [151]. The disappearing of the slow component in passivated samples suggests that the trapping mechanism is driven by surface defects, which are also responsible for the exciton luminescence quenching.

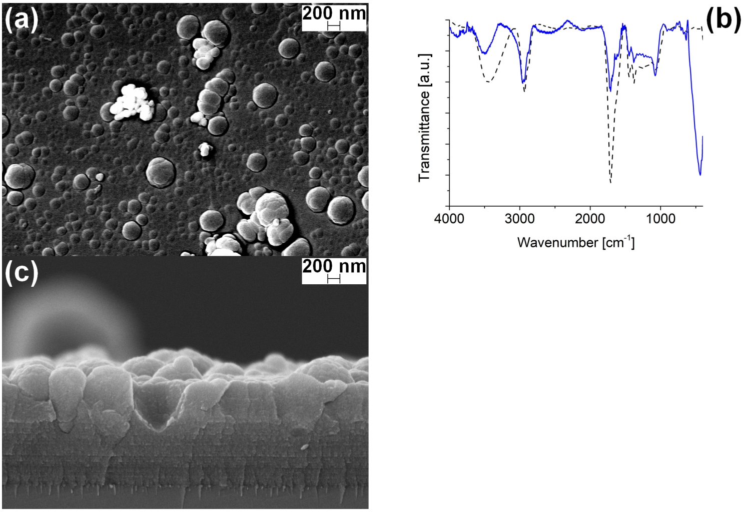

FIGURE 6.8: (a) SEM top-view, (b) FT-IR spectrum, (c) SEM cross-section and of the co-deposited plasma polymerized film with ZnO nanoparticles (300 mm/min).

Figure 6.8a shows the top-view of a co-deposited ZnO/PPH sample obtained with backscattered electron detector (BSD), produced at 300 mm/min. Compared to the hexane only sample, the film shows a cauliflower morphology with several domes of size and density compatible with ZnO aggregates fully covered by polymeric coating. However, the bright spots on the surface are likely to be uncovered or partially covered ZnO aggregates. The film surface, visible in the neighbourhood of the aggregates, appears flatter compared to the hexane only sample.

The morphology change could be ascribed to the concurrent presence of hexane and water in the buffer aerosol solution. However, a dedicated deposition test with just hexane and water but without ZnO particles showed the same structure of the PPH film (Figure 6.3), therefore we can deduce that the dome structure of composite films derives from a zinc oxide-hexane interaction. In fact, it has been pointed out that may zinc oxide properties can be affected by the presence of low surface tension solvents [190].

The SEM cross-section in Figure 6.8c shows a different morphology, supporting this hypothesis. The layered structure derived by subsequent plasma depositions is still visible but mixed with the columnar growth highlighted by the presence of craters and domes with dimension higher than the coating thickness. Even though the presence of zinc oxide particles within the thickness is not visually confirmed by SEM, the columnar growth can be the result of nanoparticles acting as seeds for the growth.

If we consider the domes as partially or fully coated nanoparticles aggregates, the coverage density in composite films is estimated as 0.40 ± 0.02 % of the surface area, being in good agreement with the powder-only sample.

The areal density is a compromise limited by the aerosol technology and the PPH deposition rate. Therefore, the first way to improve the coverage density could be the use of pulsed plasma or the change of the aerosol generator.

Figure 6.8b shows the FT-IR spectrum of ZnO-PPH composite compared to the PPH only (dashed-line). The spectra are in good agreement and the ZnO peak is detected at 430 cm^{-1} [204]. Since the thickness is not exactly the same among the samples, the relative intensity of the peaks varies. The presence of a broad band at 3500 cm^{-1} and of a peak at 1640 cm^{-1} proves the presence of adsorbed water coming either from the nanopowder, the nanopowder dispersing agent or the polymeric film itself coming from environmental moisture uptake, alongside with the presence of trapped OH groups in the ZnO structure.

6.4 Summary

With this work, we studied the co-deposition process of zinc oxide nanoparticles with n-hexane through APPJ technology. ZnO nanoparticles were produced by conventional precipitation method, annealed at 400 °C in oven and characterized before being incorporated in plasma films. On the other hand, liquid hexane was fed as precursor for the deposition of thin polymeric films obtained through plasma polymerization in atmospheric conditions. The resulting films were homogeneous and with complex branched structure that gave good thermal stability. The deposition rate for liquid hexane was evaluated by measuring the thickness at different substrate to plasma deposition speed. The experimental results showed that a plateau is reached for high substrate speeds due to a flow effect. The co-deposition of ZnO-PPH films resulted in a polymeric coating covered with a dispersion of sub-micrometric clusters of ZnO nanoparticles. Due to a limitation of the aerosol technology and the high gas flow involved, the coverage density reached was low; however, a possible solution includes the use of pulsed plasma before a complete change of the aerosol generator. The co-deposited samples showed a considerable increase in the excitonic luminescence yield, ascribed to a powerful passivation of the surface defects through polymeric encapsulation. The effectiveness of the surface passivation is also highlighted by the disappearing of the slow decay component in the exciton recombination dynamics, ascribed to surface trap states.

Chapter 7

Deposition of ZnO nanoparticles and nano-films through APPJ

Part of this section has been published in:

Thin Solid Films 708 (2020) 138118

ELSEVIER

Contents lists available at ScienceDirect

Thin Solid Films

journal homepage: www.elsevier.com/locate/tsf

"Aluminum doped zinc oxide coatings at low temperature by atmospheric pressure plasma jet"
M. Favaro, E. Zanazzi, A. Patelli, S. Carturan, R. Ceccato, V. Mulloni, M. Bortolotti, A. Quaranta
Thin Solid Films, Vol. 728, 31 August 2020, #138118

In this chapter we report on the study and characterization of pure and aluminum doped zinc oxide thin films produced with APPJ technology. Stoichiometrically precise liquid aerosol solutions of zinc acetate and aluminum acetate were fluxed in the plasma torch using an Ar flow and reacted in plasma with ambient air to form zinc oxide and Al-doped zinc oxide. The reacted material was deposited on heated silicon substrates using a controlled-speed 3D stage. Three doping level were achieved by mixing the precursors in well-defined amounts. The samples were chemically, electrically and optically analyzed and compared with spray pyrolysis ones. The role of aluminum as dopant was confirmed by different measurement techniques.

7.1 Introduction

Zinc oxide can be produced with many different techniques, such as sputtering, chemical vapor deposition (CVD), electro deposition and vapor-liquid-solid processes [25].
In the framework of CVD processes, non-equilibrium DC plasmas represents one way to obtain high quality zinc oxide powders, even though the temperatures reached with these processes is in the order of 500 °C, close to conventional techniques such as spray pyrolysis. Despite the superior quality that can be obtained with this families of processes, the main critical point is represented by the processing temperature. In fact, this limit is not easily surmountable, and precludes the possibility to treat heat-sensitive materials, such as daily-use polymers. A way to reduce the processing temperature, and sometimes to lower it to near-atmospheric conditions, is to implement a radio-frequency (RF) circuit in the plasma head, that by the application of a sinusoidal wave, extracts the plasma from a high-voltage and high-temperature generation zone to a processing zone, where the temperature of electrons is much higher than the mean temperature of the ions. In this way, APPJ torches offers the unique possibility to work far below the critical temperature of 100 °C, that represents the upper working limit for the majority of polymeric materials. In this framework, an APPJ torch was used to produce aluminum-doped zinc oxide (AZO) coatings on a silicon substrate with resistivities in the typical range of atomic layer deposition ($10^0 \div 10^{-2}\ \Omega\ X\ cm$) at 250 °C [89, 205, 206]. The limitation of these studies resides in the use of helium as processing gas, the is well-known to be expensive. To overcome this limitation, and to study an effective and sustainable alternative, an argon APPJ torch was used to produce AZO thin films starting from liquid zinc and aluminum acetate water solution precursors. The deposition was obtained on a silicon substrate, heated between 100 and 150 °C. FT-IR and EDS were used to investigate the chemical composition, while SEM imaging for the surface morphology. The structural characterization was obtained through XRD measurements. The optical properties were investigate via PL measurements, and the resistivity of the material as a function of the doping

degree with electrical measurements.

7.2 Experimental

Zinc oxide samples were produced starting from zinc acetate dihydrate ($Zn(CH_3COO)_2$) as base precursor and aluminum acetate dibasic ($C_2H_5O_4Al$) as dopant precursor. Solutions with 5 mM concentration were prepared using bi-distilled water.

The solutions were placed in a 2-neck flask (50 mL) and partially submerged in water to produce an aerosol using an ultrasonic generator. The aerosol was fed into the plasma torch using an argon flow of 0.3 slm. For the generation and cooling of the plasma, 5 slm of argon were fed in the plasma channel and 14 slm of industrial air in the cooling channel. The use of air in the cooling channel grants a constant supply of oxygen nearby the plasma, therefore the oxidation action is effective.

Upon plasma triggering, the HV was turned off, while the RF power was set to 20 W.

A silicon wafer (*p-type, 8÷12Ω cm*) was selected as suitable substrate for the deposition, using a constant velocity of 5 mm/s and an active deposition area of 10x10 mm^2. The plasma to substrate distance was kept constant at 6 mm.

Since the deposition rate of this technique is in the order of $10^{-7}\ cm^3/s$, 20 deposition steps were necessary to obtain a single sample.

The substrate was heated at a constant temperature of 100 °C or 150 °C using a silicon heating bed controlled with an external PID.

The average film thickness was in the range of 1 μm.

Different doping level were achieved by varying the aluminum to zinc ratio in the precursor solution, as reported in Table 7.1. The samples were labeled as PD_Alx_yC or as SP_Alx_yC, were the first characters refer to the production route (PD for plasma deposition and SP for spray pyrolysis), x is the aluminum acetate percentage content and y is the substrate temperature.

Deposition technique	**Al/Zn (precursor)**	**Sample name**
Plasma	0.00	PD_Al0_1X0C
	0.01	PD_Al1_1X0C
	0.05	PD_Al5_1X0C
	0.10	PD_Al10_1X0C
Spray pyrolysis	0.00	SP_Al0_1X0C
	0.01	SP_Al1_1X0C
	0.05	SP_Al5_1X0C
	0.10	SP_Al10_1X0C

TABLE 7.1: Sample labelling as function of the production technique (PD = plasma deposition, SP = spray pyrolysis) and the initial dopant concentration in the precursor solution.

7.3 Results and discussion

7.3.1 XRD analysis

As previously reported (Section 3.7), all the measurements were performed in grazing angle mode (≈ 1 °) with an integration time of 1h. The three main peaks of zinc oxide are lying around 35÷45 ° but the addition of aluminum as dopant gives rise to a peak lying at ≈ 21 °, therefore the spectra are plotted between 20 ° and 60 ° (Figure 7.1,7.2).
For all the samples, the main parameters are listed in Table 7.2.
The PD and SP spectra of the samples produced at 150 °C are reported in Figure 7.1 and 7.2, respectively. The SP samples show a crystalline zinc-oxide based structure with an average grain size of about 15 nm. For both the undoped PD and SP samples a weak texture can be observed with a preferential growth along the (101) direction for the SP and (002) direction for the PD. In general, the deposition technique does not seem to affect the crystallite dimension whereas the presence of Al as dopant does.
Especially for SP samples, the intensity of the peak around 21.5 ° increases significantly with the increase of aluminum acetate precursor content. This peak can be related with the presence of aluminum hydroxide ($Al(OH)_3$) in the structure, as also supposed according to the PL spectra.
For both SP and PD, the addition of dopant result in a shift of the preferential growth orientation toward the (002) direction.

For both samples, the peak around 24.7 ° is due to the silicon substrate.

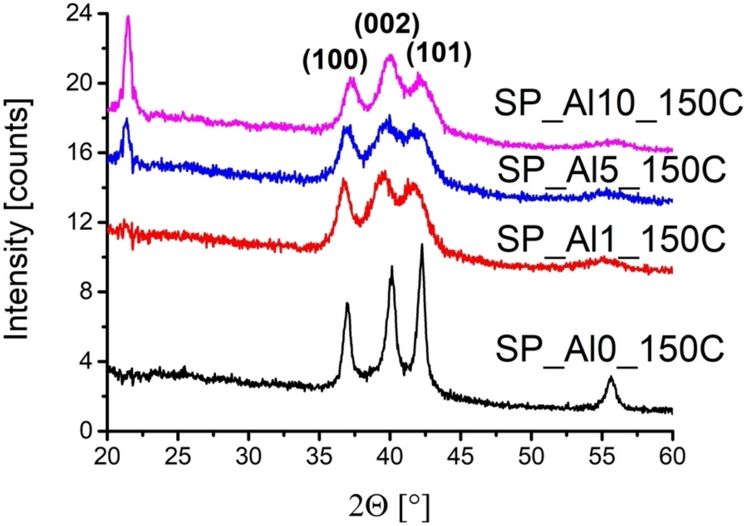

FIGURE 7.1: XRD spectra of the 150 °C samples produced with plasma deposition as function of the dopant amount.

Sample	2θ [°]	Plane family	Crystallite dimension [nm]
PD_Al0_150C	36.70 39.74 41.87	(100) (002) (101)	12.8 ± 0.3
SP_Al0_150C	36.96 40.13 42.26	(100) (002) (101)	18.6 ± 0.3
PD_Al10_150C	36.96 40.10 42.10	(100) (002) (101)	10.5 ± 0.6
SP_Al10_150C	37.19 39.97 42.17	(100) (002) (101)	6.9 ± 0.2

TABLE 7.2: Comparison of the XRD crystallite parameters for undoped and 10% doped PD and SP samples.

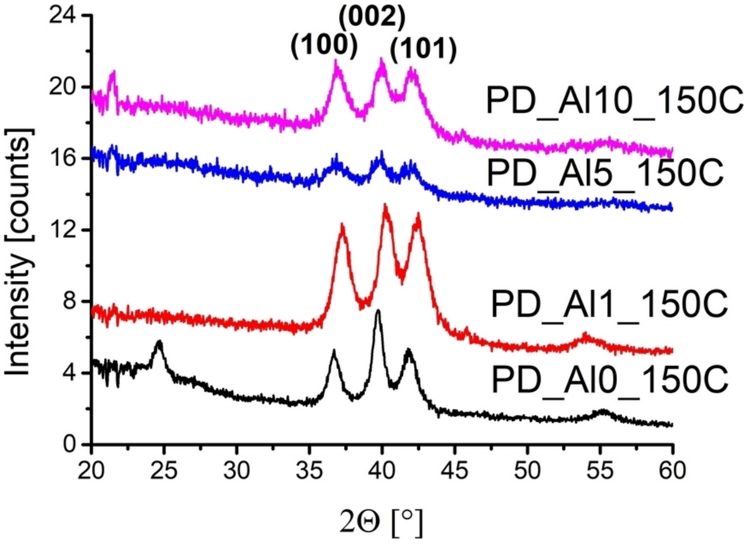

FIGURE 7.2: XRD spectra of the 150 °C samples produced with spray pyrolysis as function of the dopant amount.

The effectiveness of dopant incorporation is also visible from the slight

peaks shifting to higher angles that can be ascribed to the aluminum interaction in the zinc oxide network.
This effectiveness is remarked by a deeper analysis of the crystal cell parameters.
Figure 7.3 shows the variation of the lattice characteristic parameters of zinc oxide as function of the dopant amount for the SP samples, while Figure 7.4 shows the variation for the PD samples. It can be noticed that in both cases the general trend is a decrease in the characteristic *a,c* cell parameters. The values of undoped samples appears to be bigger than that of the literature, probably due to the higher content of defects in the structure. Moreover, the decrease is more noticeable for the PD samples, possibly due to the incorporation of aluminum in the substitutional sites.

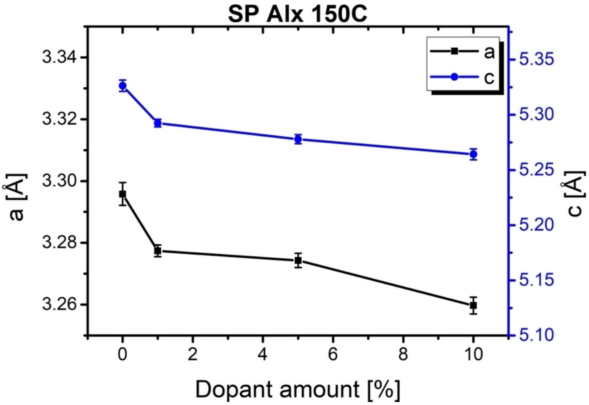

FIGURE 7.3: Lattice parameters variation for the 150 °C samples produced with plasma deposition as function of the dopant amount.

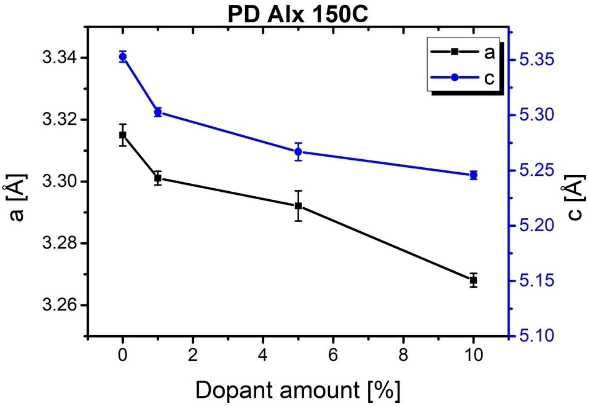

FIGURE 7.4: Lattice parameters variation for the 150 °C samples produced with spray pyrolysis as function of the dopant amount.

7.3.2 FT-IR spectra

The FT-IR spectra of SP and PD samples produced at 100 °C are visible in Figure 7.5 and 7.6 respectively. In can be noticed that for both samples a relatively high amount of organic residues of precursor are present. The two pronounced peaks at 1580 cm^{-1} and 1420 $cm^{-1}$are assigned to the carboxylic group present in the acetate structure. Additionally, the signal at 3300 cm^{-1} shows a massive presence of OH groups, while the signal at 430 cm^{-1} is assigned to the characteristic ZnO stretching. It is clear that, for both techniques, the presence of all these impurities lowers the final quality of the oxide.

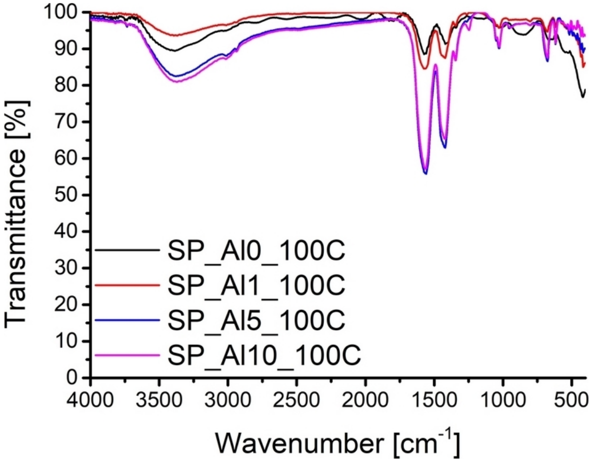

FIGURE 7.5: FT-IR spectra of the plasma deposited samples produced at 100 °C as a function of the dopant amount.

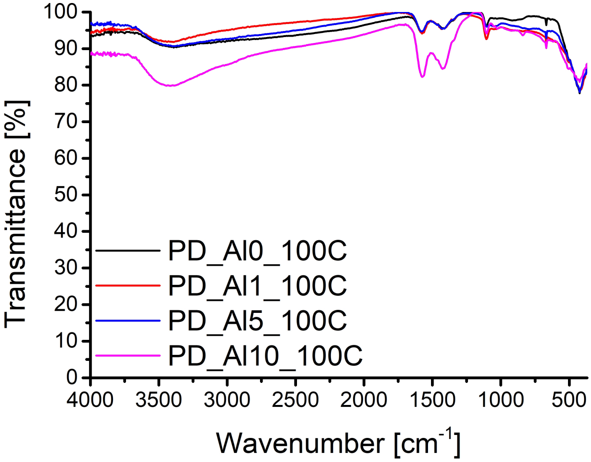

FIGURE 7.6: FT-IR spectra of the spray pyrolysis samples produced at 100 °C as a function of the dopant amount.

Conversely, when the production temperature is raised up to 150 °C, the

final quality improves drastically for PD samples (Figure 7.7), while maintaining almost the same characteristics for the SP samples (Figure 7.8). In fact, the SP samples still show a massive presence of organic residues and water, whereas the PD samples shows a clean single peak spectrum with only the zinc oxide vibration.
The addition of dopant results in an increase of the carboxylic-related signals but does not add any peak since the aluminum oxide has no characteristic peaks in this spectral range.
Considering the temperature effect on the degradation of the acetate group, we can clearly state that no degradation is expected, since the two temperatures are lower than 200 °C.

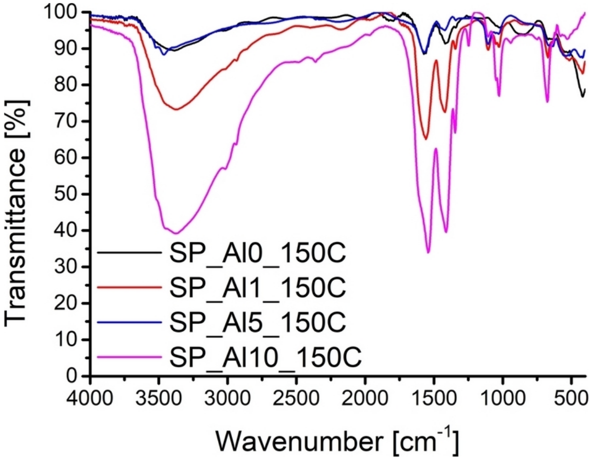

FIGURE 7.7: FT-IR spectra of the plasma deposited samples produced at 150 °C as a function of the dopant amount.

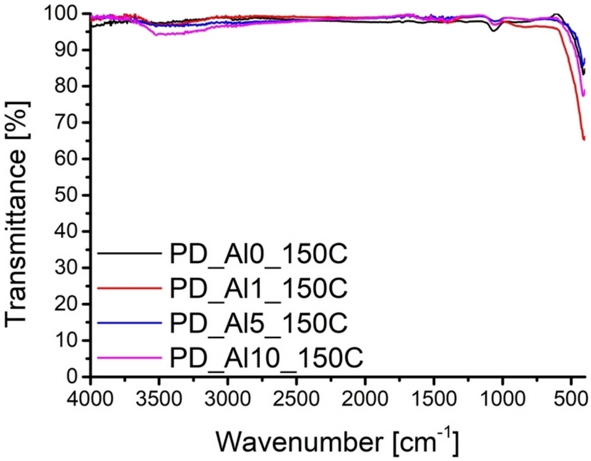

FIGURE 7.8: FT-IR spectra of the spray pyrolysis samples produced at 150 °C as a function of the dopant amount.

7.3.3 SEM/EDS analysis

SEM imaging and EDS analysis were performed separately on two different instruments. For morphological information a FEG source was employed while for EDS analysis a conventional carbon filament was used.

Figure 7.9 and 7.10 shows the top-view of plasma deposited samples at 150 °C for undoped and 10% doped zinc oxide respectively. It can be noticed that the addition of dopant induces a remarked change in the surface morphology, probably related to the presence of an amorphous phase, as also evidenced by the production technique (Figure 7.9 inset).

The morphology suggests that the plasma action is concurrent with a Leidenfrost effect occurring on a droplet of water solution reaching the substrate surface. This effect is well know for spray pyrolysis samples but was never observed in plasma deposition.

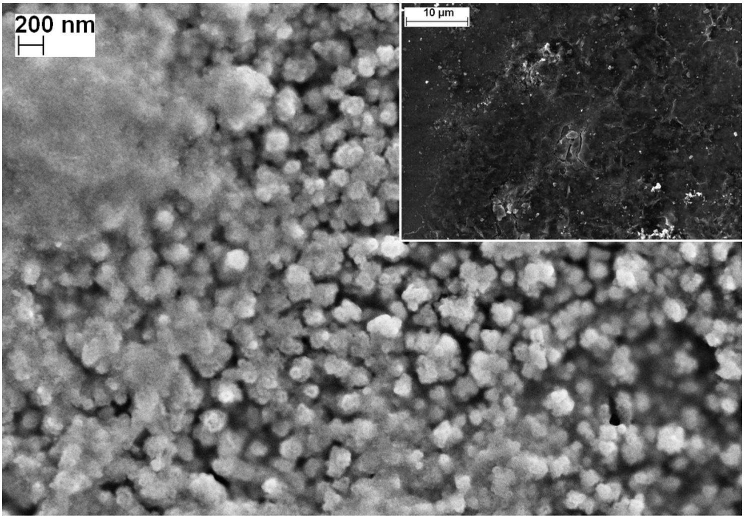

FIGURE 7.9: SEM top-view of the PD_Al0_150C sample (0%); inset: SP_Al0_150C sample.

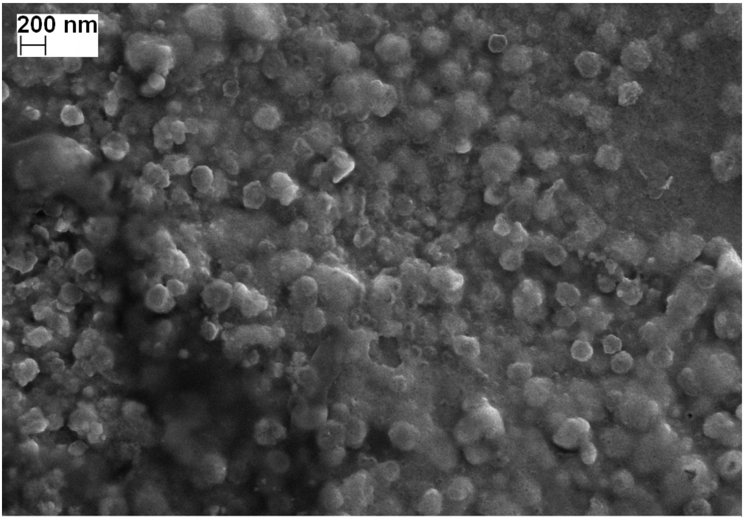

FIGURE 7.10: SEM top-view of the PD_Al10_150C sample (10%).

The films are formed by platelets that results from the formation of a columnar structure, either derived by grains formed in the homogenous phase in the gas flow or by growing on the surface. The lateral platelet dimension is around 100 nm. The layered structure (Figure 7.11) is the result of the consecutive deposition steps of the 3D stage. An average thickness of 1.0 ± 0.2 μm was measured after a raster of 20 steps, therefore a single layer is about 50 nm thick even if the thickness waviness is in the order of several micrometers.

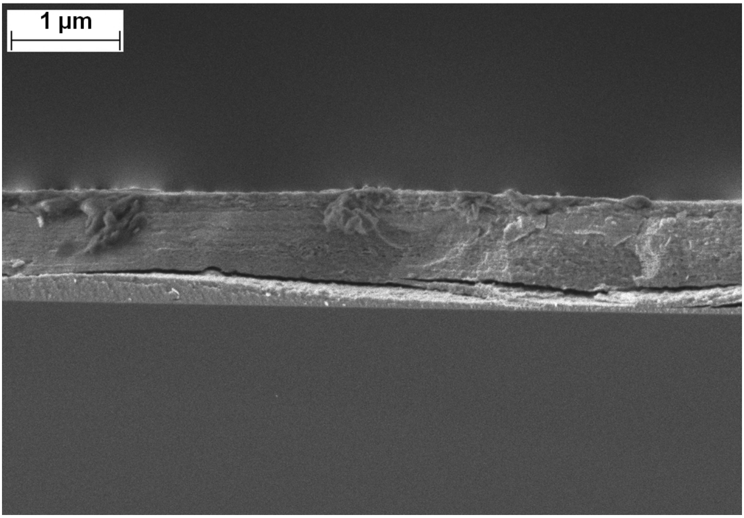

FIGURE 7.11: SEM cross-section of the PD_Al0_150C sample.

7.3.4 PL measurements

Laser-induced photoluminescence of undoped and doped samples was investigated using a λ_{ex} = 355 nm Nd:YAG laser described elsewhere 3.3.1. The spectra of SP samples produced at 150 °C are reported in Figure 7.12. It can be noticed that the excitonic peak at 380 nm is not visible while a broad green band at 580-600 nm is present. This defect-related band shifts to slightly higher wavelengths with the increase in doping and a small feature at 420 nm appears. There are many interpretations of the luminescence of zinc oxide reported in the literature. The defective band centered at high wavelengths (around 600 nm typically) is ascribed to oxygen related defects. In particular interstitial oxygen centers derived by an excess of oxygen shows a pronounced orange emission (sometimes called yellow band). The blue band appearing at 420 nm can be assigned to pyrolitic carbon defects that are formed during the pyrolysis process, as previously observed by *Ortega-Liebana et al.* [207] in luminescent carbon nanodots and in doped structures by *Armitage et al.* [208].

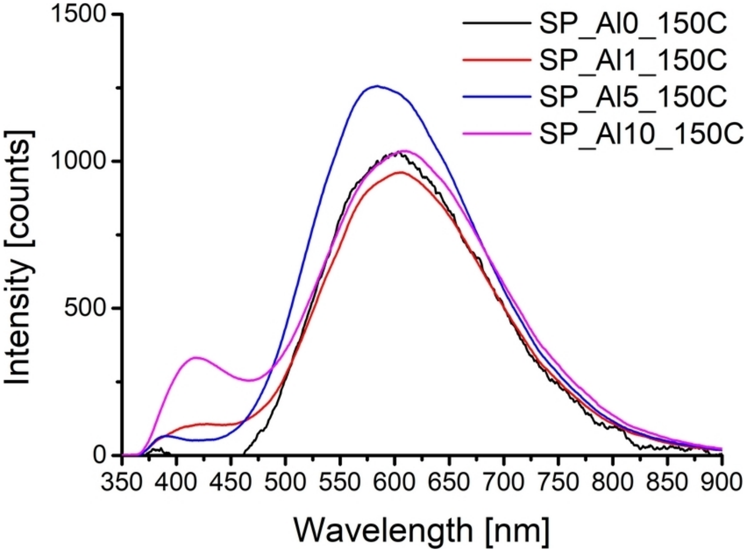

FIGURE 7.12: Laser-induced fluorescence (λ_{ex} = 355 nm) of SP_Alx_150C samples produced at 150 °C by spray pyrolysis.

The spectra of PD samples produced at 150 °C are shown in Figure 7.13 where two main components can be distinguished: a defective emission band at 580 nm and a feature at 450 nm that grows with the dopant addition. This second emission is rarely observed in this AZO systems but, to a deeper analysis, can be ascribed to the formation of non-stoichiometric alumina (Al_2O_{3-x}). This oxygen-deficient component luminescence is related to the presence of alumina F centers; however the presence of alumina has not been clearly proved whereas the presence of aluminum hydroxide was recorded by XRD measurements. The PL of $Al(OH)_3$ under laser excitation is shown in Figure 7.13 inset, where a broad peak centered at 470 nm is visible. Therefore, the hypothesis of a partial aluminum hydroxide contribution in the final emission cannot be completely excluded.

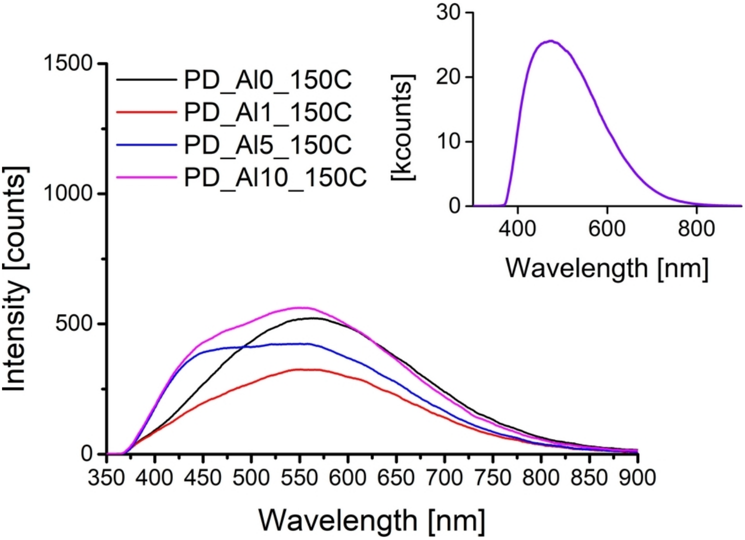

FIGURE 7.13: Laser-induced fluorescence (λ_{ex} = 355 nm) of PD_Alx_150C samples produced at 150 °C by plasma deposition ($Al(OH)_3$ luminescence in the inset).

7.3.5 Electrical measurements

The electrical resistivity of PD_Alx_150C is reported in Figure 7.14 as function of the dopant content. The comparison with SP samples was not possible because of the surface cracks that did not allow for a correct measurement.

It can be noticed that the resistivity, as expected, drops upon addition of dopant up to a 5% content and raises back to the initial values for the 10% content. This effect is well known and related to the trivalent state of aluminum, that acts as n-type dopant in the zinc oxide network. As previously observed by *El Manouni et al.* [209], *Piquè et al.* [210] and *Aktaruzzaman et al.* [211], the dopant amount plays an important role in determining the final electrical properties. Several authors suggest that the excess of aluminum content leads to an increase of defects and traps or to a decrease of crystal dimension with consequent reduction fo the carrier mobility.

The donor effect is therefore present, even though to a deeper analysis the values of electrical resistivity measured are some orders of magnitude higher than that reported in the literature. The role of defects is crucial for the final electron mobility and the combination of electrical and PL measurements suggest that the content of defects is non negligible, since the exciton transition is completely quenched and Al-related defects are present (450 nm emission band).

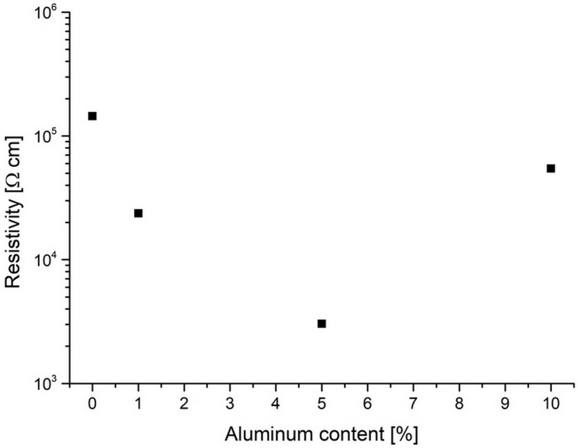

FIGURE 7.14: Electrical resistivity for the PD samples produced at 150 °C (errorbars within the marker).

7.4 Summary

In this work, aluminum doped zinc oxide thin films were deposited by atmospheric pressure plasma deposition on hot substrates to promote the crystallization. The production route evidenced the possibility to obtain homogeneous doped samples at low temperatures (150 °C), opening to several applications were the substrate temperature is fundamental since it is related to the use of polymeric and flexible substrates. A good stoichiometry, close to atomic ratio in solution, was achieved, showing that a key parameter for this technique is easy to control. The comparison with spray pyrolysis samples highlighted that the plasma plays an important role in the decomposition of the organic part for the determination of a final homogeneous oxide. Moreover, the result is achieved through the effectiveness of plasma radical environment rather than a simple heating effect. In fact, the acetate group can easily burn in the atmosphere but only at temperatures higher than 200 °C.

The morphology of plasma deposited AZO films is structured as an assembly of platelets that forms by the impact effect of droplets with the substrate. This effect is due to the high exit speed from the plasma torch and is typical of aerosol buffer solutions formed by droplets. The electrical resistance measurements highlighted that the aluminum ions should be dispersed mainly in the substitutional sites, even if such high values suggests a highly defective structure.

Conclusions and future work

The aim of this thesis was to produce, characterize and study nanostructured materials for flexible detectors in mixed radiation fields. The core study on standalone ZnO:Zn phosphors and nanopowders embedded in polysiloxane for composite flexible scintillators, presented in Chapter 5, highlights the effectiveness of ZnO-based materials for radiation detection. The main advancement, in fact, is represented by the proof of pulse shape discrimination (PSD) capability under combined α and γ exposure of ZnO:Zn phosphors. Although previously hypothesized, it has never been experimentally observed, leaving an open gap that could be finally fulfilled.

Similarly, the systematic correlation of functional properties with the powder reduction degree was partially missing in the literature, making the results proposed in this thesis innovative and original.

To overcome some of the limitations that characterizes traditional detectors, a flexible polymeric matrix (PDMS) with superior optical transparency and high radiation hardness was employed. Nanostructured phosphors (ZnO:Zn) with enhanced green emission were produced and characterized before being incorporated in such matrix. Samples were fully investigated to understand the correlation between reduction degree, obtained upon thermal reduction treatment, and functional properties such as photoluminescence, radioluminescence and scintillation under α, γ and proton excitation.

The most promising samples showed a remarked green luminescence with good light yield under mixed excitation sources making them interesting for the production of dose-sensitive luminescent dosimeters for radio- and proton-therapy.

However, those composite scintillators did not show an appreciable energy transfer between matrix and phosphors, as partially observed previously for the case of organic/inorganic systems based on quantum dots dispersed in polysiloxanes, reported in Chapter 4. In that case a small amount of quantum dots was dispersed in a phenyl-containing polysiloxane matrix to exploit the non-radiative energy transfer between matrix and luminescent nanocrystals. Unfortunately, due to an incompatibility of decay lifetime and the low nanocrystal concentration, poor or absent energy transfer was observed.

Beside the conventional wet chemistry route, another innovative production technique was exploited for the production of nanostructured phosphors. ZnO-based scintillators were synthesized using a novel atmospheric pressure plasma torch (APPJ) working at room temperature conditions in open air.

Undoped and doped ZnO nanofilms were deposited at temperatures much lower than well-consolidated conventional techniques showing comparable or superior functional properties. Tunable doping was easily obtained by varying the chemical ratio of the feeding precursor solutions while the morphology could be tuned by varying the solution concentration.

Additionally, atmospheric plasma was exploited for capping standalone nanopowders via plasma-induced polymerization. The liquid monomer was fed in the plasma together with the phosphors and a capping layer with effective functional properties was deposited.

These studies, reported in Chapter 6 and 7, shows that APPJ is a suitable technique for synthesizing and doping nanopowders, alongside with producing coatings with an effective passivation action. For the first time, a non-conventional polymeric precursor (*n*-hexane) was used to produce a homogeneous coating embedding luminescent nanoparticles that resulted in a luminescence recovery and enhancement.

All these studies enriches the current state of the art on flexible siloxane-based scintillators and atmospheric pressure plasma deposition, highlighting that more efforts are needed to improve the scintillation performance and synthesis conditions. Additional studies to deepen the energy transfer mechanism of siloxane-based matrices and to understand the radiation damaging in ZnO:Zn phosphors are ongoing and will help to fulfill the literature open gap.

References

[1] J. B. Birks and F. W. K. Firk. *The Theory and Practice of Scintillation Counting*. Vol. 18. 8. Pergamon Press, 1965, pp. 60–60. DOI: `10.1063/1.3047620`.

[2] J. C. Lötters et al. "The mechanical properties of the rubber elastic polymer polydimethylsiloxane for sensor applications". In: *Journal of Micromechanics and Microengineering* 7.3 (1997), pp. 145–147. ISSN: 09601317. DOI: `10.1088/0960-1317/7/3/017`.

[3] M. Bowen et al. "A new radiation-resistand plastic scintillator". In: *IEEE Transactions on Nuclear Science* 36.1 (1989), pp. 562–565. URL: `http://library1.nida.ac.th/termpaper6/sd/2554/19755.pdf`.

[4] P. Zygmanski et al. "Low-cost flexible thin-film detector for medical dosimetry applications". In: *Journal of Applied Clinical Medical Physics* 15.2 (2014), pp. 311–326. ISSN: 15269914. DOI: `10.1120/jacmp.v15i2.4454`.

[5] Alberto Quaranta et al. "Optical and scintillation properties of polydimethyldiphenylsiloxane based organic scintillators". In: *IEEE Transactions on Nuclear Science* 57.2 PART 2 (2010), pp. 891–900. ISSN: 00189499. DOI: `10.1109/TNS.2010.2042817`.

[6] A. Quaranta et al. "Characterization of polysiloxane organic scintillators produced with different phenyl containing blends". In: *Materials Chemistry and Physics* 137.3 (2013), pp. 951–958. ISSN: 02540584. DOI: `10.1016/j.matchemphys.2012.10.041`. URL: `http://dx.doi.org/10.1016/j.matchemphys.2012.10.041`.

[7] Laura Basiricò et al. "Direct X-ray photoconversion in flexible organic thin film devices operated below 1 v". In: *Nature Communications* 7 (2016). ISSN: 20411723. DOI: `10.1038/ncomms13063`.

[8] Andrea Ciavatti et al. "Toward Low-Voltage and Bendable X-Ray Direct Detectors Based on Organic Semiconducting Single Crystals". In: *Advanced Materials* 27.44 (2015), pp. 7213–7220. ISSN: 15214095. DOI: `10.1002/adma.201503090`.

[9] Guillaume H. V. Bertrand, Matthieu Hamel, and Fabien Sguerra. “Current Status on Plastic Scintillators Modifications”. In: *Chemistry - A European Journal* 20.48 (2014), pp. 15660–15685. ISSN: 0947-6539. DOI: `10.1002/chem.201404093`.

[10] Martin Nikl. *Nanocomposite, Ceramic, and Thin Film Scintillators*. 2016. ISBN: 9789814745222. DOI: `10.1201/9781315364643`.

[11] S. M. Carturan et al. “Flexible scintillation sensors for the detection of thermal neutrons based on siloxane 6 LiF containing composites: Role of 6 LiF crystals size and dispersion”. In: *Nuclear Instruments and Methods in Physics Research, Section A: Accelerators, Spectrometers, Detectors and Associated Equipment* 925.February (2019), pp. 109–115. ISSN: 01689002. DOI: `10.1016/j.nima.2019.01.088`. URL: `https://doi.org/10.1016/j.nima.2019.01.088`.

[12] Hana Burešová et al. “Preparation and luminescence properties of ZnO:Ga – polystyrene composite scintillator”. In: *Optics Express* 24.14 (2016), p. 15289. ISSN: 1094-4087. DOI: `10.1364/oe.24.015289`.

[13] S. Alamdari, M. Jafar Tafreshi, and M. Sasani Ghamsari. “Preparation and characterization of gallium-doped zinc oxide/polystyrene nanocomposite scintillator for alpha particles detection”. In: *Applied Physics A: Materials Science and Processing* 125.6 (2019), pp. 1–10. ISSN: 14320630. DOI: `10.1007/s00339-019-2727-1`. URL: `https://doi.org/10.1007/s00339-019-2727-1`.

[14] Glenn F. Knoll and H. W. Kraner. *Radiation Detection and Measurement*. John Wiley & Sons, 2010, p. 857. ISBN: 978-0-470-13148-0.

[15] Andrew Karellas and Bruce Thomadsen. *Scintillation Dosimetry*. Ed. by Sam Beddar and Luc Beaulieu. CRC press, 2016, p. 424. ISBN: 978-1-4822-0900-6.

[16] Eljen Technology. *Plastic scintillators*. URL: `https://eljentechnology.com/products/plastic-scintillators`.

[17] Al Rogach. *Semiconductor Nanocrystal Quantum Dots*. 2008. ISBN: 978-3-211-75235-7. DOI: `10.1007/978-3-211-75237-1`. URL: `http://link.springer.com/content/pdf/10.1007/978-3-211-`

`75237-1.pdf{\%}5Cnhttp://link.springer.com/10.1007/978-3-211-75237-1`.

[18] Klaus D. Sattler. *Handbook of Nanophysics: Nanoparticles and Quantum Dots*. Ed. by Klaus D. Sattler. Vol. 53. 9. CRC press, 2013, pp. 1689–1699. ISBN: 9788578110796. DOI: `10.1017/CBO9781107415324.004`. arXiv: `arXiv:1011.1669v3`.

[19] Andrew M. Smith and Shuming Nie. "Semiconductor nanocrystals: Structure, properties, and band gap engineering". In: *Accounts of Chemical Research* 43.2 (2010), pp. 190–200. ISSN: 00014842. DOI: `10.1021/ar9001069`.

[20] S E Létant and T-F Wang. "Semiconductor Quantum Dot Scintillation under γ-Ray Irradiation". In: *Nano Letters* 6.12 (2006), pp. 2877–2880. ISSN: 1530-6984. DOI: `10.1021/nl0620942`. URL: `http://www.ncbi.nlm.nih.gov/pubmed/17163723{\%}5Cnhttp://pubs.acs.org/doi/abs/10.1021/nl0620942`.

[21] Zhitao Kang et al. "CdTe quantum dots and polymer nanocomposites for x-ray scintillation and imaging". In: *Applied Physics Letters* 98.18 (2011), pp. 10–13. ISSN: 00036951. DOI: `10.1063/1.3589366`.

[22] Chris C. Lawrence et al. "Neutron response characterization for an EJ299-33 plastic scintillation detector". In: *Nuclear Instruments and Methods in Physics Research, Section A: Accelerators, Spectrometers, Detectors and Associated Equipment* 759 (2014), pp. 16–22. ISSN: 01689002. DOI: `10.1016/j.nima.2014.04.062`. URL: `http://dx.doi.org/10.1016/j.nima.2014.04.062`.

[23] Ian H. Campbell and Brian K. Crone. "Quantum-dot/organic semiconductor composites for radiation detection". In: *Advanced Materials* 18.1 (2006), pp. 77–79. ISSN: 09359648. DOI: `10.1002/adma.200501434`.

[24] Chao Liu et al. "Transparent Ultra-High-Loading Quantum Dot/Polymer Nanocomposite Monolith for Gamma Scintillation". In: *ACS Nano* 11.6 (2017), pp. 6422–6430. ISSN: 1936086X. DOI: `10.1021/acsnano.7b02923`.

[25] Chennupati Jagadish and Stephen Pearton. *Zinc Oxide Bulk, Thin Films and Nanostructures*. Elsevier Science, 2006, p. 600. ISBN: 9780080447223. DOI: `10.1016/B978-0-08-044722-3.X5000-3`.

[26] Michal A. Borysiewicz. "ZnO as a functional material, a review". In: *Crystals* 9.10 (2019). ISSN: 20734352. DOI: `10.3390/cryst9100505`.

[27] K. Vanheusden et al. "Correlation between photoluminescence and oxygen vacancies in ZnO phosphors". In: *Applied Physics Letters* 403.August 1998 (1995), p. 403. ISSN: 00036951. DOI: `10.1063/1.116699`.

[28] K. Vanheusden et al. "Mechanisms behind green photoluminescence in ZnO phosphor powders". In: *Journal of Applied Physics* 79.10 (1996), pp. 7983–7990. ISSN: 00218979. DOI: `10.1063/1.362349`.

[29] Charlotte Drouilly et al. "ZnO oxygen vacancies formation and filling followed by in situ photoluminescence and in situ EPR". In: *Journal of Physical Chemistry C* 116.40 (2012), pp. 21297–21307. ISSN: 19327447. DOI: `10.1021/jp307693y`.

[30] S. B. Zhang, S. H. Wei, and Alex Zunger. "Intrinsic n-type versus p-type doping asymmetry and the defect physics of ZnO". In: *Physical Review B - Condensed Matter and Materials Physics* 63.7 (2001), pp. 1–7. ISSN: 1550235X. DOI: `10.1103/PhysRevB.63.075205`.

[31] Ü Özgür et al. "A comprehensive review of ZnO materials and devices". In: *Journal of Applied Physics* 98.4 (2005), pp. 1–103. ISSN: 00218979. DOI: `10.1063/1.1992666`.

[32] Dong Jun Yoo et al. "Opto-electrical properties of ZnO:Al powders prepared in a micro drop fluidized reactor". In: *Materials Chemistry and Physics* 183 (2016), pp. 398–404. ISSN: 02540584. DOI: `10.1016/j.matchemphys.2016.08.044`. URL: `http://dx.doi.org/10.1016/j.matchemphys.2016.08.044`.

[33] Anderson Janotti and Chris G. Van De Walle. "Fundamentals of zinc oxide as a semiconductor". In: *Reports on Progress in Physics* 72.12 (2009). ISSN: 00344885. DOI: `10.1088/0034-4885/72/12/126501`. arXiv: `arXiv:1208.5721`.

[34] T. Ivanova et al. "Optical characterization of sol-gel ZnO:Al thin films". In: *Superlattices and Microstructures* 85 (2015), pp. 101–111. ISSN: 10963677. DOI: `10.1016/j.spmi.2015.05.013`.

[35] Linhua Xu et al. "Two different mechanisms on UV emission enhancement in Ag-doped ZnO thin films". In: *Journal of Luminescence* 158 (2015), pp. 396–400. ISSN: 00222313. DOI: `10.1016/j.jlumin.2014.10.028`. URL: `http://dx.doi.org/10.1016/j.jlumin.2014.10.028`.

[36] E. I. Gorokhova et al. "Optical, luminescence, and scintillation properties of ZnO and ZnO:Ga ceramics". In: *Journal of Optical Technology* 75.11 (2008), p. 741. ISSN: 1070-9762. DOI: `10.1364/jot.75.000741`.

[37] Stephen E. Derenzo, Marvin J. Weber, and Mattias K. Klintenberg. "Temperature dependence of the fast, near-band-edge scintillation from CuI, HgI2, PbI2, ZnO:Ga and CdS:In". In: *Nuclear Instruments and Methods in Physics Research, Section A: Accelerators, Spectrometers, Detectors and Associated Equipment* 486.1-2 (2002), pp. 214–219. ISSN: 01689002. DOI: `10.1016/S0168-9002(02)00705-2`.

[38] P. J. Simpson et al. "Superfast timing performance from ZnO scintillators". In: *Nuclear Instruments and Methods in Physics Research, Section A: Accelerators, Spectrometers, Detectors and Associated Equipment* 505.1-2 (2003), pp. 82–84. ISSN: 01689002. DOI: `10.1016/S0168-9002(03)01025-8`.

[39] M. Katagiri et al. "Scintillation materials for neutron imaging detectors". In: *Nuclear Instruments and Methods in Physics Research, Section A: Accelerators, Spectrometers, Detectors and Associated Equipment* 529.1-3 SPEC. ISS. (2004), pp. 274–279. ISSN: 01689002. DOI: `10.1016/j.nima.2004.04.165`.

[40] N. Kubota et al. "Evaluation of ZnS-family phosphors for neutron detectors using photon counting method". In: *Nuclear Instruments and Methods in Physics Research, Section A: Accelerators, Spectrometers, Detectors and Associated Equipment* 529.1-3 SPEC. ISS. (2004), pp. 321–324. ISSN: 01689002. DOI: `10.1016/j.nima.2004.05.004`.

[41] E. D. Bourret-Courchesne, S. E. Derenzo, and M. J. Weber. "Development of ZnO:Ga as an ultra-fast scintillator". In: *Nuclear Instruments and Methods in Physics Research, Section A: Accelerators, Spectrometers, Detectors and Associated Equipment* 601.3 (2009), pp. 358–363. ISSN: 01689002. DOI: `10.1016/j.nima.2008.12.206`.

[42] Liang Chen et al. "The dependence of fluorescent decay time of ZnO:Ga crystal on instantaneous non-equilibrium carriers induced by charged particles". In: *Journal of Luminescence* 214.May (2019), p. 116520. ISSN: 00222313. DOI: `10.1016/j.jlumin.2019.116520`. URL: `https://doi.org/10.1016/j.jlumin.2019.116520`.

[43] J. Pejchal et al. "Luminescence characteristics of the LPE-grown undoped and In-doped ZnO thin films and bulk single crystals". In: *Physica Status Solidi (C) Current Topics in Solid State Physics* 4.3 (2007), pp. 942–945. ISSN: 18626351. DOI: `10.1002/pssc.200673857`.

[44] Takayuki Yanagida et al. "Optical and scintillation properties of bulk ZnO crystal". In: *Physica Status Solidi (C) Current Topics in Solid State Physics* 9.12 (2012), pp. 2284–2287. ISSN: 18626351. DOI: `10.1002/pssc.201200176`.

[45] Masataka Kano et al. "Response-time-improved ZnO scintillator by impurity doping". In: *Journal of Crystal Growth* 318.1 (2011), pp. 788–790. ISSN: 00220248. DOI: `10.1016/j.jcrysgro.2010.10.192`. URL: `http://dx.doi.org/10.1016/j.jcrysgro.2010.10.192`.

[46] M. K. Patra et al. "Studies of luminescence properties of ZnO and ZnO:Zn nanorods prepared by solution growth technique". In: *Journal of Luminescence* 128.2 (2008), pp. 267–272. ISSN: 00222313. DOI: `10.1016/j.jlumin.2007.08.005`.

[47] E. Hasabeldaim et al. "Surface characterization and cathodoluminescence degradation of ZnO thin films". In: *Applied Surface Science* 424 (2017), pp. 412–420. ISSN: 01694332. DOI: `10.1016/j.apsusc.2016.11.178`. URL: `http://dx.doi.org/10.1016/j.apsusc.2016.11.178`.

[48] Yang Zhang, Weifeng Zhang, and Haiwu Zheng. "Fabrication and photoluminescence properties of ZnO:Zn hollow microspheres".

In: *Scripta Materialia* 57.4 (2007), pp. 313–316. ISSN: 13596462. DOI: `10.1016/j.scriptamat.2007.04.028`.

[49] Zhenling Wang et al. "Tunable photoluminescent and cathodoluminescent properties of ZnO and ZnO:Zn phosphors". In: *Journal of Physical Chemistry B* 110.19 (2006), pp. 9469–9476. ISSN: 15206106. DOI: `10.1021/jp057214t`.

[50] Stephen E. Derenzo et al. "Bright and ultra-fast scintillation from a semiconductor?" In: *Nuclear Instruments and Methods in Physics Research, Section A: Accelerators, Spectrometers, Detectors and Associated Equipment* 805 (2016), pp. 36–40. ISSN: 01689002. DOI: `10.1016/j.nima.2015.07.033`. URL: `http://dx.doi.org/10.1016/j.nima.2015.07.033`.

[51] Vladimir A. Demidenko et al. "Scintillation properties of ceramics based on zinc oxide". In: *Radiation Measurements* 42.4-5 (2007), pp. 549–552. ISSN: 13504487. DOI: `10.1016/j.radmeas.2007.01.050`.

[52] R. Li et al. "Incorporation of Luminescent Zinc Oxide Nanoparticles into Polystyrene". In: *MRS Online Proceedings Library* 53.9 (2019), pp. 1689–1699. ISSN: 1098-6596. arXiv: `arXiv:1011.1669v3`.

[53] Fiorenza Fanelli and Francesco Fracassi. "Atmospheric pressure non-equilibrium plasma jet technology: general features, specificities and applications in surface processing of materials". In: *Surface and Coatings Technology* 322 (2017), pp. 174–201. ISSN: 02578972. DOI: `10.1016/j.surfcoat.2017.05.027`. URL: `http://dx.doi.org/10.1016/j.surfcoat.2017.05.027`.

[54] Mounir Laroussi. "Foreword". In: *Plasma Processes and Polymers* 5.6 (2008), pp. 501–502. ISSN: 16128850. DOI: `10.1002/ppap.200800094`.

[55] Th von Woedtke et al. "Plasmas for medicine". In: *Physics Reports* 530.4 (2013), pp. 291–320. ISSN: 03701573. DOI: `10.1016/j.physrep.2013.05.005`. URL: `http://dx.doi.org/10.1016/j.physrep.2013.05.005`.

[56] Davide Mariotti and R. Mohan Sankaran. "Microplasmas for nanomaterials synthesis". In: *Journal of Physics D: Applied Physics* 43.32 (2010). ISSN: 00223727. DOI: `10.1088/0022-3727/43/32/323001`.

[57] T. Belmonte, G. Henrion, and T. Gries. "Nonequilibrium atmospheric plasma deposition". In: *Journal of Thermal Spray Technology* 20.4 (2011), pp. 744–759. ISSN: 10599630. DOI: `10.1007/s11666-011-9642-0`.

[58] Liangliang Lin and Qi Wang. "Microplasma: A New Generation of Technology for Functional Nanomaterial Synthesis". In: *Plasma Chemistry and Plasma Processing* 35.6 (2015), pp. 925–962. ISSN: 02724324. DOI: `10.1007/s11090-015-9640-y`.

[59] T Belmonte et al. "Nanoscience with non-equilibrium plasmas at atmospheric pressure". In: *Journal of Physics D: Applied Physics* 44.36 (2011), p. 363001. ISSN: 0022-3727. DOI: `10.1088/0022-3727/44/36/363001`. URL: `http://stacks.iop.org/0022-3727/44/i=36/a=363001?key=crossref.c5543a8fd60a38ad9fe11a97957c1fd6{\%}5Cnhttp://stacks.iop.org/0022-3727/44/i=36/a=363001`.

[60] T. Belmonte, G. Henrion, and T. Gries. "Nonequilibrium atmospheric plasma deposition". In: *Journal of Thermal Spray Technology* 20.4 (2011), pp. 744–759. ISSN: 10599630. DOI: `10.1007/s11666-011-9642-0`.

[61] Davide Mariotti et al. "Low-Temperature Atmospheric Pressure Plasma Processes for "Green" Third Generation Photovoltaics". In: *Plasma Processes and Polymers* 13.1 (2016), pp. 70–90. ISSN: 16128869. DOI: `10.1002/ppap.201500187`.

[62] X. Lu, M. Laroussi, and V. Puech. "On atmospheric-pressure non-equilibrium plasma jets and plasma bullets". In: *Plasma Sources Science and Technology* 21.3 (2012). ISSN: 09630252. DOI: `10.1088/0963-0252/21/3/034005`.

[63] L. Bárdos and H. Baránková. "Cold atmospheric plasma: Sources, processes, and applications". In: *Thin Solid Films* 518.23 (2010), pp. 6705–6713. ISSN: 00406090. DOI: `10.1016/j.tsf.2010.07.044`. URL: `http://dx.doi.org/10.1016/j.tsf.2010.07.044`.

[64] Johann Laimer and Herbert Störi. "Recent advances in the research on non-equilibrium atmospheric pressure plasma jets". In: *Plasma Processes and Polymers* 4.3 (2007), pp. 266–274. ISSN: 16128850. DOI: `10.1002/ppap.200600114`.

[65] A. Fridman, A. Chirokov, and A. Gutsol. “Non-thermal atmospheric pressure discharges”. In: *Journal of Physics D: Applied Physics* 38.2 (2005). ISSN: 00223727. DOI: `10.1088/0022-3727/38/2/R01`.

[66] Michael Lieberman and Allan Lichtenberg. *Principle of Plasma Discharges and Materials Processing*. John Wiley & Sons, 2005, p. 794. ISBN: 0-471-72001-1.

[67] Yuri P. Raizer. *Gas Discharge Physics.pdf*. 1991.

[68] Francoise Massines et al. “Atmospheric pressure low temperature direct plasma technology: Status and challenges for thin film deposition”. In: *Plasma Processes and Polymers* 9.11-12 (2012), pp. 1041–1073. ISSN: 16128850. DOI: `10.1002/ppap.201200029`.

[69] Alexander Fridman. *Plasma Chemistry*. Cambridge University Press, 2008, p. 1022. ISBN: 978-0-511-39857-5.

[70] J. Winter, R. Brandenburg, and K. D. Weltmann. “Atmospheric pressure plasma jets: An overview of devices and new directions”. In: *Plasma Sources Science and Technology* 24.6 (2015), p. 64001. ISSN: 13616595. DOI: `10.1088/0963-0252/24/6/064001`. URL: `http://dx.doi.org/10.1088/0963-0252/24/6/064001`.

[71] Luisa Stella Dolci et al. “Carboxyl surface functionalization of poly(L -lactic acid) electrospun nanofibers through atmospheric non-thermal plasma affects fibroblast morphology”. In: *Plasma Processes and Polymers* 11.3 (2014), pp. 203–213. ISSN: 16128869. DOI: `10.1002/ppap.201300104`.

[72] Piera Bosso, Fiorenza Fanelli, and Francesco Fracassi. “Deposition of Water-Stable Coatings Containing Carboxylic Acid Groups by Atmospheric Pressure Cold Plasma Jet”. In: *Plasma Processes and Polymers* 13.2 (2016), pp. 217–226. ISSN: 16128869. DOI: `10.1002/ppap.201500005`.

[73] Yui Lun Wu et al. “Electrical and optical characteristics of cylindrical non-thermal atmospheric-pressure dielectric barrier discharge plasma sources”. In: *Surface and Coatings Technology* 234 (2013), pp. 100–103. ISSN: 02578972. DOI: `10.1016/j.surfcoat.2012.09.043`. URL: `http://dx.doi.org/10.1016/j.surfcoat.2012.09.043`.

[74] M. Teschke et al. "High-speed photographs of a dielectric barrier atmospheric pressure plasma jet". In: *IEEE Transactions on Plasma Science* 33.2 I (2005), pp. 310–311. ISSN: 00933813. DOI: `10.1109/TPS.2005.845377`.

[75] Andreas Schütze et al. "The atmospheric-pressure plasma jet: A review and comparison to other plasma sources". In: *IEEE Transactions on Plasma Science* 26.6 (1998), pp. 1685–1694. ISSN: 00933813. DOI: `10.1109/27.747887`.

[76] J. Y. Jeong et al. "Etching materials with an atmospheric-pressure plasma jet". In: *Plasma Sources Science and Technology* 7.3 (1998), pp. 282–285. ISSN: 09630252. DOI: `10.1088/0963-0252/7/3/005`.

[77] J. Y. Jeong et al. "Etching polyimide with a nonequilibrium atmospheric-pressure plasma jet". In: *Journal of Vacuum Science & Technology A: Vacuum, Surfaces, and Films* 17.5 (1999), pp. 2581–2585. ISSN: 0734-2101. DOI: `10.1116/1.581999`.

[78] S. E. Babayan et al. "Deposition of silicon dioxide films with a non-equilibrium atmospheric-pressure plasma jet". In: *Plasma Sources Science and Technology* 10.4 (2001), pp. 573–578. ISSN: 09630252. DOI: `10.1088/0963-0252/10/4/305`.

[79] Damien Thiry et al. "Plasma diagnostics for the low-pressure plasma polymerization process: A critical review". In: *Thin Solid Films* 606 (2016), pp. 19–44. ISSN: 00406090. DOI: `10.1016/j.tsf.2016.02.058`. URL: `http://dx.doi.org/10.1016/j.tsf.2016.02.058`.

[80] Delphine Merche, Nicolas Vandencasteele, and Fran??ois Reniers. "Atmospheric plasmas for thin film deposition: A critical review". In: *Thin Solid Films* 520.13 (2012), pp. 4219–4236. ISSN: 00406090. DOI: `10.1016/j.tsf.2012.01.026`. URL: `http://dx.doi.org/10.1016/j.tsf.2012.01.026`.

[81] H. Yasuda. *Plasma Polymerization*. Elsevier, 1985, p. 432. ISBN: 9780127687605. DOI: `10.1016/C2012-0-01688-2`. URL: `https://linkinghub.elsevier.com/retrieve/pii/C20120016882`.

[82] Don Passey and Geoffrey Eastmond. *New methods of polymer synthesis*. Ed. by J.R. Ebdon and G.C. Eastmond. Vol. 3. 7. 2012, pp. 1677–1679. ISBN: 9789401042680. DOI: `10.1039/c2py90007f`.

[83] D. Gerchman et al. "Thin film deposition by plasma polymerization using D-limonene as a renewable precursor". In: *Progress in Organic Coatings* 129.January (2019), pp. 133–139. ISSN: 03009440. DOI: `10.1016/j.porgcoat.2019.01.018`. URL: `https://doi.org/10.1016/j.porgcoat.2019.01.018`.

[84] R Mohan. *Plasma Processing of Nanomaterials*. CRC press, 2011, p. 432. ISBN: 1439866767. URL: `https://books.google.com/books?id=29ijh1iCxI4C{\&}pgis=1`.

[85] M. Favaro et al. "Aluminum doped zinc oxide coatings at low temperature by atmospheric pressure plasma jet". In: *Thin Solid Films* 708 (2020). ISSN: 00406090. DOI: `10.1016/j.tsf.2020.138118`.

[86] A. Barranco et al. "Plasma-enhanced chemical vapor deposition of SiO2 from a Si(CH3)3Cl precursor and mixtures Ar/O2 as plasma gas". In: *Journal of Vacuum Science & Technology A: Vacuum, Surfaces, and Films* 21.4 (2003), pp. 900–905. ISSN: 0734-2101. DOI: `10.1116/1.1577134`.

[87] C. Jiménez et al. "Deposition of TiO 2 thin films by atmospheric plasma post-discharge assisted injection MOCVD". In: *Surface and Coatings Technology* 201.22-23 SPEC. ISS. (2007), pp. 8971–8975. ISSN: 02578972. DOI: `10.1016/j.surfcoat.2007.04.025`.

[88] L. Soukup et al. "Investigation of the atmospheric RF torch-barrier plasma jet for deposition of CeOx thin films". In: *Surface and Coatings Technology* 169-170 (2003), pp. 571–574. ISSN: 02578972. DOI: `10.1016/S0257-8972(03)00097-5`.

[89] M. D. Barankin et al. "Plasma-enhanced chemical vapor deposition of zinc oxide at atmospheric pressure and low temperature". In: *Solar Energy Materials and Solar Cells* 91.10 (2007), pp. 924–930. ISSN: 09270248. DOI: `10.1016/j.solmat.2007.02.009`.

[90] R. Y. Korotkov et al. "Atmospheric plasma discharge chemical vapor deposition of SnOx thin films using various tin precursors". In: *Thin Solid Films* 516.15 (2008), pp. 4720–4727. ISSN: 00406090. DOI: `10.1016/j.tsf.2007.08.074`.

[91] Robert A. Sailer et al. "Deposition of transparent conductive indium oxide by atmospheric-pressure plasma jet". In: *Surface and*

Coatings Technology 203.5-7 (2008), pp. 835–838. ISSN: 02578972. DOI: `10.1016/j.surfcoat.2008.06.053`. URL: `http://dx.doi.org/10.1016/j.surfcoat.2008.06.053`.

[92] Davide Mariotti and Jenish Patel. "Plasma-liquid interactions at atmospheric pressure for nanomaterials synthesis and surface engineering". In: *Plasma Processes and Polymers* 9.11-12 (2012), pp. 1074–1085. ISSN: 16128850. DOI: `10.1002/ppap.201200007`.

[93] Novriany Amaliyah et al. "Plasma in-liquid method for reduction of zinc oxide in zinc nanoparticle synthesis". In: *Materials Research Express* 2.2 (2015), p. 25004. ISSN: 20531591. DOI: `10.1088/2053-1591/2/2/025004`. URL: `http://dx.doi.org/10.1088/2053-1591/2/2/025004`.

[94] G Zvereva et al. "Plasma–liquid interactions: a review and roadmap". In: *Plasma Sources Science and Technology* 25.5 (2016), p. 053002. DOI: `10.1088/0963-0252/25/5/053002`.

[95] Niall O Connor et al. "Room temperature deposition of tunable plasmonic nanostructures by atmospheric pressure jet plasma". In: *Journal of Materials Chemistry* 22.19 (2012), pp. 9485–9489. ISSN: 09599428. DOI: `10.1039/c2jm30879g`.

[96] M. Favaro et al. "Thin films of plasma-polymerized n-hexane and zno nanoparticles co-deposited via atmospheric pressure plasma jet". In: *Coatings* 11.2 (2021). ISSN: 20796412. DOI: `10.3390/coatings11020167`.

[97] A. Patelli et al. "A customised atmospheric pressure plasma jet for conservation requirements". In: *IOP Conference Series: Materials Science and Engineering* 364.1 (2018). ISSN: 1757899X. DOI: `10.1088/1757-899X/364/1/012079`.

[98] Alessandro Patelli et al. "Nanoroughness, Surface Chemistry, and Drug Delivery Control by Atmospheric Plasma Jet on Implantable Devices". In: *ACS Applied Materials and Interfaces* 10.46 (2018), pp. 39512–39523. ISSN: 19448252. DOI: `10.1021/acsami.8b15886`.

[99] PicoQuant. *PicoHarp 300 User's Manual and Technical Data*.

[100] E. Zanazzi et al. "Real-Time Optical Response of Polysiloxane/Quantum Dot Nanocomposites under 2 MeV Proton Irradiation: Luminescence Enhancement of Polysiloxane Emission through Quantum

Dot Sensitization”. In: *Physica Status Solidi (A) Applications and Materials Science* 217.5 (2020). ISSN: 18626319. DOI: `10.1002/pssa.201900586`.

[101] M. Anni et al. “Förster energy transfer from blue-emitting polymers to colloidal CdSe/ZnS core shell quantum dots”. In: *Applied Physics Letters* 85.18 (2004), pp. 4169–4171. ISSN: 00036951. DOI: `10.1063/1.1814795`.

[102] Aaron R. Clapp et al. “Can luminescent quantum dots be efficient energy acceptors with organic dye donors?” In: *Journal of the American Chemical Society* 127.4 (2005), pp. 1242–1250. ISSN: 00027863. DOI: `10.1021/ja045676z`.

[103] Aaron R. Clapp et al. “Fluorescence Resonance Energy Transfer between Quantum Dot Donors and Dye-Labeled Protein Acceptors”. In: *Journal of the American Chemical Society* 126.1 (2004), pp. 301–310. ISSN: 00027863. DOI: `10.1021/ja037088b`.

[104] Robert Z Stodilka et al. “Optical Degradation of CdSe / ZnS Quantum Dots upon Gamma-Ray Irradiation”. In: *Journal of Physical Chemistry C* 113 (2009), pp. 2580–2585.

[105] Girija Gaur et al. “Influence of Ionizing Radiation and the Role of Thiol Ligands on the Reversible Photodarkening of CdTe/CdS Quantum Dots”. In: *ACS Applied Materials and Interfaces* 8.12 (2016), pp. 7869–7876. ISSN: 19448252. DOI: `10.1021/acsami.5b09657`.

[106] Nathan J. Withers et al. “Rapid degradation of CdSe/ZnS colloidal quantum dots exposed to gamma irradiation”. In: *Applied Physics Letters* 93.17 (2008), pp. 2011–2014. ISSN: 00036951. DOI: `10.1063/1.2978073`.

[107] E. Zanazzi et al. “Photoluminescence enhancement of colloidal CdSe/ZnS quantum dots embedded in polyvinyl alcohol after 2 MeV proton irradiation: crucial role of the embedding medium”. In: *Optical Materials* 88 (2019). ISSN: 09253467. DOI: `10.1016/j.optmat.2018.11.047`.

[108] Joseph R. Lakowicz. *Principles of Fluorescence Spectroscopy Principles of Fluorescence Spectroscopy*. Springer Science+Business Media,

2006, p. 362. ISBN: 978-0-387-31278-1 (Print) 978-0-387-46312-4 (Online). DOI: `10.1007/978-0-387-46312-4`. arXiv: `arXiv:1011.1669v3`.

[109] Tibor Jacob Hajagos et al. “High-Z Sensitized Plastic Scintillators: A Review”. In: *Advanced Materials* 30.27 (2018), pp. 1–13. ISSN: 15214095. DOI: `10.1002/adma.201706956`.

[110] E. Zanazzi et al. “Radiation-induced optical change of ion-irradiated CdSeS/ZnS core-shell quantum dots embedded in polyvinyl alcohol”. In: *Nuclear Instruments and Methods in Physics Research, Section B: Beam Interactions with Materials and Atoms* 435 (2018). ISSN: 0168583X. DOI: `10.1016/j.nimb.2018.05.027`.

[111] Kazuto Koike et al. “Radiation hardness of single-crystalline zinc oxide films”. In: *Physica Status Solidi (C) Current Topics in Solid State Physics* 9.7 (2012), pp. 1577–1579. ISSN: 18626351. DOI: `10.1002/pssc.201100566`.

[112] Melvin John F. Empizo et al. “Photoluminescence properties of a single ZnO microstructure for potential scintillator applications”. In: *Optical Materials* 38 (2014), pp. 256–260. ISSN: 09253467. DOI: `10.1016/j.optmat.2014.10.044`. URL: `http://dx.doi.org/10.1016/j.optmat.2014.10.044`.

[113] Edith D. Bourret-Courchesne, Stephen E. Derenzo, and Marvin J. Weber. “Semiconductor scintillators ZnO and PbI2: Co-doping studies”. In: *Nuclear Instruments and Methods in Physics Research, Section A: Accelerators, Spectrometers, Detectors and Associated Equipment* 579.1 (2007), pp. 1–5. ISSN: 01689002. DOI: `10.1016/j.nima.2007.04.001`.

[114] Yao Wen Hsu et al. “Deposition of zinc oxide thin films by an atmospheric pressure plasma jet”. In: *Thin Solid Films* 519.10 (2011), pp. 3095–3099. ISSN: 00406090. DOI: `10.1016/j.tsf.2010.12.156`. URL: `http://dx.doi.org/10.1016/j.tsf.2010.12.156`.

[115] Yong-Seok Choi et al. “Growth and Characterization of Gallium-Doped ZnO Films for α-Particle Scintillators”. In: *Journal of The Electrochemical Society* 155.11 (2008), H909. ISSN: 00134651. DOI: `10.1149/1.2976885`.

[116] Tadatsugu Minami. “New n -Type TCOs”. In: *MRS Bulletin* 25.08 (2000), pp. 38 –44.

[117] A. Nuruddin and J. R. Abelson. “Improved transparent conductive oxide/p+/i junction in amorphous silicon solar cells by tailored hydrogen flux during growth”. In: *Thin Solid Films* 394.1-2 (2001), pp. 49–63. ISSN: 00406090. DOI: `10.1016/s0040-6090(01)01167-1`.

[118] G. P. Dransfield. “Inorganic sunscreens”. In: *Radiation Protection Dosimetry* 91.1-3 (2000), pp. 271–273. ISSN: 01448420. DOI: `10.1093/oxfordjournals.rpd.a033216`.

[119] M. D. McCluskey and S. J. Jokela. “Defects in ZnO”. In: *Journal of Applied Physics* 106.7 (2009). ISSN: 00218979. DOI: `10.1063/1.3216464`.

[120] X. Zhang et al. “Evidence for high- Tc ferromagnetism in Znx (ZnO) 1-x granular films mediated by native point defects”. In: *Physical Review B - Condensed Matter and Materials Physics* 80.17 (2009), pp. 2–7. ISSN: 10980121. DOI: `10.1103/PhysRevB.80.174427`.

[121] J. B. Yi et al. “Ferromagnetism in dilute magnetic semiconductors through defect engineering: Li-doped ZnO”. In: *Physical Review Letters* 104.13 (2010), pp. 1–4. ISSN: 00319007. DOI: `10.1103/PhysRevLett.104.137201`.

[122] M. Khalid et al. “Defect-induced magnetic order in pure ZnO films”. In: *Physical Review B - Condensed Matter and Materials Physics* 80.3 (2009), pp. 1–5. ISSN: 10980121. DOI: `10.1103/PhysRevB.80.035331`.

[123] Guozhong Xing et al. “Correlated d0 ferromagnetism and photoluminescence in undoped ZnO nanowires”. In: *Applied Physics Letters* 96.11 (2010), pp. 1–4. ISSN: 00036951. DOI: `10.1063/1.3340930`.

[124] J. V. Foreman et al. “Effects of reabsorption and spatial trap distributions on the radiative quantum efficiencies of ZnO”. In: *Physical Review B - Condensed Matter and Materials Physics* 81.11 (2010), pp. 1–10. ISSN: 10980121. DOI: `10.1103/PhysRevB.81.115318`.

[125] S. A.M. Lima et al. “Luminescent properties and lattice defects correlation on zinc oxide”. In: *International Journal of Inorganic Materials* 3.7 (2001), pp. 749–754. ISSN: 14666049. DOI: `10.1016/S1466-6049(01)00055-1`.

[126] John S. Neal et al. “Evaluation of melt-grown, ZnO single crystals for use as alpha-particle detectors”. In: *IEEE Transactions on Nuclear Science* 55.3 (2008), pp. 1397–1403. ISSN: 00189499. DOI: `10.1109/TNS.2008.922829`.

[127] Z.Y Xue et al. “The blue photoluminescence emitted from ZnO films deposited on glass substrate by rf magnetron sputtering”. In: *Applied Surface Science* 195.1-4 (2002), pp. 126–129. ISSN: 01694332. DOI: `10.1016/s0169-4332(02)00547-0`.

[128] Yusuke Furukawa et al. “Temperature dependence of scintillation properties for a hydrothermal-method-grown zinc oxide crystal evaluated by nickel-like silver laser pulses”. In: *Journal of the Optical Society of America B* 25.7 (2008), B118. ISSN: 0740-3224. DOI: `10.1364/josab.25.00b118`.

[129] A. B. Djurišić et al. “Defect emissions in ZnO nanostructures”. In: *Nanotechnology* 18.9 (2007). ISSN: 09574484. DOI: `10.1088/0957-4484/18/9/095702`.

[130] Fushan Wen et al. “Hydrothermal synthesis of ZnO:Zn with green emission at low temperature with reduction process”. In: *Solid State Communications* 135.1-2 (2005), pp. 34–37. ISSN: 00381098. DOI: `10.1016/j.ssc.2005.03.066`.

[131] A. Wagner et al. “ZnO Luminescence and scintillation studied via photoexcitation, X-ray excitation and gamma-induced positron spectroscopy”. In: *Scientific Reports* 6.1 (2016), pp. 1–9. DOI: `10.1038/srep31238`.

[132] J. S. Neal et al. “Comparative investigation of the performance of ZnO-based scintillators for use as α-particle detectors”. In: *Nuclear Instruments and Methods in Physics Research, Section A: Accelerators, Spectrometers, Detectors and Associated Equipment* 568.2 (2006), pp. 803–809. ISSN: 01689002. DOI: `10.1016/j.nima.2006.09.041`.

[133] P. A. Rodnyi et al. “Novel scintillation materialzno transparent ceramics”. In: *IEEE Transactions on Nuclear Science* 59.5 PART 2 (2012), pp. 2152–2155. ISSN: 00189499. DOI: `10.1109/TNS.2012.2189896`.

[134] Yu Yi Chen and Jia Yang Juang. “Enhancement of Ga-doped zinc oxide film properties and deposition rate by multiple deposition

using atmosphere pressure plasma jet". In: *Journal of Alloys and Compounds* 694 (2017), pp. 452–458. ISSN: 09258388. DOI: `10.1016/j.jallcom.2016.09.320`. URL: `http://dx.doi.org/10.1016/j.jallcom.2016.09.320`.

[135] Takayuki Yanagida et al. "Scintillation properties of in doped ZnO with different in concentrations". In: *IEEE Transactions on Nuclear Science* 57.3 PART 2 (2010), pp. 1325–1328. ISSN: 00189499. DOI: `10.1109/TNS.2009.2035120`.

[136] Takayuki Yanagida et al. "Scintillation properties of in doped ZnO with different in concentrations". In: *IEEE Transactions on Nuclear Science* 57.3 PART 2 (2010), pp. 1325–1328. ISSN: 00189499. DOI: `10.1109/TNS.2009.2035120`.

[137] Liang Chen et al. *Comparative study on fluorescence decay time of doped ZnO crystals under α and β excitation*. 2019. DOI: `10.1016/j.nima.2019.04.095`.

[138] Lídia Santos et al. "WO3 nanoparticle-based conformable pH sensor". In: *ACS Applied Materials and Interfaces* 6.15 (2014), pp. 12226–12234. ISSN: 19448252. DOI: `10.1021/am501724h`.

[139] G. Jeff Sykora, Erik M. Schooneveld, and Nigel J. Rhodes. "ZnO:Zn/6LiF scintillator—A low afterglow alternative to ZnS:Ag/6LiF for thermal neutron detection". In: *Nuclear Instruments and Methods in Physics Research, Section A: Accelerators, Spectrometers, Detectors and Associated Equipment* 883.November 2017 (2018), pp. 75–82. ISSN: 01689002. DOI: `10.1016/j.nima.2017.11.052`.

[140] E. D. Bourret-Courchesne, S. E. Derenzo, and M. J. Weber. "Development of ZnO:Ga as an ultra-fast scintillator". In: *Nuclear Instruments and Methods in Physics Research, Section A: Accelerators, Spectrometers, Detectors and Associated Equipment* 601.3 (2009), pp. 358–363. ISSN: 01689002. DOI: `10.1016/j.nima.2008.12.206`.

[141] Qiuping Zhang et al. "Oxygen vacancy-mediated ZnO nanoparticle photocatalyst for degradation of methylene blue". In: *Applied Sciences (Switzerland)* 8.3 (2018), pp. 1–12. ISSN: 20763417. DOI: `10.3390/app8030353`.

[142] L. A. Kappers et al. “EPR and optical study of oxygen and zinc vacancies in electron-irradiated ZnO”. In: *Nuclear Instruments and Methods in Physics Research, Section B: Beam Interactions with Materials and Atoms* 266.12-13 (2008), pp. 2953–2957. ISSN: 0168583X. DOI: `10.1016/j.nimb.2008.03.146`.

[143] Hülya Kaftelen et al. “EPR and photoluminescence spectroscopy studies on the defect structure of ZnO nanocrystals”. In: *Physical Review B - Condensed Matter and Materials Physics* 86.1 (2012), pp. 1–9. ISSN: 10980121. DOI: `10.1103/PhysRevB.86.014113`.

[144] Joydip Sengupta et al. “Influence of annealing temperature on the structural, topographical and optical properties of sol-gel derived ZnO thin films”. In: *Materials Letters* 65.17-18 (2011), pp. 2572–2574. ISSN: 0167577X. DOI: `10.1016/j.matlet.2011.06.021`.

[145] B. D. CULLITY. “X-Ray Diffraction Addison-Wesley Metallurgy Series”. In: *Journal of Chemical Information and Modeling* 53 (1956), pp. 1689–1699. ISSN: 1098-6596. arXiv: `arXiv:1011.1669v3`.

[146] Jun Kue Park et al. “Dynamical Properties of Hydrogen in ZnO : H Treated by H 2 / Ar Plasma under Atmospheric Pressure”. In: (2015), pp. 7–8.

[147] Haibo Zeng et al. “Blue luminescence of ZnO nanoparticles based on non-equilibrium processes: Defect origins and emission controls”. In: *Advanced Functional Materials* 20.4 (2010), pp. 561–572. ISSN: 1616301X. DOI: `10.1002/adfm.200901884`.

[148] Anderson Janotti and Chris G. Van De Walle. “Native point defects in ZnO”. In: *Physical Review B - Condensed Matter and Materials Physics* 76.16 (2007), pp. 1–22. ISSN: 10980121. DOI: `10.1103/PhysRevB.76.165202`.

[149] Jinpeng Lv and Xingji Li. “Defect evolution in ZnO and its effect on radiation tolerance”. In: *Physical Chemistry Chemical Physics* 20.17 (2018), pp. 11882–11887. ISSN: 14639076. DOI: `10.1039/c8cp01855c`.

[150] A. Jagannatha Reddy et al. “EPR, thermo and photoluminescence properties of ZnO nanopowders”. In: *Spectrochimica Acta - Part A: Molecular and Biomolecular Spectroscopy* 81.1 (2011), pp. 59–63. ISSN:

13861425. DOI: `10.1016/j.saa.2011.06.048`. URL: `http://dx.doi.org/10.1016/j.saa.2011.06.048`.

[151] T. Koida et al. "Correlation between the photoluminescence lifetime and defect density in bulk and epitaxial ZnO". In: *Applied Physics Letters* 82.4 (2003), pp. 532–534. ISSN: 00036951. DOI: `10.1063/1.1540220`.

[152] Arunasish Layek, Biswajit Manna, and Arindam Chowdhury. "Carrier recombination dynamics through defect states of ZnO nanocrystals: From nanoparticles to nanorods". In: *Chemical Physics Letters* 539-540 (2012), pp. 133–138. ISSN: 00092614. DOI: `10.1016/j.cplett.2012.05.028`. URL: `http://dx.doi.org/10.1016/j.cplett.2012.05.028`.

[153] Takahiro Matsumoto et al. "Correlation between grain size and optical properties in zinc oxide thin films". In: *Applied Physics Letters* 81.7 (2002), pp. 1231–1233. ISSN: 00036951. DOI: `10.1063/1.1499991`.

[154] Patrycja Makuła, Michał Pacia, and Wojciech Macyk. "How To Correctly Determine the Band Gap Energy of Modified Semiconductor Photocatalysts Based on UV-Vis Spectra". In: *Journal of Physical Chemistry Letters* 9.23 (2018), pp. 6814–6817. ISSN: 19487185. DOI: `10.1021/acs.jpclett.8b02892`.

[155] T. Makino et al. "Band gap engineering based on MgxZn1-xO and CdyZn1-yO ternary alloy films". In: *Applied Physics Letters* 78.9 (2001), pp. 1237–1239. ISSN: 00036951. DOI: `10.1063/1.1350632`.

[156] P. A. Rodnyi and I. V. Khodyuk. "Optical and luminescence properties of zinc oxide (Review)". In: *Optics and Spectroscopy (English translation of Optika i Spektroskopiya)* 111.5 (2011), pp. 776–785. ISSN: 0030400X. DOI: `10.1134/S0030400X11120216`.

[157] Ruijin Hong et al. "ZnO:Zn phosphor thin films prepared by face-to-face annealing". In: *Journal of Crystal Growth* 284.3-4 (2005), pp. 347–352. ISSN: 00220248. DOI: `10.1016/j.jcrysgro.2005.07.029`.

[158] P. Rodnyi et al. "Influence of annealing on the scintillation properties of zinc oxide powders and ceramics". In: *Radiation Measurements* 90 (2016), pp. 136–139. ISSN: 13504487. DOI: `10.1016/j.`

radmeas.2016.01.021. URL: `http://dx.doi.org/10.1016/j.radmeas.2016.01.021`.

[159] John S. Neal et al. “Investigation of ZnO-based polycrystalline ceramic scintillators for use as α -particle detectors”. In: *IEEE Transactions on Nuclear Science* 56.3 (2009), pp. 892–898. ISSN: 00189499. DOI: `10.1109/TNS.2008.2004702`.

[160] E. Zanazzi et al. ”Proton Irradiation Effects on Colloidal InGaP/ZnS Core-Shell Quantum Dots Embedded in Polydimethylsiloxane: Discriminating Core from Shell Radiation-Induced Defects through Time-Resolved Photoluminescence Analysis”. In: *Journal of Physical Chemistry C* 122.38 (2018). ISSN: 19327455. DOI: `10.1021/acs.jpcc.8b06181`.

[161] K. Bandopadhyay and J. Mitra. “Zn interstitials and O vacancies responsible for n-type ZnO: what do the emission spectra reveal?” In: *RSC Advances* 5.30 (2015), pp. 23540–23547. ISSN: 20462069. DOI: `10.1039/c5ra00355e`. URL: `http://dx.doi.org/10.1039/C5RA00355E`.

[162] D. G. Thomas. “The exciton spectrum of zinc oxide”. In: *Journal of Physics and Chemistry of Solids* 15.1-2 (1960), pp. 86–96. ISSN: 00223697. DOI: `10.1016/0022-3697(60)90104-9`.

[163] A. Mang, K. Reimann, and St Rübenacke. “Band gaps, crystal-field splitting, spin-orbit coupling, and exciton binding energies in ZnO under hydrostatic pressure”. In: *Solid State Communications* 94.4 (1995), pp. 251–254. ISSN: 00381098. DOI: `10.1016/0038-1098(95)00054-2`.

[164] G. Cantwell, W. C. Harsch, and B. Jogai. “Valence-band ordering in zno”. In: *Physical Review B - Condensed Matter and Materials Physics* 60.4 (1999), pp. 2340–2344. ISSN: 1550235X. DOI: `10.1103/PhysRevB.60.2340`.

[165] Yefan Chen et al. “Plasma assisted molecular beam epitaxy of ZnO on c-plane sapphire: Growth and characterization”. In: *Journal of Applied Physics* 84.7 (1998), pp. 3912–3918. ISSN: 00218979. DOI: `10.1063/1.368595`.

[166] M. Sasani Ghamsari et al. “ZnO nanocrystals with narrow-band blue emission”. In: *Journal of Luminescence* 205.September 2018 (2019), pp. 508–518. ISSN: 00222313. DOI: `10.1016/j.jlumin.2018.09.064`. URL: `https://doi.org/10.1016/j.jlumin.2018.09.064`.

[167] Zhong Lin Wang. “Zinc oxide nanostructures: growth, properties and applications”. In: *Journal of Physics: Condensed Matter* 16.25 (2004), R829–R858. ISSN: 0953-8984. DOI: `10.1088/0953-8984/16/25/R01`. URL: `http://stacks.iop.org/0953-8984/16/i=25/a=R01?key=crossref.79a64bb3c5533760ca9ff098c9a46a8a`.

[168] Yutaka Fujimoto et al. “Scintillation characteristic of in,Ga-Doped ZnO thin films with different dopant concentrations”. In: *Japanese Journal of Applied Physics* 50.1 PART 3 (2011). ISSN: 00214922. DOI: `10.1143/JJAP.50.01BG04`.

[169] Xin Wen, Qingmin Zhang, and Zhuang Shao. “Magnetron sputtering for ZnO:Ga scintillation film production and its application research status in nuclear detection”. In: *Crystals* 9.5 (2019), pp. 1–23. ISSN: 20734352. DOI: `10.3390/cryst9050263`.

[170] Alessandro Di Mauro et al. “ZnO for application in photocatalysis: From thin films to nanostructures”. In: *Materials Science in Semiconductor Processing* 69.March (2017), pp. 44–51. ISSN: 13698001. DOI: `10.1016/j.mssp.2017.03.029`.

[171] Alessandro Di Mauro et al. “Novel synthesis of ZnO/PMMA nanocomposites for photocatalytic applications”. In: *Scientific Reports* 7.January (2017), pp. 1–12. ISSN: 20452322. DOI: `10.1038/srep40895`. URL: `http://dx.doi.org/10.1038/srep40895`.

[172] T.C. Bharat et al. “Synthesis of Doped Zinc Oxide Nanoparticles: A Review”. In: *Materials Today: Proceedings* 11 (2019), pp. 767–775. ISSN: 22147853. DOI: `10.1016/j.matpr.2019.03.041`. URL: `https://linkinghub.elsevier.com/retrieve/pii/S2214785319303840`.

[173] Xi Wen Du et al. “Complete UV emission of ZnO nanoparticles in a PMMA matrix”. In: *Semiconductor Science and Technology* 21.8 (2006), pp. 1202–1206. ISSN: 02681242. DOI: `10.1088/0268-1242/21/8/037`.

[174] R. Y. Hong, J. Z. Qian, and J. X. Cao. "Synthesis and characterization of PMMA grafted ZnO nanoparticles". In: *Powder Technology* 163.3 (2006), pp. 160–168. ISSN: 00325910. DOI: `10.1016/j.powtec.2006.01.015`.

[175] B. Kulyk et al. "Optical properties of ZnO/PMMA nanocomposite films". In: *Journal of Alloys and Compounds* 502.1 (2010), pp. 24–27. ISSN: 09258388. DOI: `10.1016/j.jallcom.2010.04.162`. URL: `http://dx.doi.org/10.1016/j.jallcom.2010.04.162`.

[176] Haider Mohammed Shanshoof et al. "Polymer-ZnO nanocomposites foils and thin films for UV protection". In: *AIP Conference Proceedings* 1614.February (2014), pp. 136–141. ISSN: 15517616. DOI: `10.1063/1.4895185`.

[177] Erjun Tang, Guoxiang Cheng, and Xiaolu Ma. "Preparation of nano-ZnO/PMMA composite particles via grafting of the copolymer onto the surface of zinc oxide nanoparticles". In: *Powder Technology* 161.3 (2006), pp. 209–214. ISSN: 00325910. DOI: `10.1016/j.powtec.2005.10.007`.

[178] S Mahamumi et al. "ZnO Nanoparticles Embedded in Polymeric Matrices". In: *Nanostructured Materials* 7.6 (1996), pp. 659–666.

[179] Nick S. Norberg and Daniel R. Gamelin. "Influence of surface modification on the luminescence of colloidal ZnO nanocrystals". In: *Journal of Physical Chemistry B* 109.44 (2005), pp. 20810–20816. ISSN: 15206106. DOI: `10.1021/jp0535285`.

[180] Viorica E. Podasca, Tinca Buruiana, and Emil C. Buruiana. "UV-cured polymeric films containing ZnO and silver nanoparticles with UV-vis light-assisted photocatalytic activity". In: *Applied Surface Science* 377 (2016), pp. 262–273. ISSN: 01694332. DOI: `10.1016/j.apsusc.2016.03.178`. URL: `http://dx.doi.org/10.1016/j.apsusc.2016.03.178`.

[181] P. A. Rodnyi, G. B. Stryganyuk, and I. V. Khodyuk. "Luminescence of a ZnO:Ga crystal upon excitation in vacuum UV region". In: *Optics and Spectroscopy* 104.2 (2008), pp. 210–212. ISSN: 0030-400X. DOI: `10.1134/s0030400x08020100`.

[182] Fiorenza Fanelli, Anna M. Mastrangelo, and Francesco Fracassi. "Aerosol-assisted atmospheric cold plasma deposition and characterization of superhydrophobic organic-inorganic nanocomposite thin films". In: *Langmuir* 30.3 (2014), pp. 857–865. ISSN: 15205827. DOI: `10.1021/la404755n`.

[183] Fiorenza Fanelli et al. "Preparation of multifunctional superhydrophobic nanocomposite coatings by aerosol-assisted atmospheric cold plasma deposition". In: *Nanoscience and Nanotechnology Letters* 7.1 (2015), pp. 84–88. ISSN: 19414919. DOI: `10.1166/nnl.2015.1943`.

[184] Fiorenza Fanelli et al. "Thin film deposition at atmospheric pressure using dielectric barrier discharges: Advances on three-dimensional porous substrates and functional coatings". In: *Japanese Journal of Applied Physics* 55.7S2 (2016). ISSN: 13474065. DOI: `10.7567/JJAP.55.07LA01`.

[185] Anna Liguori et al. "Co-Deposition of Plasma-Polymerized Polyacrylic Acid and Silver Nanoparticles for the Production of Nanocomposite Coatings Using a Non-Equilibrium Atmospheric Pressure Plasma Jet". In: *Plasma Processes and Polymers* 13.6 (2016), pp. 623–632. ISSN: 16128869. DOI: `10.1002/ppap.201500143`.

[186] Andrei Choukourov et al. "Plasma Polymerization on Mesoporous Surfaces: N-Hexane on Titanium Nanoparticles". In: *Journal of Physical Chemistry C* 119.52 (2015), pp. 28906–28916. ISSN: 19327455. DOI: `10.1021/acs.jpcc.5b08604`.

[187] Kyu Hyun Hwang et al. "Plasma-polymerized n-hexane and its utilization as multilayer moisture-barrier film with aluminum oxide". In: *Korean Journal of Chemical Engineering* 31.3 (2014), pp. 528–531. ISSN: 02561115. DOI: `10.1007/s11814-013-0278-2`.

[188] H. Biederman et al. "Deposition and properties of hydrophilic films prepared by plasma polymerization of Ar/n-hexane/H2O". In: *Vacuum* 46.12 (1995), pp. 1413–1418. ISSN: 0042207X. DOI: `10.1016/0042-207X(95)00163-8`.

[189] F. Sohbatzadeh et al. "Characterization and performance of coupled atmospheric pressure argon plasma jet with n-hexane electrospray for hydrophobic layer coatings on cotton textile". In: *Diamond and Related Materials* 91.August 2018 (2019), pp. 34–45. ISSN: 09259635. DOI: `10.1016/j.diamond.2018.10.023`. URL: `https://doi.org/10.1016/j.diamond.2018.10.023`.

[190] Dominic B. Potter, Ivan P. Parkin, and Claire J. Carmalt. "The effect of solvent on Al-doped ZnO thin films deposited via aerosol assisted CVD". In: *RSC Advances* 8.58 (2018), pp. 33164–33173. ISSN: 20462069. DOI: `10.1039/C8RA06417B`.

[191] Jörg Friedrich. "Mechanisms of plasma polymerization - Reviewed from a chemical point of view". In: *Plasma Processes and Polymers* 8.9 (2011), pp. 783–802. ISSN: 16128850. DOI: `10.1002/ppap.201100038`.

[192] Lin Guo et al. "Highly monodisperse polymer-capped ZnO nanoparticles: Preparation and optical properties". In: *Applied Physics Letters* 76.20 (2000), pp. 2901–2903. ISSN: 00036951. DOI: `10.1063/1.126511`.

[193] S. L. Chen, W. M. Chen, and I. A. Buyanova. "Dynamics of donor bound excitons in ZnO". In: *Applied Physics Letters* 102.12 (2013). ISSN: 00036951. DOI: `10.1063/1.4798531`.

[194] Catia Clementi et al. "Photoluminescence properties of zinc oxide in paints: A study of the effect of self-absorption and passivation". In: *Applied Spectroscopy* 66.10 (2012), pp. 1233–1241. ISSN: 00037028. DOI: `10.1366/12-06643`.

[195] Rachael Jetson et al. "Effects of surface modification on the fluorescence properties of conjugated polymer/ZnO nanocomposites". In: *Materials Chemistry and Physics* 124.1 (2010), pp. 417–421. ISSN: 02540584. DOI: `10.1016/j.matchemphys.2010.06.058`. URL: `http://dx.doi.org/10.1016/j.matchemphys.2010.06.058`.

[196] Alexey Kondyurin et al. "Covalent attachment and bioactivity horseradish peroxidase on plasma-polymerized hexane coatings". In: *Plasma Processes and Polymers* 5.8 (2008), pp. 727–736. ISSN: 16128850. DOI: `10.1002/ppap.200800010`.

[197] Aleksandra B. Djurišić and Yu Hang Leung. "Optical properties of ZnO nanostructures". In: *Small* 2.8-9 (2006), pp. 944–961. ISSN: 16136810. DOI: `10.1002/smll.200600134`.

[198] H. Zhou et al. "Behind the weak excitonic emission of ZnO quantum dots: ZnO/Zn(OH) 2 core-shell structure". In: *Applied Physics Letters* 80.2 (2002), pp. 210–212. ISSN: 00036951. DOI: `10.1063/1.1432763`.

[199] S. Monticone, R. Tufeu, and A. V. Kanaev. "Complex Nature of the UV and Visible Fluorescence of Colloidal ZnO Nanoparticles". In: *The Journal of Physical Chemistry B* 102.16 (1998), pp. 2854–2862. ISSN: 1520-6106. DOI: `10.1021/jp973425p`. URL: `http://pubs.acs.org/doi/abs/10.1021/jp973425p`.

[200] S. F. Chichibu et al. "Improvements in quantum efficiency of excitonic emissions in ZnO epilayers by the elimination of point defects". In: *Journal of Applied Physics* 99.9 (2006). ISSN: 00218979. DOI: `10.1063/1.2193162`.

[201] Pietro Camarda et al. "Luminescence mechanisms of defective ZnO nanoparticles". In: *Physical Chemistry Chemical Physics* 18.24 (2016), pp. 16237–16244. ISSN: 14639076. DOI: `10.1039/c6cp01513a`.

[202] John Wilkinson, K. B. Ucer, and R. T. Williams. "Picosecond excitonic luminescence in ZnO and other wide-gap semiconductors". In: *Radiation Measurements* 38.4-6 (2004), pp. 501–505. ISSN: 13504487. DOI: `10.1016/j.radmeas.2004.01.022`.

[203] Tobias Voss and Lars Wischmeier. "Recombination dynamics of surface-related excitonic states in single ZnO nanowires". In: *Journal of Nanoscience and Nanotechnology* 8.1 (2008), pp. 228–232. ISSN: 15334880. DOI: `10.1166/jnn.2008.N06`.

[204] Alessio Becheri et al. "Synthesis and characterization of zinc oxide nanoparticles: Application to textiles as UV-absorbers". In: *Journal of Nanoparticle Research* 10.4 (2008), pp. 679–689. ISSN: 13880764. DOI: `10.1007/s11051-007-9318-3`.

[205] Kyle W. Johnson et al. "Atmospheric pressure plasma enhanced chemical vapor deposition of zinc oxide and aluminum zinc oxide". In: *Thin Solid Films* 548 (2013), pp. 210–219. ISSN: 00406090.

DOI: `10.1016/j.tsf.2013.09.060`. URL: `http://dx.doi.org/10.1016/j.tsf.2013.09.060`.

[206] Andrea Illiberi et al. "Recent advances in atmospheric vapor-phase deposition of transparent and conductive zinc oxide". In: *Chemical Vapor Deposition* 20.7-9 (2014), pp. 234–242. ISSN: 15213862. DOI: `10.1002/cvde.201400056`.

[207] M. C. Ortega-Liebana et al. "Uniform luminescent carbon nanodots prepared by rapid pyrolysis of organic precursors confined within nanoporous templating structures". In: *Carbon* 117 (2017), pp. 437–446. ISSN: 00086223. DOI: `10.1016/j.carbon.2017.03.017`. URL: `http://dx.doi.org/10.1016/j.carbon.2017.03.017`.

[208] R. Armitage, Q. Yang, and E. R. Weber. "Analysis of the carbon-related "blue" luminescence in GaN". In: *Journal of Applied Physics* 97.7 (2005). ISSN: 00218979. DOI: `10.1063/1.1856224`.

[209] A. El Manouni et al. "Effect of aluminium doping on zinc oxide thin films grown by spray pyrolysis". In: *Superlattices and Microstructures* 39.1-4 (2006), pp. 185–192. ISSN: 07496036. DOI: `10.1016/j.spmi.2005.08.041`.

[210] A Piqué et al. "Effect of aluminum doping on zinc oxide thin films grown by pulsed laser deposition for organic light-emitting devices". In: *Thin Solid Films* 377-378 (2002), pp. 798–802. ISSN: 00406090. DOI: `10.1016/s0040-6090(00)01290-6`.

[211] A. F. Aktaruzzaman, G. L. Sharma, and L. K. Malhotra. "Electrical, optical and annealing characteristics of ZnO:Al films prepared by spray pyrolysis". In: *Thin Solid Films* 198.1-2 (1991), pp. 67–74. ISSN: 00406090. DOI: `10.1016/0040-6090(91)90325-R`.

Scientific Production

Published papers

E. Zanazzi, M. Favaro, A. Ficorella, L. Pancheri, G. F. Dalla Betta, A. Quaranta, “Radiation-induced optical change of ion-irradiated CdSeS/ZnS core-shell quantum dots embedded in polyvinyl alcohol”, Nuclear Inst. And Methods in Physics Research B, 435 (2018) 327–330.

E. Zanazzi, M. Favaro, A. Ficorella, L. Pancheri, G. F. Dalla Betta, A. Quaranta, “Proton Irradiation Effects on Colloidal InGaP/ZnS Core-Shell Quantum Dots Embedded in Polydimethylsiloxane: Discriminating Core from Shell Radiation-Induced Defects through Time-Resolved Photoluminescence Analysis”, J. Phys. Chem. C, 122 (2018) 22170-22177.

E. Zanazzi, M. Favaro, A. Ficorella, L. Pancheri, G. F. Dalla Betta, A. Quaranta, “Photoluminescence enhancement of colloidal CdSe/ZnS quantum dots embedded in polyvinyl alcohol after 2 MeV proton irradiation: crucial role of the embedding medium”, Optical Materials, 88 (2019) 271–276.

E. Zanazzi, M. Favaro, A. Ficorella, L. Pancheri, G. F. Dalla Betta, A. Quaranta, “Real-Time Optical Response of Polysiloxane/Quantum Dot Nanocomposite under 2 MeV Proton Irradiation: Luminescence Enhancement of the Polysiloxane Emission through Quantum Dot Sensitization”, Phys. Status Solidi A, 217 (2020), 1900586

M. Favaro, E. Zanazzi, A. Patelli, S. Carturan, R. Ceccato, V. Mulloni, M. Bortolotti, A. Quaranta, “Aluminum doped zinc oxide coatings at low temperature by atmospheric pressure plasma jet”, Thin Solid Films, 708 (2020), 138118

M. Favaro, A. Patelli, R. Ceccato, S. Diré, E. Callone, G. Fredi, A. Quaranta, "Co-deposition of plasma-polymerized n-hexane and zinc oxide nanoparticles with atmospheric pressure plasma jet", Coatings, submitted

M. Favaro, R. Ceccato, S. Diré, E. Callone, A. Quaranta, "Zinc oxide-based phosphors: the reduction effect on scintillation light yield", Journal of Applied Physics, to be submitted

Participation to *Congresses, Schools and Workshops*

Presentations at conferences, schools and workshops

Poster presentation at the workshop “Photonics as a key enabling technology” 17th November 2017, Bruno Kessler Foundation (FBK), Trento, Italy, “Synthesis and characterization of ZnO and ZnS deposited by atmospheric pressure plasma jet (APPJ) for scintillation detectors”.

Poster presentation at the Summer School on Neutron Detectors (NDRA 2018), 2nd - 5th July, 2018, Riva del Garda (TN), Italy, “Synthesis and characterization of ZnO and ZnS deposited by atmospheric pressure plasma jet (APPJ) for scintillation detectors”.

Acknowledgements

First and foremost I would like to thank Prof. Alberto Quaranta for trusting me, giving the possibility to pursue the doctoral course and for his valuable advice and support. A special thank is dedicated to my family, especially to my brother Luca, whom without this would have not been possible.
I would also like to express my sincere gratitude to Dr. Sara Carturan, Dr. Sandra Moretto and to all the people of the Legnaro National Laboratories for helping me with their technical and scientific support.
I would like to extend my sincere thanks to my former colleagues Dr. Enrico Zanazzi, Dr. Roberto Mendicino, Dr. Giulia Fredi and to all the professors, researchers, PhD students and technicians of the Department of Industrial Engineering for their constant help.
Lastly, a special thank goes to my friends Luca, Marco, Emanuele, Francesco, Lorenzo, Paola and Irene for their encouragement and constant support during these troubled years.

Matteo Favaro
Matteo Favaro